The Role of FBXW7 in CNS Myelination

Hannah Y. Collins

A DISSERTATION

Presented to the Neuroscience Graduate Program at the Oregon Health & Science University, Portland School of Medicine in partial fulfillment of the requirements for the degree of

DOCTOR OF PHILOSOPHY

Table of Contents

I. LIST OF FIGURES & TABLES

II. List of Abbreviations

Abbreviation	Full Term
CASPR	Contactin-associated protein
CHX	Cycloheximide
ChIP	Chromatin-immunoprecipitation
CNP1	Cyclic nucleotide 3' phosphodiesterase
CNS	Central nervous system
co-IP	Co-immunoprecipitation
CSF	Cerebral spinal fluid
dpf	Days post-fertilization
E	Embryonic day
EdU	5-ethynyl-2'-deoxyuridine
EGFP	Enhanced green fluorescent protein
ENU	N-ethyl-N-nitrosourea
ER	Endoplasmic reticulum
FBXW7	F-box and WD repeat domain-containing protein 7
FDR	False discovery rate
GFAP	Glial fibrillary acidic protein
GM	Grey matter
ICA	Intramolecular chaperone auto-processing domain
icKO	Inducible knockout mouse
IF	Immunofluorescence
KO	Constitutive knockout mouse
LC-MS	Liquid Chromatography-Mass Spectrometry
MAG	Myelin-associated glycoprotein
MAP1B	Microtubule-associated protein 1b
MBP	Myelin Basic Protein
MYO1D	Myosin ID
MYRF	Myelin Regulatory Factor
NICD	Notch intracellular domain
NPC	Neural progenitor cells
NSC	Neural stem cell
OLs	Oligodendrocytes
OPC	Oligodendrocyte precursor cells
PNS	Peripheral nervous system
pSS	Primary somatosensory cortex
RAE1	Ribonucleic acid export 1
SCF	SKP1-Cullin-Fbox

SCP	Schwann cell precursors
TAM	Tamoxifen
TEM	Transmission electron microscopy
TF/TFs	Transcription factor/Transcription factors
TMT	Tandem mass tags
WM	White matter

III. ACKNOWLEDGMENTS

As I reflect on the path that led me here, I am overwhelmed with gratitude for the people who have shaped my life and made this work possible.

To Holly and the entire Adams family — you opened your home and your hearts to me when I was sixteen, at a time when I had lost my way and my family. After the loss of my father, you welcomed me into your lives without hesitation, giving me not just shelter, but a true home. On your fourteen acres of beautiful land, I found a place where I could begin to heal my soul.

Holly, you have been my longest and most enduring friend—a constant through every season of my life. Your generosity has known no bounds, whether through time, love, or even money, and you have shown up for me in ways both big and small, again and again. From spontaneous road trips to unforgettable festivals, our adventures have stitched themselves into the fabric of my life. In you, I've had not only a best friend, but a sister—someone who's shared in my joy, held me in sorrow, and never once let go.

Becky, you were the mother I never knew I needed—nurturing, wise, and endlessly generous. You taught me that love can arrive in the most unexpected ways. Keith, you stepped into a fathering role with strength and kindness, always careful to honor and never overshadow my father's memory.

And to the whole Adams family, thank you for allowing me the space to rebel, to stumble through my grief, and to be an ignorant, wild child without ever withdrawing your love or support. Your patience, forgiveness, and unwavering belief in me gave me the room to grow into the person I was meant to be. Without you, this journey would not have been possible.

To my father, Dean Collins — you were not only a world-renowned photographer, but a fierce and devoted father who never stopped fighting for me. When I was a child caught in the storm of foster care, after my mother's betrayals and the painful unraveling of our family, you spent every penny you had to bring me back. You showed me what love, sacrifice, and resilience truly mean. Your passion for your art, your determination to create beauty in the world, and your refusal to give up on me shaped who I am more than words can fully express. Though cancer took you from me far too soon, your spirit remains with me in everything I do, in the curiosity that drives my science, in the persistence I bring to every challenge, and in the search for meaning and wonder in the world around me.

To Haley — you are my person, my sister, and my soulmate. Even though our relationship has always been fiery, you have been my constant: the one who understands me, challenges me, and holds me accountable. Watching you fight your way through your PhD, I learned some of the most important lessons about navigating academia — about resilience, integrity, and finding your own voice. Your hard-won wisdom shaped me more than you know. And yes, you can finally shut up, because I'm moving closer to you.

To the memory of Ben Barres — working in your lab at Stanford was one of the most formative experiences of my scientific life. Your brilliance as a scientist, your fierce advocacy for inclusion and fairness, and your generosity as a mentor shaped not only my research, but also the kind of scientist and human being I aspire to be. Your legacy lives on in every student and colleague you inspired, and I am proud to carry a small piece of that forward in my own work.

To my PhD mentors, Dr. Kelly Monk and Dr. Ben Emery — or as I affectionately call you, Ma and Pa, you have been nothing short of extraordinary. Kelly, with your razor-sharp eye and uncanny ability to spot every misplaced comma (and you know I had a lot), you taught me the precision and discipline that make great science and pushed me to be better at every turn, and I am endlessly grateful for your dedication. Ben, my Type B dad, always ready to dive into a discussion about science, you gave me a sense of calm that balanced me through the ups and downs of this journey. Additionally, I am eternally grateful that you made it to the end with me, and that you kept your promise to not kill yourself on that damn boat first, even though I know you gave it the old college try.

I also owe you both a giant apology for always being late on edits, please know it wasn't just procrastination (okay, sometimes it was), but mostly because every time I sent you something, I wanted to make it better and better… and better… until I completely overthought it and shot myself in the foot. Thank you for your patience with my "draft 27 of draft 5" tendencies and for pretending not to notice when deadlines mysteriously came and went.

Together, you created the perfect mentoring balance, and beyond that, you built and nurtured one of the most collaborative, generous, and inspiring scientific environments I have ever had the privilege to be a part of. The incredible research communities you've fostered, and the way you care for your students and postdocs, are seen and deeply appreciated by all of us. You have both shaped not just my career, but the scientist and colleague I aspire to be.

Finally, to the many mentors, colleagues, and friends along the way — thank you for your guidance, encouragement, and collaboration. This journey was never mine alone, and I am grateful beyond words for all of you who walked beside me.

This work is dedicated to Keith and Rebecca Adams, who have never treated me as anything less than their true daughter

IV. ABSTRACT

Myelination in the central nervous system (CNS) is a tightly orchestrated process that enables rapid impulse conduction, supports neuronal metabolism, and ensures long-term brain health. Oligodendrocytes (OLs), the myelinating glia of the CNS, achieve this by extending and wrapping their membranes around axons to form multi-lamellar myelin sheaths. While extrinsic cues such as axon diameter and neuronal activity influence OL behavior, intrinsic mechanisms that coordinate lineage progression, myelin synthesis, and sheath organization are less well understood. Here, we identify FBXW7, a substrate recognition subunit of the SCF (SKP1–CUL1–F-box) E3 ubiquitin ligase complex, as a pivotal regulator of OL development and myelin homeostasis. Using a combination of zebrafish models, primary OL cultures, and temporally controlled conditional knockout mice, we show that FBXW7 modulates OL lineage progression in a stage-specific and context-dependent manner.

Prior work suggested that in neural progenitors, FBXW7 limits oligodendrocyte precursor cell (OPC) production by repressing NOTCH1 signaling, thereby regulating the transition from progenitors to glial cells. Here we show that in mature OLs, FBXW7 prevents pathological myelin overgrowth and maintains sheath architecture by targeting the N-terminal cleavage product of MYRF (N-MYRF), a master transcriptional regulator of myelin gene expression, for proteasomal degradation. Loss of FBXW7 leads to the accumulation of N-MYRF, triggering excessive myelin production, transient sheath elongation, and subsequent development of myelin outfoldings and ectopic neuronal cell body wrapping.

Notably, *Myrf* haploinsufficiency partially rescues these phenotypes, underscoring MYRF as a critical downstream effector of FBXW7.

Importantly, we show that the consequences of *Fbxw7* loss are highly dependent on developmental timing: early deletion leads to OL loss and gliosis, whereas deletion in mature OLs induces sheath elongation and structural mis-patterning without overt cell death. Unbiased proteomic analyses further identify additional FBXW7-interacting proteins, including MAP1B, MYCBP2, and RAE1, suggesting broader regulatory functions in cytoskeletal organization, trafficking, and protein turnover.

Together, these findings position FBXW7 as a molecular brake that integrates developmental, transcriptional, and proteostatic mechanisms to fine-tune CNS myelination. By controlling both the quantity and quality of myelin produced, FBXW7 safeguards neural circuit architecture and function. This work has important implications for understanding myelin plasticity, neurodevelopmental disorders, and remyelination failure in disease, and opens new avenues for targeting FBXW7-dependent pathways with the goal of eventual therapeutic strategies.

V. CHAPTER 1: INTRODUCTION TO OLIGODENDROCYTES AND CENTRAL NERVOUS SYSTEM MYELINATION

Glial cells in the central nervous system

The central nervous system (CNS) comprises a highly organized and complex cellular network that underlies cognition, sensory integration, motor coordination, and physiological homeostasis. Although neurons have historically been the primary focus of neuroscience due to their role in electrical signal transmission, they account for only about half of the brain's cellular composition. The other half is made up of glial cells, non-neuronal populations with distinct morphologies and molecular identities[1]. Once thought to serve merely structural roles, glia are now recognized as active and indispensable players in CNS development, function, and plasticity. Insights from both zebrafish and mouse models have been instrumental in uncovering the diverse roles of glia, particularly in myelination[2,3] and neural circuit refinement[4,5]. The optical transparency and genetic tractability of zebrafish facilitate real-time *in vivo* imaging of glial dynamics[6], while murine models allow for precise temporal and lineage-specific manipulations to investigate glial contributions across developmental stages and in disease contexts[7,8]. Together, these model organisms have significantly advanced our understanding of glial biology within the CNS.

Glial cells can be broadly categorized into five major subtypes: ependymal cells, astrocytes, microglia, OPCs, and OLs. Each class exhibits specialized roles that extend far beyond structural support.

Ependymal Cells

Ependymal cells are classified as glia in large part due to their developmental origins from the neuroepithelial cells of the embryonic neural tube, the same progenitor pool that gives rise to neurons, astrocytes and OLs[9]. During early neurodevelopment, radial glial cells (RGCs) emerge from neuroepithelial precursors and serve as the principal progenitor population in the developing CNS[1,10]. While many RGCs differentiate into neurons or intermediate progenitors during embryogenesis, a subset transitions into glial lineages during the gliogenic switch[11]. Ependymal cells arise from these late radial glia that line the ventricles and exit the cell cycle postnatally to form a quiescent, multiciliated epithelial layer that form a barrier between the cerebral spinal fluid (CSF) and the underlying neural parenchyma[12,13]. The coordinated beating of the motile cilia of ependymal cells facilitates the circulation of CSF, thereby contributing to the distribution of signaling molecules and maintenance of intracranial pressure[11]. Ependymal cells also participate in CSF homeostasis through ion transport and barrier functions[14]. Recent studies suggest that subsets of ependymal cells may have latent neurogenic potential or contribute to injury-induced repair in specific contexts[11,15,16].

Astrocytes

Astrocytes are perhaps the most multifunctional glial subtype, exhibiting profound structural and functional heterogeneity across CNS regions[17–20]. Originating from radial glial progenitors[21–23], astrocytes populate the brain in a tiled, non-overlapping manner[24–26]. They are typically divided into two morphological classes:

protoplasmic astrocytes, found in gray matter, exhibit a highly branched, star-like morphology[24,27,28], while fibrous astrocytes, localized to white matter, possess longer and less branched processes[19,29].

Functionally, astrocytes perform critical roles in maintaining CNS homeostasis. These include regulation of extracellular potassium concentrations through Kir4.1 channels[30–32], neurotransmitter uptake and recycling, particularly glutamate via EAAT1/2 transporters, and providing metabolic substrates such as lactate to neurons through the astrocyte-neuron lactate shuttle[33–35]. Astrocytes are also essential for the development and maintenance of the blood–brain barrier (BBB)[36], interacting with endothelial cells and pericytes[36,37] via endfoot processes enriched in Aquaporin-4 and Connexins[38–40]. During synaptogenesis, astrocytes secrete factors such as thrombospondins and SPARCL1[41,42], which promote synaptic formation and maturation. In adulthood, astrocytes modulate synaptic function and contribute to long-term synaptic plasticity[43,44]. Furthermore, astrocytes act as innate immune responders, producing cytokines and chemokines in response to injury or infection[45,46], and undergo reactive gliosis in the context of neuroinflammation[47].

Although much of our understanding of astrocyte biology derives from mammalian systems, particularly rodents, recent work has demonstrated that astrocytes are a conserved glial cell type across vertebrates[1,9]. In zebrafish, both bona fide astrocytes and radial glia coexist within the central nervous system[48]. While radial glial cells are retained into adulthood and continue to serve as neural progenitors with astrocyte-like properties, such as neurotransmitter clearance, ion buffering,

and neurovascular modulation, recent studies have identified a distinct population of *Glast*$^{+}$ astrocytes that more closely resemble mammalian counterparts in both morphology and function[49]. These zebrafish astrocytes emerge from radial glial cells beginning at ~2 dpf, forming an elaborately branched meshwork of fine processes that tile the brain and spinal cord, associate closely with synapses, and express canonical astrocyte markers like glutamine synthetase. Time-lapse *in vivo* imaging has revealed dynamic process elaboration throughout development, as well as spontaneous calcium microdomain activity within astrocytic processes, paralleling the activity seen in mammalian astrocytes *in vivo*. Importantly, these astrocytes also exhibit responsiveness to neuromodulators such as norepinephrine and show tiling behavior indicative of spatial domain organization[48]. Collectively, these findings establish zebrafish as a powerful vertebrate model for studying astrocyte biology with high spatial and temporal resolution, including the first opportunity to image astrocyte morphogenesis continuously from birth to maturity *in vivo*[3,5].

Astrocyte-like cells have also been identified in Drosophila melanogaster, underscoring the ancient evolutionary origins of this glial cell type[22,50,51]. Despite the anatomical simplicity of the fly CNS, Drosophila astrocytes perform many core functions observed in vertebrate systems. They tile the neuropil in a non-overlapping manner, enwrap synapses, buffer extracellular ions, clear neurotransmitters, and regulate synaptic activity[22,50]. These cells express conserved molecular machinery, including glutamate transporters and potassium

channels, and have been leveraged as a genetically tractable system to dissect fundamental aspects of neuron-glia interactions across evolution[1,5].

Microglia

Microglia are the resident macrophage-like immune cells of the CNS. In mammals they arise from yolk sac-derived erythromyeloid precursors between embryonic day (E)7.5-E8.5, prior to the onset of definitive hematopoiesis[52,53]. These progenitors infiltrate the neuroepithelium via embryonic circulation and subsequently disperse throughout the parenchyma to form a non-overlapping, highly motile surveillance network that persists into adulthood[54,55].

Microglia continuously extend and retract their processes to monitor the CNS microenvironment and are pivotal for developmental synaptic refinement[4]. This process is mediated through phagocytosis of weak or excessive synapses, often via complement-dependent mechanisms involving proteins such as C1q and C3[56,57]. In addition to shaping synaptic architecture, microglia respond rapidly to CNS insults, adopting activated phenotypes characterized by morphological transformation[58], transcriptional reprogramming[59,60], and the secretion of pro-inflammatory or anti-inflammatory mediators[61]. They also clear apoptotic cells[62,63], protein aggregates[64,65], and cellular debris through phagocytic activity[66,67]. In zebrafish, microglia share many of these fundamental functions and originate from primitive macrophages in the rostral blood island, migrating into the CNS around 2-3 days post-fertilization (dpf)[68,69]. Thanks to the optical transparency and genetic tools available in zebrafish, researchers can directly visualize microglial behavior during development, injury response, and regeneration *in vivo*[6].

Oligodendrocyte Precursor Cells (OPCs)

OPCs, also known as NG2 glia due to their expression of the chondroitin sulfate proteoglycan NG2, are proliferative progenitor cells unique to vertebrates that can maintain as progenitors as well as give rise to myelinating OLs[70]. They are derived from specified domains of the ventral ventricular zone under the influence of transcription factors such as Olig1/2 and Nkx2.2[71,72]. Following specification, OPCs migrate extensively, proliferate, and tile the CNS[73]. Notably, OPCs are not restricted to development, they persist in the brain throughout life, retaining their proliferative capacity and contributing to myelin plasticity and repair in adulthood[72,74,75].

In addition to their canonical roles in generating OLs during development and remyelination[76], OPCs are increasingly recognized as an independent glial population with unique functional attributes. OPCs are the only glial cells known to receive direct synaptic input from neurons via AMPA- and GABA-receptor–mediated transmission[77–79], suggesting a capacity for activity-dependent regulation[80–82]. They also express molecules involved in immune signaling and can respond to inflammatory stimuli[83]. Recent work has shown that OPCs are capable of limited phagocytosis, contributing to the pruning of synaptic material, although to a lesser extent than microglia[74,84]. These properties position OPCs as both sensors and effectors within neural circuits, bridging developmental and adaptive roles[85].

In zebrafish, OPCs share many core features with their mammalian counterparts, including their specification from ventral neural progenitors under the control of

conserved transcription factors like Olig2[86,87]. Zebrafish OPCs emerge early in development, populating the spinal cord and brain as early as 2–3 dpf, and exhibit highly stereotyped patterns of migration, proliferation, and tiling, similar to those seen in mammals[86–89]. Moreover, studies in zebrafish have highlighted conserved OPC-neuron interactions and their response to neuronal activity, further validating the zebrafish as a powerful model to study OPC biology and plasticity across development, health, and repair[77,88].

Oligodendrocytes (OLs)

OLs are the myelinating cells of the CNS, responsible for wrapping axons in concentric layers of specialized membrane to form the myelin sheath[75]. OLs arise from OPCs following a tightly regulated sequence of transcriptional events, including the downregulation of proliferative signals[90] and upregulation of myelin-specific genes such as *Myelin basic protein* (*Mbp)*, *Proteolipid protein 1 (Plp1)*, *Myelin-associated glycoprotein (Mag)*, and *Myelin oligodendrocyte glycoprotein* (*Mog)*[91,92], discussed in more detail below. Myelin formation is a metabolically intensive process that requires massive membrane synthesis[93] and remodeling that involves dynamic cytoskeletal regulation to extend and wrap processes around axons[94–96].

The myelin sheath serves multiple functions: it electrically insulates axons to enable saltatory conduction, increases action potential propagation speed[97,98], and provides trophic support to maintain axonal health[99–102] by providing metabolic substrates such as lactate and pyruvate[103–105]. Importantly, myelinating OLs exhibit regional heterogeneity and adapt to local circuit demands[106], with what emerging

evidence suggesting myelin plasticity in response to experience or learning[80,107–111]. Dysfunction in OL development or myelin maintenance underlies a spectrum of demyelinating and neurodegenerative disorders[103], including leukodystrophies[112], multiple sclerosis[76], and certain psychiatric conditions[113–117].

Despite significant advances in our understanding of glial biology, the molecular and cellular mechanisms governing glial specification, maturation, and function remain incompletely characterized. The studies described in this dissertation aim to investigate the cell-intrinsic regulatory networks and transcriptional programs that control OL lineage progression and myelin biogenesis. Elucidating these mechanisms is critical not only for understanding CNS development but also for informing therapeutic strategies to promote remyelination and neuroprotection in disease contexts.

Development of OL lineage cells

OPCs are specified in three temporally and spatially distinct waves during embryonic development, originating from NPCs[72]. In the mouse, the first wave emerges at embryonic day E12.5 from the ventral medial ganglionic eminence and the anterior entopeduncular area[72,118]. The second wave arises at E15.5 from the lateral and caudal ganglionic eminences[118–121], while the third and final wave originates from cortical NPCs around birth and populates the upper cortical regions[122]. These temporally and regionally defined origins confer distinct properties on OPCs, including differences in proliferative capacity, differentiation potential, and regional distribution[77,123]. Lineage-tracing studies in rodents have revealed that OPCs derived from early waves are often eliminated during CNS

maturation, with the third wave contributing substantially to the postnatal and adult OPC pool[124].

The site of OPC specification significantly influences their subsequent behavior[125]. In rodent white matter (WM), OPCs exhibit higher rates of proliferation and a greater propensity to terminally differentiate into mature OLs, which no longer divide[126,127]. In contrast, gray matter (GM)-derived OPCs in the ventral forebrain and spinal cord can give rise to both OLs and, under some conditions, protoplasmic astrocytes, highlighting their lineage plasticity[128]. Notably, approximately 40% of OPCs that initiate differentiation into OLs undergo programmed cell death, both during development and in adulthood, underscoring the tight regulation of OL number and the competitive nature of myelination[129,130].

Myelination begins when differentiated OLs extend elaborate processes that contact axons and initiate membrane wrapping[131]. The leading edge of the OL's process spirals concentrically around the axon, excluding cytoplasm and forming the compacted, multilamellar structure characteristic of the myelin sheath[2,94,96]. In rodents, this initial wrapping phase is followed by a period of sheath elongation and stabilization, which predominantly occurs in the first few weeks postnatally and continues into early adulthood, particularly in regions such as the corpus callosum, optic nerve, and spinal cord[109,132,133]. In zebrafish, by contrast, myelination is remarkably rapid and stereotyped: initial sheath formation begins within a day after OPC differentiation, with sheath elongation occurring over hours to days, and stabilization typically achieved within 24–48 hours[77,134,135]. Notably, zebrafish OLs extend a surplus of nascent sheaths, pruning back a subset during the stabilization

phase, a process that mirrors the refinement seen in mammalian systems but on an accelerated developmental timescale[136].

Intriguingly, while rodent OLs myelinate only axons under physiological conditions[75,80,81,137–139], zebrafish OLs display transient ensheathment of neuronal cell bodies even in wild-type animals, highlighting a species-specific feature that has provided valuable insight into the mechanisms of target selection and sheath pruning[3,136]. Additionally, rodent OLs will myelinate inert synthetic fibers or beads *in vitro*[140], demonstrating that the core capacity to initiate myelination is an intrinsic property of the cell, although *in vivo* this process is tightly regulated by molecular cues that orchestrate axon selection, sheath patterning, and adaptation to environmental demands[80,81,99,101,102,131,134].

While OPC specification and expansion predominantly occur prenatally in rodents[72], the onset of myelination coincides with birth and extends into adulthood, with a gradual decline in later life[75,109]. OPC differentiation and myelin formation are governed by cell-intrinsic transcriptional and epigenetic programs[92,130,141], but OPCs are also highly responsive to extrinsic factors, including neuronal activity[77,80–82], axon-glia signaling[81,102,103], and interactions with other glial cells[66,142]. Importantly, both rodents and zebrafish display activity-dependent myelin plasticity, wherein OLs modulate sheath number, length, and thickness in response to changes in neuronal firing[77,80–82]. In zebrafish, sensory experience has been shown to regulate the formation and stabilization of individual sheaths[77], while in rodents, activity-dependent remodeling of pre-existing myelin, including sheath length adjustments and de novo sheath formation, persists into

adulthood[108,143,144]. This dynamic plasticity provides an experience-dependent layer of control over axonal conduction velocity, synaptic integration, and neural circuit function.

Mature OLs and the myelin they produce are remarkably stable and long-lived[109,133]. Carbon-14 birth-dating studies in humans have demonstrated that WM OLs can persist for decades, while lineage-tracing and fate-mapping experiments in mice estimate OLs survive for several years[75,145]. Estimates of adult oligodendrogenesis in humans suggest ongoing but regionally variable turnover, with greater replacement in gray matter compared to the relatively stable white matter[127,146]. Notably, adult OPCs in rodents continue to proliferate and can generate new OLs in response to environmental cues or injury[73,110,122], suggesting a lifelong capacity for remodeling, although the functional integration of these new cells is still under active investigation.

The importance of long-term myelin maintenance is underscored by the devastating consequences of demyelinating diseases such as multiple sclerosis and leukodystrophies[76,112,147]. Although these conditions are often driven by autoimmune mechanisms targeting CNS myelin[148], the downstream loss of myelin, OL degeneration, and subsequent axonal pathology are central to disease progression and neurological dysfunction[76,83,137]. While remyelination has traditionally been attributed to newly differentiated OLs derived from OPCs, recent studies suggest that mature OLs can also contribute directly to remyelination, though how effective this remyelination to functional recovery is still debated[149]. Given the longevity of OLs and the extensive membrane infrastructure they

sustain, elucidating the molecular mechanisms underlying OLs homeostasis, myelin plasticity, and CNS maintenance over the lifespan remains a critical challenge for the field[75,109]. Insights from comparative models such as mouse and zebrafish, with their rapid and accessible myelination dynamics, are poised to shed light on conserved and divergent mechanisms of myelin regulation across vertebrates

Molecular mechanisms of OL myelination

The transition from OPCs to mature, myelinating OLs is orchestrated by a sophisticated regulatory network that integrates transcriptional programs[92,150,151], intracellular signaling pathways[152–155], and cytoskeletal remodeling[95,96,156]. This shift requires the coordinated repression of OPC-associated genes and the activation of a myelination-specific transcriptional program, accompanied by dynamic actin and microtubule remodeling[95,96,156], membrane biogenesis[93,132,157], increased lipid synthesis[158,159], and the induction of structural myelin proteins[160].

Transcriptional regulation of OL differentiation

Among the earliest transcription factors (TFs) in the OL lineage is OLIG2, which promotes OPC specification and proliferation[71,92]. SOX10, another lineage-defining TF, is expressed throughout the OL lineage and plays stage-specific roles: in OPCs, SOX10 cooperates with OLIG2 to maintain progenitor identity and support proliferation[92,150,161], but as differentiation begins, SOX10 redirects its activity toward promoting myelin gene expression. This switch is critically dependent on the induction of *Myrf* (*Myelin regulatory factor*), which acts as a molecular linchpin, guiding SOX10 to activate myelin-specific targets[161,162], a

mechanism recently highlighted by studies showing that MYRF modulates SOX10 target selection during OL development[150].

MYRF is indispensable for both the initiation and maintenance of CNS myelination[151,163]. It is synthesized as a type-II membrane protein in the endoplasmic reticulum (ER), where its intramolecular chaperone auto-processing (ICA) domain promotes trimerization and autocatalytic cleavage[164]. The resulting N-terminal trimer translocates to the nucleus, where it functions as a transcriptional activator, driving expression of canonical myelin genes such as *Mbp*, *Plp1*, *Mag*, and *Mog*[164–166]. Although initially characterized in the CNS, MYRF is also expressed in peripheral tissues including the retina, lung, heart, and urogenital tract, and *MYRF* mutations in humans are associated with multisystem congenital anomalies[167–169]. In mice, homozygous *Myrf* deletion results in embryonic lethality, underscoring its essential roles beyond the CNS[163].

Within the CNS, *Myrf* expression is restricted to differentiating OPCs, newly formed OLs, and myelinating OLs[20,151]. It is considered a master regulator of myelin gene expression and is required for both the transition into the myelinating state and the long-term stability of mature OLs[161,163]. MYRF directly regulates canonical myelin genes such as *Mbp*, *Plp1*, *Mag*, and *Mog*. Loss-of-function studies show that *Myrf* deletion in OPCs does not compromise survival or proliferation, but it blocks terminal differentiation and leads to the loss of mature OL transcripts and myelin sheaths, rather than immediate cell death[151,163,170]. Similarly, inducible *Myrf* ablation in postmitotic OLs disrupts maintenance of the myelinating state and compromises OL function[108,170].

Genetic models using *Myrf*$^{fl/fl}$ animals crossed with inducible Cre drivers (e.g., *Pdgfra-Cre*^{ERT2}, *Plp1-Cre*^{ERT}, *Sox10-Cre*^{ERT2}) have become powerful tools in myelin research[171]. Conditional *Myrf* deletion in OPCs halts new myelin formation, enabling temporal interrogation of developmental and adult myelination[144,170]. These models have clarified the role of myelination in memory consolidation and critical period plasticity[172,173]. Deletion in mature OLs has been used to model demyelination and remyelination independent of immune mechanisms, allowing focused analysis of OL-intrinsic support of axonal integrity[104,170]. Dual-lineage deletion using *Sox10-Cre*^{ERT2} disrupts both OPCs and OLs, causing widespread demyelination and failure to remyelinate, which has helped reveal the neuronal consequences of chronic myelin loss[170].

Intracellular signaling pathways regulating myelination

Beyond TFs, several intracellular signaling pathways converge to regulate OL differentiation and myelination. NOTCH1 signaling is a key negative regulator[90,174,175]. In the developing CNS, activation of NOTCH1 by its canonical ligand JAGGED1, typically expressed in neurons and astrocytes[176,177], maintains OPCs in an undifferentiated state by inducing HES family repressors such as HES1 and HES5[178,179], which inhibit pro-myelination genes including *Myrf* and *Sox10*[162]. Conditional ablation of *Notch1* or its downstream effectors accelerates OL differentiation[175], while sustained NOTCH1 activation impairs myelination[90], highlighting its role in timing OPC differentiation and potentially regulating remyelination following injury[175].

The mechanistic target of rapamycin (mTOR) pathway promotes myelination by controlling metabolic programs necessary for membrane biogenesis[154,155,180]. mTOR operates through two distinct complexes, mTORC1[181] and mTORC2[182], with mTORC1 being especially important in OLs[155]. mTORC1 integrates growth factor and neuronal activity signals to regulate lipid synthesis, protein translation, and cytoskeletal remodeling essential for membrane extension and wrapping[183]. Conditional deletion of *Raptor*, a critical mTORC1 component, in OLs leads to severe hypomyelination and impaired expression of myelin genes, whereas hyperactivation of mTOR signaling enhances myelination by boosting membrane production and wrapping[154,184].

Additionally, the MAPK/ERK signaling pathway has emerged as a key regulator of OL wrapping and sheath elongation[94,153]. Active during both development and adulthood, the MAPK-ERK cascade promotes cytoskeletal remodeling and membrane expansion, a processes critical for successful axonal ensheathment[153]. This pathway is canonically activated downstream of receptor tyrosine kinases (RTKs), such as FGFRs and TrkB, which respond to extracellular growth factors and neurotrophins[185]. Ligand binding induces RTK dimerization and autophosphorylation, recruiting adaptor proteins like GRB2 and the RAS-activating guanine nucleotide exchange factor SOS[186]. Once activated, RAS initiates a phosphorylation cascade through RAF and MEK that culminates in ERK1/2 activation[187]. In OLs, this cascade facilitates actin disassembly, promotes lipid and protein trafficking to growing membranes, and integrates axonal signals to tune myelin growth[153,187]. Manipulation of MAPK/ERK activity can alter sheath length

and thickness, emphasizing its roles not only in early myelination but also in experience-dependent plasticity[153].

Cytoskeletal mechanisms of myelination

The cytoskeleton plays an essential and dynamic role in OL differentiation, myelin sheath formation, and maintenance[156]. As OPCs transition to OLs, extensive remodeling of the actin and microtubule networks is required to support the dramatic morphological changes that accompany axonal ensheathment and membrane wrapping[95,96]. Initially, actin polymerization drives the extension of OL processes toward target axons, establishing contact and initiating ensheathment. Once wrapping is underway, however, a marked shift occurs: actin depolymerization becomes critical to allow membrane spreading and compaction, facilitating the formation of the multilayered, cytoplasm-excluded myelin sheath[95,96]. Pharmacological disruption of actin turnover at this stage leads to stalled or incomplete wrapping, underscoring the necessity of tightly coordinated cytoskeletal dynamics[188].

Actin-binding proteins, including cofilin, gelsolin, and the Arp2/3 complex, regulate the balance between actin polymerization and depolymerization, and their precise spatiotemporal control is crucial for sheath expansion. Cofilin-mediated severing of actin filaments, for example, has been shown to be indispensable for sheath elongation, while Arp2/3-driven branching is required for the initial protrusive activity at the leading edge [189–191].

Microtubules also play key roles in OL morphology and myelination. Microtubule extension supports process outgrowth, and stabilization of the microtubule network

helps establish the intracellular transport highways necessary to deliver membrane components and myelin proteins to the growing sheath[192,193]. The microtubule-associated protein TAU and motor proteins such as kinesins and dyneins coordinate the trafficking of vesicles, organelles, and cytoskeletal regulators critical for membrane expansion and compaction[64,194,195].

Collectively, the cytoskeleton acts as both a structural framework and an active driver of myelination, orchestrating the complex choreography of process extension, wrapping, and sheath maturation[95,96,156,188–191]. A deeper understanding of these mechanisms holds promise for identifying novel targets to promote remyelination and restore OL function in demyelinating conditions.

Integration of transcriptional, signaling, and cytoskeletal networks

Taken together, while MYRF serves as a master regulator that reprograms the transcriptional landscape of differentiating OLs[150,151,163], its activity is embedded within a broader regulatory framework that integrates intrinsic TFs (e.g., SOX10, OLIG2)[71,150,161], cell-extrinsic cues (e.g., neuronal activity, axon-glia interactions)[80–82], intracellular signaling pathways (e.g., NOTCH1, mTOR, MAPK/ERK)[90,153,183], and cytoskeletal dynamics[96,156]. The actin and microtubule cytoskeletons do not merely provide structural support but actively drive OL morphological changes, process extension, axonal wrapping, and sheath stabilization, translating upstream signals into the physical work of myelination[192,193].

A deeper understanding of how these transcriptional, signaling, and cytoskeletal mechanisms are integrated to coordinate myelin formation, long-term

maintenance, and adaptive plasticity will be critical for the development of targeted therapies aimed at enhancing remyelination and preserving CNS function in demyelinating diseases. Importantly, insights from comparative models such as zebrafish, with their rapid and accessible myelination dynamics, will continue to illuminate both conserved and species-specific principles underlying OL biology and CNS repair.

Schwann cell myelination

In addition to the CNS, myelination also occurs in the peripheral nervous system (PNS), where it is mediated by Schwann cells (SCs). Remarkably, SCs evolved the capacity to generate myelin independently from the OL lineage of the CNS[2]. Although both cell types likely share a common ancestral glial cell, possibly resembling those found in primitive, non-myelinated vertebrates such as the lamprey[196], they employ largely distinct genetic programs and regulatory mechanisms to generate structurally similar multilamellar myelin sheaths[197].

It is hypothesized that the evolutionary pressure to maintain rapid axonal conduction in increasingly complex and larger organisms drove the independent emergence of myelination in both the CNS and PNS[198]. Despite converging on a similar functional outcome, OLs and SCs exhibit fundamental differences in developmental origin, cellular behavior, and regenerative capacity[196,198].

A key distinction is in their myelination strategy: mature OLs in the CNS can myelinate multiple axons simultaneously, often up to 50, by extending numerous processes[199]. In contrast, SC in the PNS exhibit a strict 1:1 relationship with axons; a single SC myelinates only one axonal segment[200,201]. Furthermore, while mature

OLs are terminally differentiated and cannot revert to a progenitor-like state, SCs retain remarkable plasticity[202]. Following peripheral nerve injury, SCs can de-differentiate into a “repair” phenotype[152,203], characterized by enhanced expression of growth factors, phagocytic activity to clear myelin debris, and support for axonal regrowth[203], a response not observed in CNS OLs.

SCs are derived from neural crest cells, a transient, multipotent embryonic cell population. During development, neural crest cells migrate along peripheral nerves and differentiate into Schwann cell precursors (SCPs), which then give rise to immature SCs[204,205]. As SCPs populate peripheral nerves, they begin a critical morphogenetic process known as radial sorting, in which SCs extend cytoplasmic processes to segregate axons based on caliber[206,207]. In mammals, large-diameter axons (>1 μm) are sorted for subsequent myelination, whereas small-diameter axons (<1 μm) remain unmyelinated and become ensheathed within Remak bundles by non-myelinating SCs, known as Remak SCs[206,208].

Following radial sorting, myelinating SCs undergo differentiation and initiate the wrapping of selected large-caliber axons with compact myelin. This process is driven by the activation of key transcription factors such as *Egr2* (*Krox20*)[209], *Oct6* (*Pou3f1*)[204], and *Sox10*, which regulate expression of essential myelin genes including *Mpz* (myelin protein zero), *Pmp22*, and *Mbp*[210].

Although the morphological stages of SC development, radial sorting, lineage bifurcation, and myelination are well characterized, the molecular signals regulating these transitions remain incompletely understood. Neuregulin-1 (NRG1) signaling via ERBB receptors on SCs is known to play a pivotal role in axon-SC

communication and radial sorting[209]. However, the full complement of transcriptional, epigenetic, and metabolic cues that govern SC fate decisions and plasticity, particularly during regeneration, is still an area of active investigation[202,203].

Forward genetic screen in zebrafish to identify novel regulators of myelination

Forward genetic screens in model organisms such as *Danio rerio* (zebrafish) have proven to be exceptionally powerful tools for uncovering the molecular mechanisms that regulate myelination[211]. Dr. Kelly Monk, upon establishing her laboratory at Washington University in St. Louis, collaborated with the Solnica-Krezel lab to perform a large-scale, three-generation forward genetic screen using N-ethyl-N-nitrosourea (ENU) mutagenesis[212]. Given the remaining knowledge gaps in myelin biology, the Monk and Solnica-Krezel labs initiated a new forward genetic screen to uncover novel genes required for glial development and myelination.

The screening strategy involved ENU mutagenesis of male zebrafish[213], which were subsequently outcrossed through three generations to wild-type fish that were double homozygous for two fluorescent reporter transgenes: Tg(lhx1a:eGFP)[214] and Tg(mbp:mCherry-CAAX)[215]. The *lhx1a* promoter drives expression of enhanced green fluorescent protein (EGFP) in a subset of sensory neurons, allowing visualization of axonal structures, while *mbp* drives membrane-targeted mCherry (mCherry-CAAX) expression in OLs and SCs. MBP is a critical

structural protein involved in the compaction of the myelin sheath and serves as a robust marker for mature myelinating glia[160].

The dual-reporter strategy enabled simultaneous visualization of both axons and myelin, facilitating the discrimination between primary defects in myelin formation and secondary phenotypes resulting from axonal loss. This approach also allowed the identification of both CNS and PNS myelination abnormalities in living zebrafish larvae.

Whole-genome sequencing and phenotypic screening of approximately 680 mutagenized genomes yielded 31 recessive mutations that disrupted glial development and/or myelination in either the PNS or CNS. After rigorous validation, 26 mutations were confirmed as true positives and shown to be heritable, while five lines were excluded due to inconsistent or non-reproducible phenotypes.

This screen represents one of the most comprehensive efforts to date to identify novel regulators of myelinating glia using a vertebrate genetic model. It expands the genetic toolkit available to study myelin biology and offers a foundation for dissecting the complex molecular networks that coordinate glial differentiation, axon-glial interactions, and myelin maintenance[212].

FBXW7's role in CNS development and myelination

While most mutations identified in the zebrafish forward genetic screen led to reduced or disrupted myelination, one exceptional allele, *stl64*, resulted in increased myelination, a highly unusual and biologically intriguing phenotype[212].

This mutation was mapped to the *fbxw7* gene, which encodes F-box and WD repeat domain-containing protein 7 (FBXW7), a substrate recognition component of the SCF (Skp1–Cullin–F-box) E3 ubiquitin ligase complex[216]. E3 ligases function as the specificity-conferring arm of the ubiquitin-proteasome system, recruiting defined sets of target proteins for polyubiquitination and subsequent proteasomal degradation[217]. Within the SCF complex, FBXW7 binds phosphorylated substrates and facilitates their ubiquitination by coordinating with the Skp1 adaptor, the Cul1 scaffold, and the Rbx1-RING finger protein that recruits E2 ubiquitin-conjugating enzymes[216,218,219]. In this way, FBXW7 serves as a central regulator of proteostasis, targeting a range of key transcription factors, signaling proteins, and cell cycle regulators for degradation to maintain cellular homeostostasis[220]. FBXW7 plays a critical role in maintaining developmental and cellular homeostasis by controlling the stability of a broad array of substrates, including NOTCH1, c-MYC, c-JUN, CYCLIN E, mTOR, and MCL-1[218,221–223]. Structurally, FBXW7 contains an F-box domain that recruits the SCF complex, a dimerization domain, and seven WD40 repeats that recognize conserved phosphodegron motifs on its substrates[224]. Best known as a tumor suppressor, FBXW7 is frequently mutated, deleted, or epigenetically silenced in diverse array of human cancers, including colorectal, endometrial, breast, gastric, and hepatocellular carcinomas. Loss of FBXW7 function leads to the accumulation of its oncogenic targets, driving unchecked proliferation, genomic instability, and resistance to apoptosis, all hallmarks of tumorigenesis[216]. Notably, mutations in the WD40 substrate-binding domain, particularly at conserved arginine residues

such as Arg465, Arg479, Arg505, impair substrate recognition and are strongly associated with poor prognosis and chemoresistance in cancer[219].

The role of FBXW7 in the PNS was further clarified by the Monk lab using *fbxw7*$^{stl64/stl64}$ zebrafish and *Dhh-Cre; Fbxw7*$^{fl/fl}$ mice, which revealed that SC-specific deletion of *Fbxw7* caused multiple defects: increased SC numbers, disrupted radial sorting, aberrant SC-axon ratios, and hypermyelination[225]. Surprisingly, *Fbxw7*-deficient SCs acquired a hybrid phenotype, capable of both myelinating large-caliber axons and ensheathing small unmyelinated fibers, resembling both myelinating SCs and non-myelinating Remak cells[225]. Because some of these phenotypes were reminiscent of PTEN loss-of-function[226] and AKT hyperactivation[227], both of which enhance mTOR signaling, the Monk lab tested whether elevated mTOR activity accounted for the defects observed in *Fbxw7*-deficient SCs. Indeed, genetic deletion of mTOR in the *Fbxw7*-null background (*Dhh-Cre; Fbxw7*$^{fl/fl}$*; mTOR*$^{fl/fl}$) rescued most of the developmental phenotypes, except the formation of hybrid SCs. This suggested that while mTOR is a critical effector downstream of FBXW7 in regulating SC proliferation, sorting, and myelin thickness, the cell fate plasticity seen in *Fbxw7*-deficient SCs involves an mTOR-independent pathway, likely regulated by other FBXW7 targets[225].

In the context of OL development, FBXW7 loss biases NSC-derived progenitors toward the OL lineage by prolonging NOTCH1 activity, which promotes the specification of NPCs to OPCs[221,223]. Additionally, FBXW7 negatively regulates mTOR signaling in the developing zebrafish, a central pathway controlling cell growth, protein synthesis, and metabolism[228]. In the OL lineage, mTOR promotes

myelin gene expression and lipid synthesis, both essential for myelin production[155]. Thus, FBXW7 is proposed to coordinate a dual regulatory role, first limiting OPC generation via NOTCH1 and later restraining excessive myelin synthesis via mTOR inhibition. However, while this dual role is supported by zebrafish studies[228] and by indirect evidence from mammalian systems, it is important to note that in the mammalian CNS, the only available conditional knockout study used a *Nestin-Cre,* which targeted *Fbxw7* broadly in both neural stem cells and glial progenitor cells[223]. Although this study reported increased OPC numbers, abnormal myelination, and elevated mTOR pathway activity, it remains unclear whether mTOR is a direct downstream target of FBXW7 in mature OLs specifically. As such, while mTOR dysregulation is a strong candidate mechanism, further work is needed to clarify the precise molecular pathways by which FBXW7 regulates myelination.

In summary, FBXW7 orchestrates neural development and myelination by regulating the stability of proteins that control stem cell fate, lineage specification, and myelin production[221,223,228]. Its modulation of NOTCH1 and mTOR establishes it as a critical protein integrating extrinsic cues and intrinsic timing mechanisms to ensure proper CNS and PNS myelination. Importantly, clarifying whether mTOR acts as a direct downstream target of FBXW7 in CNS OLs, as it does in SCs, remains a key area for future investigation. Further identification of FBXW7 substrates in glial cells promises to uncover novel regulators of CNS development and homeostasis.

Regulation of MYRF by FBXW7

While FBXW7 had been implicated in regulating mTOR[228] and Notch1[221] signaling in the developing zebrafish spinal cord, whether these pathways operate similarly in the mammalian CNS remained unresolved. This question gained additional significance with the discovery that FBXW7 also targets MYRF, the master transcription factor essential for CNS myelination, in liver cancer cells[229]. Around the time the Monk lab was completing its investigation of FBXW7 in SC development, a separate study identified MYRF as a direct substrate of FBXW7 in a mouse hepatocellular carcinoma (mHepa) cell line. This study demonstrated that FBXW7 physically interacts with MYRF and promotes its degradation via the ubiquitin-proteasome pathway[229]. This interaction was shown to be phosphorylation-dependent, requiring prior phosphorylation of MYRF by glycogen synthase kinase 3β (GSK3β), a kinase known to prime substrates for FBXW7 binding by modifying residues within the conserved Cdc4 phosphodegron (CPD) motif[230].

This discovery provided a compelling molecular link between FBXW7 and the regulation of myelin gene expression in the CNS, suggesting a novel mechanism through which FBXW7 could control OL differentiation and myelination by targeting MYRF for proteasomal degradation. Given MYRF's essential role in driving the transcriptional program of myelin-related genes such as *Mbp, Plp1, and Mog*[92], the identification of FBXW7 as a negative regulator of MYRF introduces a key post-translational checkpoint in the control of CNS myelination.

Taken together, the dual role of FBXW7 in suppressing oncogenic signaling in cancer[216] and in modulating lineage-specific transcriptional programs in the CNS[221,228], potentially through the regulation of MYRF, highlights its significance as a master regulator of cellular homeostasis[229]. These findings also underscore the importance of dissecting FBXW7's function in OLs using cell-type-specific genetic models to determine whether MYRF is a physiologically relevant substrate of FBXW7 *in vivo*, and to define how ubiquitin-mediated turnover of MYRF integrates into the broader regulatory network controlling myelination.

In summary, the coordinated process of myelination in both the central[151,151] and peripheral nervous systems[207] is governed by a complex interplay of transcriptional, post-transcriptional, and signaling mechanisms that remain only partially understood. Central to this process is the transcription factor MYRF[151,163], a master regulator of OL maturation and myelin gene expression, whose regulation is now known to involve the ubiquitin ligase FBXW7[229]. The dual role of FBXW7 in targeting both mTOR[228] and NOTCH1[221] signaling components, as well as potentially MYRF itself[229], places it at a critical intersection of pathways that control neural stem cell fate decisions, OL lineage specification, and terminal differentiation. Parallel insights from SC biology in the PNS highlight the evolutionarily conserved yet distinct strategies used to achieve myelination across vertebrates[225]. Importantly, forward genetic screens in zebrafish have proven instrumental in identifying novel regulators such as Fbxw7 and underscore the value of unbiased discovery in uncovering unexpected players in myelin biology[212]. Furthermore, the emerging evidence that FBXW7 acts as a key tumor suppressor

in multiple cancers reinforces the broader significance of protein homeostasis in controlling cell identity, proliferation, and function[216]. Together, these findings underscore the importance of dissecting both transcriptional and posttranslational mechanisms in glial development and provide a compelling rationale for continued exploration of FBXW7-MYRF signaling as a fundamental axis in CNS myelination and a potential target for therapeutic modulation in demyelinating diseases.

Significance and Goals of the Study

Proper myelination of the CNS is essential for rapid nerve conduction, metabolic support of axons, and long-term maintenance of neural circuits[102,231]. OLs, the glial cells responsible for producing CNS myelin, undergo a tightly regulated transition from highly proliferative OPCs to postmitotic, myelinating OLs[130]. This process is orchestrated by an intricate interplay of cell-intrinsic[140] transcriptional programs and cell-extrinsic signaling cues[232]. Disruptions in OL differentiation or myelin production can result in profound neurological deficits[101,110,231], as seen in diseases such as multiple sclerosis[148], leukodystrophies[112], and traumatic CNS injury[233]. While substantial progress has been made in identifying transcription factors critical for OL development and function, including the master regulator MYRF, the upstream molecular mechanisms that govern the timing and fidelity of OL differentiation and myelination remain incompletely understood.

FBXW7, a substrate adaptor of the SCF E3 ubiquitin ligase complex, plays a central role in regulating the stability of multiple key signaling proteins, including NOTCH1[221] and mTOR[228]. Previous work in zebrafish suggested that loss of *fbxw7* results in increased OPC number due to elevated Notch1 signaling[221],

with additional evidence implicating a potential role in restricting myelin synthesis through the regulation of mTOR[228]. However, whether these regulatory pathways are conserved in the mammalian CNS and whether FBXW7 functions in a cell-autonomous manner within OLs to control their differentiation, maturation, and homeostasis has not been fully established. Moreover, emerging evidence suggests that FBXW7 may directly regulate MYRF[229], providing a potential mechanistic link between upstream signaling control and the core transcriptional machinery required for CNS myelination.

The work presented in this thesis addresses these key gaps by defining the role of FBXW7 in OL lineage progression, myelination, and maintenance in the zebrafish and mammalian CNS. Through a combination of genetic, molecular, and imaging approaches, this study investigates how FBXW7 governs the transition from OPC to mature OL, how its loss alters myelin sheath formation, and how these effects intersect with known pathways such as mTOR signaling and MYRF regulation. By dissecting the FBXW7 regulatory network in OLs, this work provides novel insights into the molecular logic of CNS myelination, offering a framework for understanding how dysregulation of proteostasis can compromise glial function and neural circuit integrity.

More broadly, the findings have significant implications for identifying potential therapeutic targets to promote remyelination in demyelinating diseases and for uncovering general principles of glial cell regulation across development and disease. By addressing both the fundamental biology and the translational relevance of FBXW7 function in the CNS, this study advances our understanding

of the mechanisms that maintain myelin homeostasis and safeguard nervous system health.

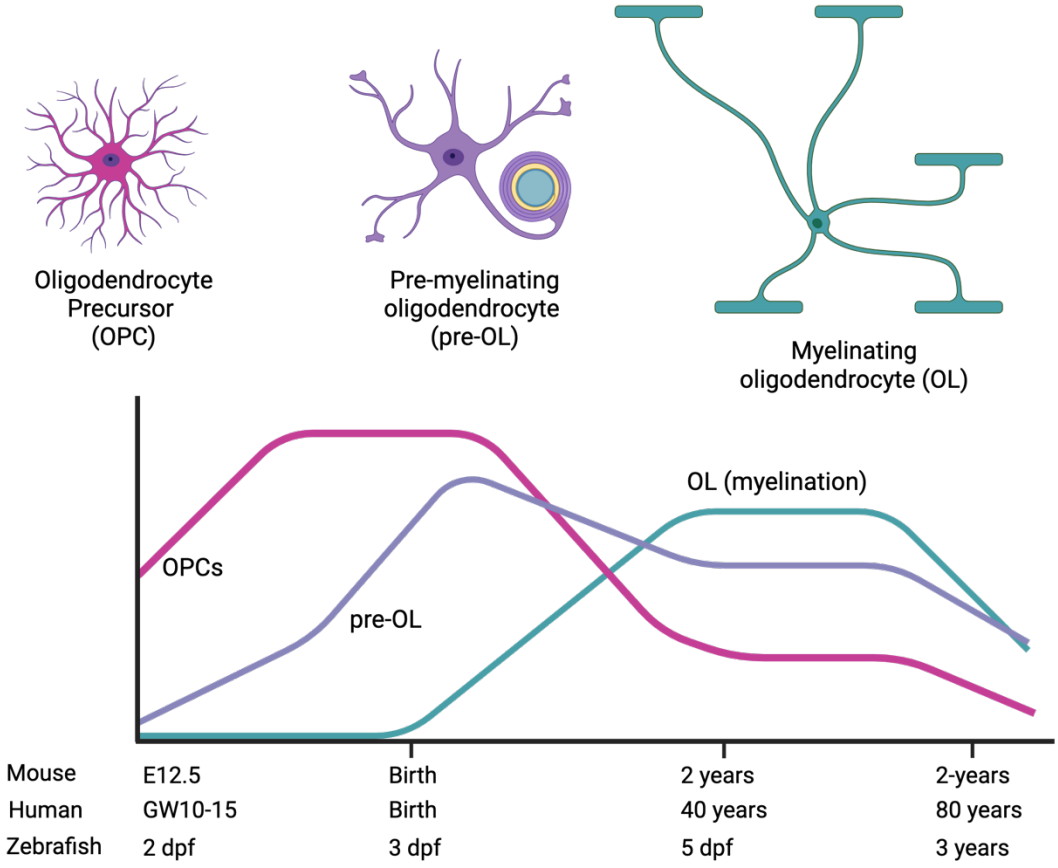
Oligodendrocyte Precursor (OPC)
Pre-myelinating oligodendrocyte (pre-OL)
Myelinating oligodendrocyte (OL)
OL (myelination)
OPCs
pre-OL
Mouse E12.5 Birth 2 years 2-years
Human GW10-15 Birth 40 years 80 years
Zebrafish 2 dpf 3 dpf 5 dpf 3 years

Figure 1.1 Developmental trajectories of OL lineage cells

Developmental progression of OL lineage cells in zebrafish, mouse, and human CNS. In all species, NPC give rise to OPCs (E12.5 in mouse, 10–15 gestational weeks (GW) in human, and ~2 dpf in zebrafish). OPCs migrate, proliferate, and differentiate into pre-OLs and then eventually into mature myelinating OLs.

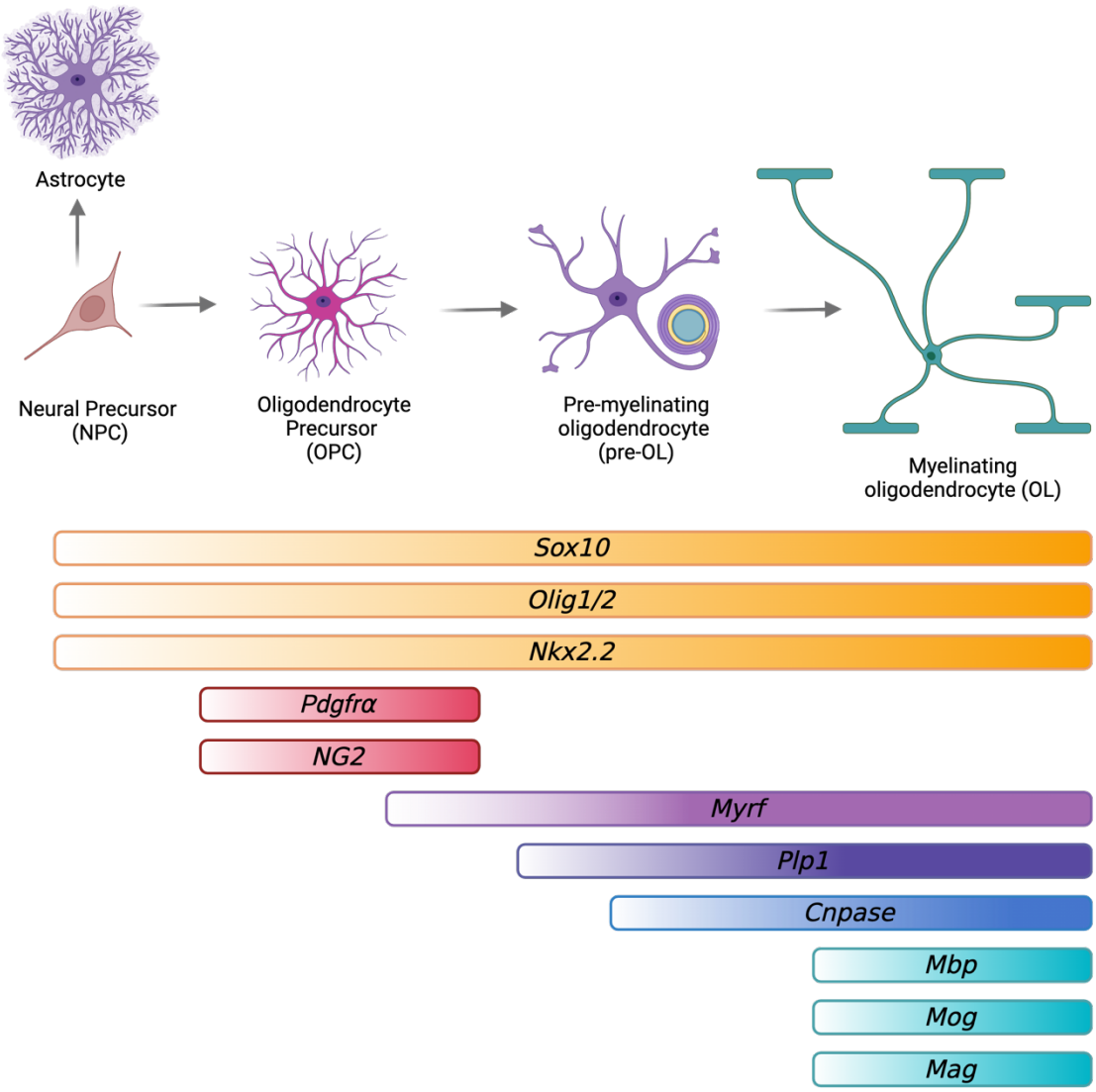
Astrocyte
Neural Precursor (NPC)
Oligodendrocyte Precursor (OPC)
Pre-myelinating oligodendrocyte (pre-OL)
Myelinating oligodendrocyte (OL)
Sox10
Olig1/2
Nkx2.2
Pdgfrα
NG2
Myrf
Plp1
Cnpase
Mbp
Mog
Mag

Figure 1.2 OL lineage markers

Developmental progression and molecular markers of OL lineage cells. Conserved transcriptional regulators (*Sox10*, *Olig1/2*, *Nkx2.2*) and stage-specific markers. OPC (*Pdgfra*, *Ng2*), pre-OLS (*Myrf*, *Plp1*,*Cnp*), differentiating OLs (*Mbp*, *Mog*, *Mag*) are shown along the timeline of lineage progression.

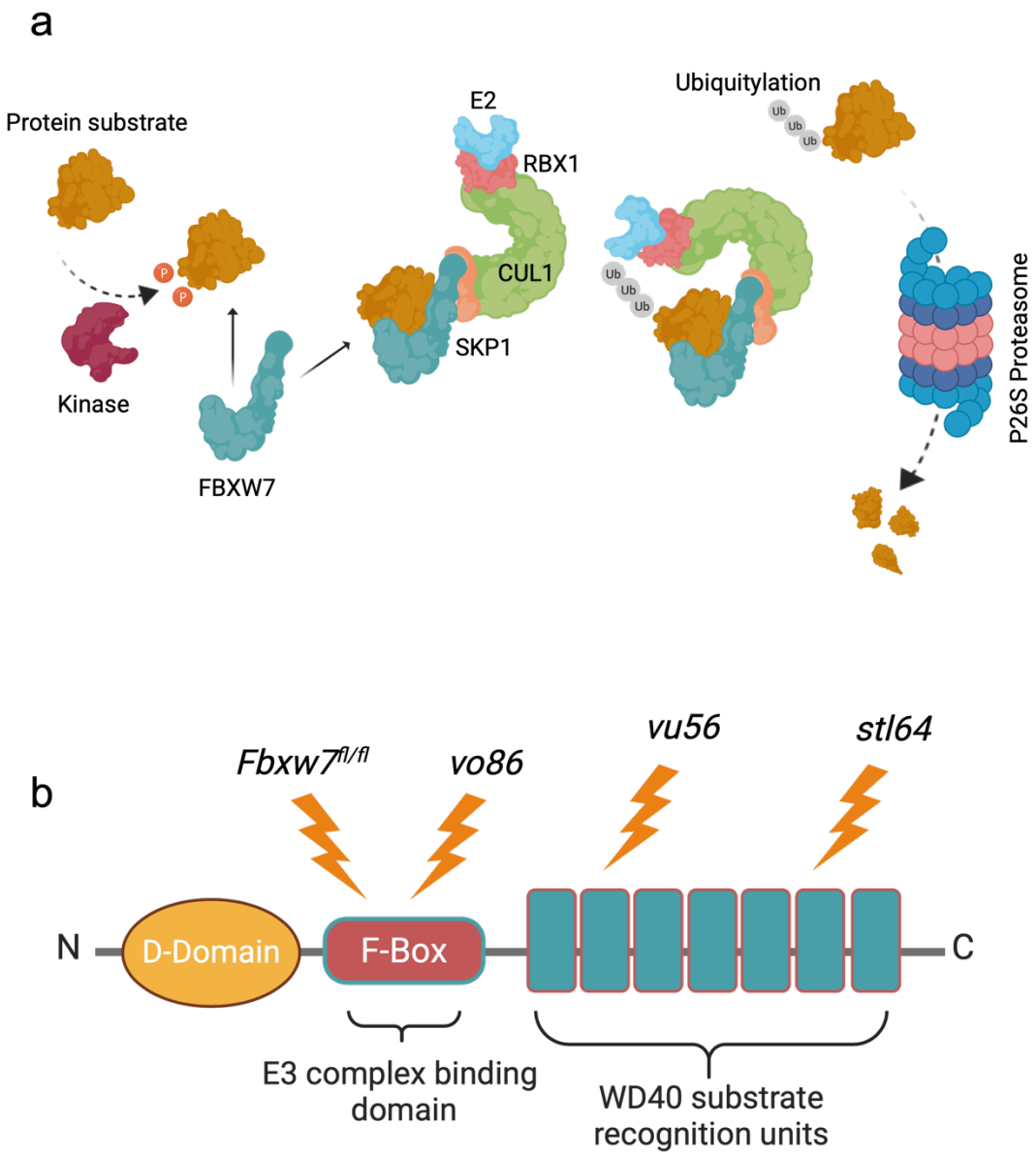
a
Protein substrate
Kinase
FBXW7
E2
RBX1
CUL1
SKP1
Ubiquitylation
Ub
P26S Proteasome
b
Fbxw7fl/fl
vo86
vu56
stl64
N
D-Domain
F-Box
C
E3 complex binding domain
WD40 substrate recognition units

Figure 1.3 Schematic of FBXW7-mediated substrate ubiquitination and domain architecture

a FBXW7 functions as the substrate recognition subunit of the SCF (SKP1–CUL1–F-box) E3 ubiquitin ligase complex, targeting phosphorylated substrates for ubiquitination and proteasomal degradation. Substrate binding occurs through recognition of phosphodegron motifs, followed by recruitment to the SCF complex, polyubiquitination, and subsequent degradation by the 26S proteasome. **b** Domain organization of FBXW7, highlighting the N-terminal D-domain, F-box domain for E3 ligase complex binding, and C-terminal WD40 repeats that mediate substrate recognition. Lightning bolts indicate relevant mutations in zebrafish (*stl64*, *vo86)* and location of LoxP sites the available mouse models.

VI. CHAPTER 2: METHODS

Zebrafish husbandry

All zebrafish experiments were done in compliance with the institutional ethical regulations for animal testing and research at Oregon Health & Science University (OHSU). *fbxw7*^{stl64}, *fbxw7*^{vo86}, and *myrf*^{eu70} zebrafish were maintained as heterozygotes. Experimental larvae were generated by incrosses to yield wild-type, heterozygous, and homozygous zebrafish. To create *fbxw7*$^{vo86/vo86}$; *myrf*$^{eu70/WT}$ animals, *fbxw7*$^{stl6/WT}$; *myrf*$^{eu70/WT}$ zebrafish were outcrossed to *fbxw7*$^{stl86/+}$. Zebrafish larvae are fed a diet of rotifers and dry food (Gemma 75) from 5 days post-fertilization (dpf) until 21 dpf. From 21 dpf until 3 months, fish are fed using rotifers and dry food (Gemma 150). Adult fish are maintained and fed with brine shrimp and dry food (Gemma 300). For larval zebrafish studies, sex cannot be considered as a biological variable as sex has not yet been determined.

Generation of *fbxw7*^{vo86} zebrafish mutants

CRISPR-Cas9 was used to generate genetic mutants in zebrafish. The CHOPCHOP web tool[234] was used to select target sites, and individual sgRNAs were synthesized using MEGAshortscript T7 Transcription kit (Thermo Fisher). The sgRNA GATGTAATCCGTCGTCTCTGTGG was mixed with Cas9 Nuclease (Integrated DNA Technologies) to a final concentration of 50 ng/mL sgRNA and 1 mg/mL of Cas9 protein and injected into one-celled zygotes at a volume of 1-2 nL. Progeny of injected F0 generation animals were screened for the presence of inherited indels resulting in frameshifts or truncations by PCR, and these F1 progenies were used to establish stable mutant lines. Genotyping for both larval

and adult zebrafish was performed by digesting tissue in Tris buffer with Proteinase-K overnight at 55ºC. PCR was performed with GoTaq DNA Polymerase (Promega, M300A). For *fbxw7*^{vo86} genotyping, PCR with (F-AAAATAGGGGCTTGCTCTGG, R- AAGTCCAGTTAAATTGAGAAGCC) was used to amply a 530 bp regain around indels. PCR products were digested with 10U of BsmBI-v2 (NEB, R0580) at 55ºC overnight and resolved on a 2% agarose gel. WT digestion products were 294 and 236 bp, with the undigested *fbxw7*^{vo86} band running at 530 bp.

Mosaic labeling and cell-type specific CRISPR-Cas9 gene disruption in zebrafish OLs

For mosaic labeling of OLs, *fbxw7*$^{vo86/+}$ zebrafish were incrossed, and fertilized one-cell zygotes were injected with 1-2 nl of a solution containing 10 ng of sox10:EGFP-caax plasmid, 25 ng of Tol2 transposase mRNA, 0.02% phenol red and 0.2 M KCl. Embryos were genotyped after imaging as described above. For cell-type specific CRISPR-Cas9-mediated gene disruption we utilized methods as previously described[77]. Briefly, sgRNAs targeting *fbxw7* exon 5 (GATGTAATCCGTCGTCTCTGTGG) and exon 7 (GCTGCCTGAAGCAGATCCTTTGG) were cloned into 10xUAS:myrmScarlet-p2A-Cas9, U6:sgRNA1;U6:sgRNA2 backbones and injected into *Tg(sox10:Kalta4)*[235] fertilized embryos at the one-cell stage. Empty backbones were used as controls. At desired timepoints, fish were anesthetized with 600 µM tricaine (TRS5, Pentair), screened for fluorescence, embedded laterally in 1.5% low-melting-point agarose (A9414, Sigma), and imaged with a 20x dipping

objective on a ZEISS LSM 980 with Airyscan 2. Sheaths were analyzed using ImageJ.

Mouse husbandry and tamoxifen (TAM) administration

All mice were housed in OHSU animal facilities, maintained in a pathogen-free temperature and humidity-controlled environment on a 12-hour light/dark cycle. All procedures were approved by the OHSU Institutional Animal Care and Use Committee. *Fbxw7*$^{fl/fl}$ mice[25] were previously purchased from Jackson Laboratories (B6;129-*Fbxw7*^{tm1Iaai}/J, JAX: 017563) and crossed to *Olig2*-Cre[236] (Olig2$^{tm2(TVA,cre)Rth}$/J, JAX:011103) or *Plp1-CreERT*[237] mice (B6.Cg-Tg[Plp1-cre/ERT]3Pop/J, JAX: 005975). *Myrf*$^{fl/fl}$ mice[151], maintained on a C57BL/6N background, were crossed into the *Plp1-CreERT-Fbxw7*$^{fl/fl}$ animals to create ***Plp1-Cre***^{ERT}***- Fbxw7***$^{fl/fl}$***; Myrf***$^{fl/wt}$ animals. CreERT negative littermates served as controls. To assess Cre-mediated recombination in the *Olig2-Cre* line, *Olig2-Cre* animals were crossed to Sun1:EGFP[238] mice to generate *Olig2*$^{wt/cre}$*-Sun1:EGFP*$^{wt/ki}$ (B6;129-Gt(ROSA)26Sortm5(CAG-Sun1/sfGFP)Nat/J, JAX: 021039). Genotypes were determined by PCR analysis using established primers for each line and were revalidated at experimental endpoints. Genotyping primers are listed in Table 2.2. All experiments were conducted in both male and female mice. For TAM injection, 8-week-old mice were dosed with 100 mg/kg tamoxifen (Sigma T5648, dissolved at 20 mg/ml in corn oil) for five consecutive days via intraperitoneal injection.

Tissue processing

Mice were terminally anaesthetized with ketamine (400 mg/kg) and xylazine (60 mg/kg) before being transcardially perfused with 20 mL of phosphate buffered saline (PBS) and 40 mL of 4% paraformaldehyde (19210, Electron Microscopy Sciences) in PBS. For immunofluorescence (IF), tissues were post-fixed in 4% paraformaldehyde in PBS (2 hours for optic nerves, overnight for brains) and cryopreserved in 30% sucrose for at least 72 hours at 4°C. Cortical flat mounts were processed as previously described[137]. Cryopreserved tissue was embedded in OCT (4583, Sakura), frozen on dry ice, and stored at -80°C until sectioning on a cryostat (Leica CM3050-S). Cryosections (12 µm thickness for brain, 16 µm for optic nerve) were mounted on Superfrost Plus slides (1255015, Fisher Scientific) and stored at -80°C. Tissue for transmission electron microscopy (TEM) was post-fixed in 2% paraformaldehyde (15710, Electron Microscopy Sciences) with 2% glutaraldehyde (16310, Electron Microscopy Sciences).

Immunofluorescence

Slides stored in -80°C were air dried for at least 2 hours before being rehydrated in 1x PBS. For MBP staining, tissue was delipidated by treating slides with ascending and descending ethanol solutions (50%, 75%, 85%, 95%, 100%) before being washed 3x in 1x PBS. Slides were blocked for 1 hr at room temperature with 10% fetal calf serum (SH30910.03, Cytiva) with 0.2% Triton X-100 (10789704001, Sigma). Primary antibodies were applied overnight in 1x PBS, 5% fetal calf serum and 0.2% Triton X-100 in a sealed container containing water at room temperature. The following primary antibodies were used: chicken anti-MBP (1:500; MBP,

Aves), mouse anti-CC1 monoclonal (1:500; OP80, Millipore), goat anti-PDGFRα (1:500; AF1062, R&D Systems), rabbit anti-IBA1 (1:1000; 019-19741, Wako), rabbit anti-GFAP (1:1000; Z0334, Dako), rabbit anti-MYRF (1:500; A16355, ABclonal), mouse anti-Calbindin1 (1:500; C9848, Sigma). Following incubation with primary antibodies, slides were washed 3x in 1x 0.2% Triton X-100 PBS before appropriate Alexa Fluor 488, 555, or 647 secondary antibodies (1:1,000; Invitrogen) were applied for one hour at room temperature. Slides were then again washed 3x with 1x 0.2% Triton X-100 PBS, washed in Milli-Q H_2O, air dried, then coverslipped with Fluoromount G (0100-01, Southern Biotech) and imaged.

Primary rat OLs were cultured on glass coverslips, fixed for 8 minutes in 4% PFA in PBS and stained in 24-well plates as described above. We used the following primary antibodies: chicken anti-MBP (1:500; MBP, Aves), rabbit anti-OLIG2 (1:500; AB9610, Millipore), and mouse anti-MAG (1:500; AB9610, Millipore). Coverslips were mounted with ProLong Diamond (P36965, Thermo Fisher) on Superfrost Plus slides.

Cortical flatmounts were sectioned at 40 µm and stored in PBS with 0.02% NaN_3 (sodium azide) at 4ºC. For staining, tissue was blocked in 10% fetal calf serum with 0.2% Triton X-100 for 2 hours with agitation at room temperature. Flatmounts were then incubated with primary antibodies at room temperature with agitation in 1x PBS 0.2% Triton X-100 for 4 days. We used the following primary antibodies: chicken anti-MBP (1:200; MBP, Aves), rabbit anti-CASPR (1:500; 34151-001, Abcam), and mouse anti-CNPase1 (1:500; MAB326, Millipore). Tissue was washed 3x 20 min 1x 0.2% Triton X-100 PBS. Alexa Fluor 488, 555 and 647

secondary antibodies (1:1,000; Invitrogen) were applied for two days at 4ºC protected from light. Tissue was washed 3x 20 min 1x 0.2% Triton X-100 PBS, slide mounted, rinsed in water, air dried, and coverslipped with Fluoromount G (0100-01, Southern Biotech). For quantification of sheath length from layer-I pSS, 280 µm x 280 µm x 30 µm images were taken of the pSS and 2 random ROIs were generated. All sheaths that passed through the ROIs were measured using ImageJ NeuroTracer in 3D.

Immunofluorescence from tissue was acquired on a ZEISS LSM 980 with Airyscan 2. Immunofluorescence from cultured OLs were imaged on Zeiss ApoTome2 at 20x. All cell counts and fluorescence intensities were quantified using ImageJ.

Isolation, expansion, and electroporation of primary rat OL precursor cells/OLs

Rat OL precursor cells (OPCs) were isolated from P6-8 Sprague Dawley rat pups as previously described[239]. OPCs from each animal were expanded in 3x 175cm^2 flasks for 3-4 days in the presence of 10 ng/mL platelet derived growth factor-aa (PDGFAA, Peprotech 100-13A). Cells were harvested fresh for each round of experiments and used at the time of first passage. OPCs were electroporated with Amaxa Basic Nucleofector Kit for Primary Mammalian Glial Cells (VPI-1006, Lonza) with 20 nM siRNAs/5 million OPCs or 4 µg of plasmid/5 million OPCs. siRNA pools for rat *Fbxw7* (L-115782-00-0005, Horizon), *Gsk3β* (L-080108-02-0005, Horizon), *Cdk5* (L-094624-02-0005, Horizon), or non-targeting controls (D-001810-10-05, Horizon) were used. Primary rat OLs were plated at 20k/coverslip

for staining, 250k cells/well of a 6-well plate for RNA, and 1 million cells/60x15 mm plate for protein isolation.

EdU incorporation and cycloheximide (CHX) treatment

Primary rat OPCs were expanded and electroporated with siRNAs and replated into proliferation media containing PDGFAA for 48 hours. Cells were pulsed with 10 μM 5-ethynyl-2'-deoxyuridine (EdU) for 6 hours. Cells were fixed with 4% PFA in PBS for 8 minutes at room temperature. Cells were stained with Click-iT EdU Cell Proliferation Kit with Alexa Fluor 647 dye (C10340, Thermo Fisher). siRNA electroporated OLs were differentiated for 3 days and treated with cycloheximide (CHX; 239763-M, Sigma) at 100 μg/mL for 4 hours to inhibit protein translation. Cell lysates were processed for western blot analyses as described below.

Transmission electron microscopy

Following post-fixation in 2% paraformaldehyde (15710, Electron Microscopy Sciences) with 2% glutaraldehyde (16310, Electron Microscopy Sciences), optic nerves and cerebellums were stored in a buffer of 1.5% paraformaldehyde, 1.5% glutaraldehyde, 50 mM sucrose, 22.5 mM $CaCl_2$ $2H_2O$ in 0.1M cacodylate buffer for at least seven days. Tissue was then infiltrated with 2% osmium tetroxide (19190, Electron Microscopy Sciences) using a Biowave Pro+ microwave (Ted Pella)[170] before dehydration in acetone and embedding in Embed 812 (14120, Electron Microscopy Sciences). 0.4 μm sections were cut on an ultramicrotome and stained with 1% Toluidine Blue (T161-25, Fisher Scientific) with 2% sodium borate (21130, Electron Microscopy Sciences). 60 nm sections were mounted on

copper grids (FCF100-Cu-50, Electron Microscopy Sciences) and counterstained with UranyLess for 5 minutes followed by 3% lead citrate (22409, 22410, Electron Microscopy Sciences) for 5 minutes. Grids were imaged at 4800x on an FEI Tecnai T12 transmission electron microscope with a 16 Mpx camera (Advanced Microscopy Techniques Corp). For g-ratio analysis, 5-8 images per animal were used. Outer myelin and axon diameters for g-ratio analyses were manually traced using ImageJ.

Cloning of dominant-negative 3xFLAG- FBXW7$^{\Delta F\text{-}Box}$

Fbxw7 coding sequence missing the F-Box domain with upstream 3x FLAG tags (3xFLAG- FBXW7$^{\Delta F\text{-}Box}$) was purchased as a double stranded gBlocks gene fragment from Integrated DNA Technologies (IDT) with KpnI + HindIII restriction enzyme overhangs. pCMV-SPORT-6 backbone and 3xFLAG- FBXW7$^{\Delta F\text{-}Box}$ inserts were digested with KpnI + HindIII restriction enzymes, gel purified, and ligated with T4 DNA ligase (EL0011, Thermo Fisher). Constructs were transformed into DH5α one-shot competent cells (12297016, Thermo Fisher) and purified with a PureLink HiPure plasmid maxiprep kit (K0491, ThermoFisher). pmaxGFP vector (Lonza) was used as a control for co-IP experiments.

Immunoprecipitation of FBXW7 dominant-negative constructs in cultured OLs

4 µg of CMV-3xFLAG-FBXW7$^{\Delta F\text{-}Box}$ and pmaxGFP were electroporated into rat OPCs. Cells were differentiated for 3 days and then lysed with cell lysis buffer (20mM Tris pH7.5, 150mM NaCl, 1% Triton X-100, 1mM EDTA, 1mM EGTA) with

cOmplete Mini Protease Inhibitor Cocktail (11836153001, Millipore) for 30 min at 4ºC with rotation. Lysates were spun at 4˚C for 10 min at 10,000 RPM. 5% of lysates were frozen for input controls. 4 µg of mouse anti-FLAG M2 antibody (F3165, Millipore) was added to lysates and rotated at 4˚C for 2 hours. 40 µL Dynabeads Protein G (10003D, Thermo Fisher) was added to lysates and rotated for 1 hour at 4˚C. Beads were sorted out with a magnetic rack and washed x5 with cell lysis buffer with rotation at 4˚C for 5 mins. Proteins were released from Dynabeads Protein G beads for LC-MS by boiling in 1% SDS. Proteins for western blots were boiled with 1x Laemmli buffer.

Western blots

For western blots on cultured OLs, plates were washed 3x with cold DPBS and lysed with RIPA buffer (50mM Tris-HCL pH 8.0, 150 mM NaCl, 1% NP-40, 0.5% Sodium deoxycholate, 0.1% SDS, 1 mM EDTA, 0.5 mM EGTA) with complete protease inhibitors (11836153001, Roche), and phosphatase inhibitors (04906837001, Roche) before being spun at 13,000 x g at 4ºC. Protein lysate was removed and frozen at -80ºC. Lysates were boiled at 98 ºC in 1x Laemmli buffer for 5 min and run on Bis-Tris-gel (NP0335BOX, Invitrogen). To transfer proteins to PVDF membranes (IPVH00010, Thermo Scientific), transfer cassettes were assembled (A25977, Thermo Fisher Scientific) and filled with transfer buffer (NP0006-01, Thermo Scientific) containing 10% methanol and run at 20V for 1hr. Following transfer, blots were rinsed in 1x TBS with 0.1% Tween-20 (TBST) before blocking in 1x TBST with 5% milk powder for one hour at room temperature. Blots were probed with antibodies against MYRF (16355, ABClonal), mTOR (2983, Cell

Signaling), Phospho-mTOR (Ser2448; 5536, Cell Signaling), cJUN (9261L, Cell Systems), TMEM98 (14731-1-AP, Proteintech), MYO1D (ab70204, Abcam), GSK3β (ab32391, abcam), DPYSL5 (CRMP5; ab36203, Abcam). All antibodies for western blots were used at a concentration of 1:1000. Blots were incubated in primary antibodies diluted in 2.5% BSA (BP9706-100, Fisher Scientific) with 1% NaN_3 in TBST overnight at 4ºC. After overnight incubation, blots were washed in 3x TBST and incubated with appropriate HRP-conjugated secondary (Goat anti-rat 7077, Cell Signaling; Goat anti-mouse 7076, Cell Signaling, Goat anti-rabbit 7074, Cell Signaling) at 1:5,000 for two hours with 2.5% milk powder in TBST. Immunoreactivity was visualized using chemiluminescence (34080, Thermo Fisher Scientific) and imaged on a Syngene GBox iChemiXT. Blots were then re-probed with β-actin-HRP (1:5000; A3854, Sigma). Densitometric analyses were performed in ImageJ by quantifying the intensity of bands relative to the ACTB loading control and then normalized to background.

Mass spectrometry and analysis

OLs electroporated with pooled siRNAs targeting *Fbxw7* or non-targeting controls were differentiated for 72 hours and lysed with eFASP buffer (4% SDS, 0.2% DCA, 100mM TEAB), frozen at -80 ºC, and submitted to the OHSU proteomic core. Samples were then sonicated using Bioruptor Pico (30s on 30s off, 10 cycles), heated to 90ºC for 10 mins, cooled, centrifuged, and protein concentration was determined by BCA. 55 µg of protein/sample were digested with eFASP and measured by peptide assay. 18 µg peptides/sample were labeled with TMT 11-plex, normalized, and pooled. Pooled TMT samples were then run on an 18

fraction 2dRPRP LC/MS on Orbitrap Fusion. Data was then analyzed with COMET/PAWS pipeline in edgeR.

OL samples from IP were prepared for proteomics analysis. Samples were dried on a SpeedVac and resuspended in 5% SDS, 50mM TEAB pH 8. Samples were reduced with dithiothreitol and alkylated with iodoacetamide. Proteins were bound to S-trap columns (Protifi, Inc.) where they were washed before being digested with trypsin. A Quantitative Colorimetric Peptide Assay (23275, Pierce) was performed. Peptides were analyzed by LC-MS on a Dionex Ultimate HPLC to an Orbitrap Q-Exactive mass spectrometer (Thermo Fisher Scientific, Waltham, MA).

qRT-PCR

RNA was isolated from primary rat OPC/OLs with the RNeasy Mini Kit (74104, QIAGEN) and stored at -80ºC. RNA from optic nerves and cerebellums were isolated by homogenizing tissue in 700 μl of TRIzol (15596026, Thermo Fisher). 140 μl of chloroform (J67241.K4, Thermo Fisher) was added to lysate and shaken for 30 seconds and left at room temperature for 5 minutes. Samples were then centrifuged for 15 minutes at 12,000 x g at 4ºC. The upper, colorless, aqueous phase containing RNA was then purified further with RNeasy UCP Micro (optic nerves) and Mini (cerebellums) Kits (73934, 74104, QIAGEN) and stored at -80ºC. cDNA was generated with SuperScript III First-Strand Synthesis (18080400, Thermo Fisher) and stored at -20ºC. qPCR was performed with PowerUP SYBR Green (A25742, Thermo Fisher) on a QuantStudio 6 Flex Real-Time PCR System

(4485691, Thermo Fisher). qRT-PCR primers were designed on the Integrated DNA Technologies (IDT) PrimerQuest program.

Quantification and statistical analysis

Myelin outfolds in the corpus callosum were quantified in ImageJ by image thresholding and particle analyses. MYRF IF in the optic nerve and cerebellum was quantified in ImageJ by overlaying DAPI mask on MYRF images followed by particle analyses for mean grey values. CC1+ cell in the cortex and corpus callosum were quantified manually. MBP+ wrapped NeuN+ cell bodies were quantified manually in the cerebellum. Western blots were quantified by densitometry in ImageJ. All bands were normalized to blot background and bands from proteins of interest were normalized to loading controls.

Statistical analyses were conducted with Prism 10 (Graphpad). In all cases the figure legend indicates the statistical test used and p-values are presented in figures. Sample size is stated in figure legends. Animals were assigned to group based on genotype by random selection and analyses were conducted blinded to genotype.

Mass spectrometry data was processed using the PAW pipeline[240] with the Comet search engine (version 2016.03)[241] searching versus the Rattus Norvegicus Uniprot database (UP000002494, Taxon ID:10116, one protein sequence per gene).

Data availability

Mass spectrometry data was processed using the PAW pipeline[240] with the Comet search engine (version 2016.03)[241] searching versus the *Rattus norvegicus* Uniprot database (UP000002494, Taxon ID:10116, one protein sequence per gene). The mass spectrometry proteomics data have been deposited to the ProteomeXchange Consortium via the PRIDE partner repository with the dataset identifier PXD063570 [242–244].

Table 2.1 – Zebrafish transgenic lines
Tg(mbp:eGFP-caax)[131]
Tg(olig2:dsRED)[245]
Tg(mbp-nls:eGFP)[134]
Tg(nbt:dsRED)[246]

Table 2.2 – mouse genotyping primers

Gene	Forward primer	Reverse primer	Size bp
$Fbxw7^{fl/fl}$	GGCTTAGCATATCAGCTATGG	ATAGTAATCCTCCTGCCTTGGC	497
$Fbxw7^{wt/wt}$	GGCTTAGCATATCAGCTATGG	ATAGTAATCCTCCTGCCTTGGC	315
Plp1-Cre^{ERT}	ATACCGGAGATCATGCAAGC	GGCCAGGCTGTTCTTCTTAG	200
Cre control	CTAGGCCACAGAATTGAAAGATCT	GTAGGTGGAAATTCTAGCATCATCC	324
$Myrf^{wt/wt}$	GGGAGGGGGCTTCAAGGAGTGT	CCCCCAGCATGCCGATGTACAC	460
$Myrf^{fl/fl}$	GGGAGGGGGCTTCAAGGAGTGT	CCTTTCGCCAGGGGGATCTTG	668
Sun1-EGFP	AAG TTCATCTGCAC ACCG	TCCTTGAAGAAGATGGTGCG	173

Olig2-Cre	GCG GTC TGG CAG TAA AAA CTA TC	GTG AAA CAG CAT TGC TGT CAC TT	100

Table 2.3 - qRT-PCR Primers

Gene	Forward	Reverse	Species
Myrf	CTTCCTTCTGGTCATCTCCTTG	GAGAGTGAAGGTGGGCAAATA	Mouse
Actb	GAGGTATCCTGACCCTGAAGTA	CACACGCAGCTCATTGTAGA	Mouse
Mbp	AGTCGCAGAGGACCCAAGAT	ACAGGCCTCTCCCCTTTC	Rat
Plp1	CACTTACAGCAGGTGATTAGAGG	AAACAAGAGATAAACAACTGGGA	Rat
Mog	GTCTATCGGCGAGGGAAAGGT	CACGGCGGCTTCTTCTTGGT	Rat
Myrf	CAGCAGTGGGAAAGGGAATAA	AACTCAGCTCCCGATAGAGAT	Rat
Tmem98	CAGTGTAACACCACGTCTACC	CTCGATTCTTAGAGGGCAACTC	Rat
Itgb3	GCTGTCCTGTATGTGGTAGAAG	CAGAGTAGCAAGGCCAATGA	Rat
Dpysl5	TCCATACCCACACCCTCATA	ACTCTCTCCTACTCTCCCTTTC	Rat
Myo1d	ACTTCAAGCGCCTCATGTATAA	CCTCTTGGTCACCTCTGTAATG	Rat
Fam107b	GAAGCACGAGAGCCGATTATAG	TCAAGGGCAAGCCATCTTAC	Rat
Vsnl1	TGTCTGGCCCACATACAATAC	CGAGAGGTTACAAATGAGGTAAGA	Rat
Pea15	ATGAAGACACAGGAGAGAGAGA	GTGAGTGTATTAGGGCAGGTTAG	Rat
Tppp	ACTGGGCAGAACTCAGAATG	CAATGAATCACGGCCCAAAC	Rat
Rpl13A	CTCATGATGACTGCAGCAAACC	GGATCCCTCCAC CCTATGACA	Rat
mbp	AATCAGCAGGTTCTTCGGAGGAGA	AAGAAATGCACGACAGGGTTGACG	Zebrafish
actb	CGAGCTGTCTTCCCATCCA	TCACCAACGTAGCTGTCTTTCTG	Zebrafish

VII. Chapter 3: FBXW7 regulates MYRF levels to control myelin capacity and homeostasis in the adult CNS

Hannah Y. Collins[1,2], Ryan A. Doan[2], Jiaxing Li[2,4], Jason E. Early[3], Megan E. Madden[3], Tyrell Simkins[1,2,5], David A. Lyons[3], Kelly R. Monk[2]*, Ben Emery[1]*

1. Jungers Center for Neurosciences Research, Department of Neurology, Oregon Health & Science University, Portland, Oregon 97239, USA

2. Vollum Institute, Oregon Health & Science University, Portland, Oregon 97239, USA

3. Centre for Discovery Brain Sciences, MS society Edinburgh Centre for MS Research, University of Edinburgh, Edinburgh EH16 4SB, UK

This chapter represents work under revisions at Nature Communications.

Author contributions

H.Y.C, T.S., K.R.M, and B.E. conceived of the project. H.Y.C designed, performed, and analyzed all experiments with the following exceptions: J.L generated the *vo86* zebrafish line (H.Y.C performed all validation experiments and analyses). J.L performed and analyzed the *fbxw7* cell-specific CRISPR-Cas9-mediated gene disruption in Fig. 1f-h. R.A.D processed and imaged optic nerve and cerebellum TEMs in Figs. 3 and 4. J.E.E and M.E.M. generated the *myrf*^{eu70} zebrafish line in Fig. 7d, I, and Supplemental Fig. 6b, and D.A.L. provided these mutants prior to publication. H.Y.C, K.R.M, and B.E. wrote the manuscript. All authors provided feedback on the manuscript and approved the submitted version.

Introduction

In the vertebrate CNS, myelin is produced by specialized glial cells called OLs. OLs wrap segments of axons, creating a multi-layered sheath that speeds the transmission of nerve impulses and provides critical support to axons[97,98,102,247]. The formation and targeting of myelin is influenced by external cues such as axonal caliber and neuronal activity, but is also tightly controlled by cell intrinsic programs[71,82,107,135,140,143,232,248]. As OL precursor cells (OPCs) differentiate from a dynamic and proliferative state into a relatively stable post-mitotic myelinating OL, they reorganize and expand their cytoskeleton, cytoplasm, and membrane[93,95,96], requiring significant transcriptional changes[20,91,141,151]. Although OLs are long-lived, surviving up to years in mice and decades in human white matter tracts, the myelin constituents themselves turn over comparatively rapidly, with a half-life of months[75,133,160,249]. Individual myelin sheaths can also be remodeled throughout life[107,109,250]. Therefore, understanding the molecular pathways and mechanisms that balance myelin growth and homeostasis is crucial for understanding myelin's role in health, aging, and disease.

Previous work from our lab and others has identified F-box and WD repeat domain-containing protein 7 (FBXW7) as a key negative regulator of developmental myelination by both Schwann cells in the peripheral nervous system (PNS) of mice and OLs in the CNS of zebrafish[212,221,225,228]. Within the PNS, FBXW7 regulates Schwann cell numbers, along with their myelin thickness[225]. Surprisingly, loss of *Fbxw7* also results in a breakdown of the normal 1:1 relationship between myelinating Schwann cells and axons, with individual *Fbxw7* conditional knockout

Schwann cells aberrantly myelinating multiple axons[225]. Within the CNS of zebrafish, *fbxw7* regulates neural stem cell fate through Notch1 signaling, biasing the cells towards an OPC fate and increasing the pool of OL lineage cells in the spinal cord[221]. At later stages, loss of *fbxw7* leads to increased myelin sheath length, attributed to dysregulation of mTOR signaling[228]. *Fbxw7* encodes the F-box domain containing recognition subunit of a SKP1-Cullin-Fbox (SCF) E3 ubiquitin ligase complex. It mediates its biological effects through targeting specific proteins for proteasomal degradation, thus controlling their total levels in the cell[221,228,251–253]. FBXW7 substrates are highly variable between cell types and have not yet been investigated in myelinating cells in an unbiased manner.

To interrogate the role of FBXW7 in the regulation of CNS myelination, we used a combination of zebrafish, primary mammalian OL cultures, and conditional knockout mouse models. We found that inactivation of *fbxw7* in developing zebrafish resulted in enhanced OL maturation in the spinal cord. Strikingly, conditional ablation of the *Fbxw7* in mature OLs in the adult mouse CNS increased myelin sheath lengths but also resulted in progressive myelin abnormalities including outfolds, disrupted paranodal organization, and ectopic ensheathment of neuronal cell bodies with myelin. We found that *Fbxw7* deficient OLs had no changes in mTOR protein levels in primary mammalian OL cultures, suggesting the myelin phenotypes were not a consequence of dysregulated mTOR signaling. Previous work in hepatocarcinoma cells identified the pro-myelination transcription factor Myelin Regulatory Factor (MYRF) as a target of FBXW7[229]. We demonstrate that the N-terminus of MYRF is a direct target of FBXW7 in OLs both *in vitro* and

in vivo, with levels of N-MYRF protein and many of its transcriptional targets substantially increased in *Fbxw7* deficient OLs. We also found that *Myrf* haploinsufficiency is sufficient to ameliorate both the increase in OL numbers in *fbxw7* knockout zebrafish, was well as myelin outfolds and ectopic myelination of granule cell in the cerebellum in our conditional knock-out mouse models. Taken together, our findings demonstrate that FBXW7 is an evolutionarily conserved negative regulator of OL myelination and that its negative regulation of MYRF in the adult CNS is required for long-term myelin homeostatic maintenance.

Results

Fbxw7 regulates OPC specification and OL myelination in the zebrafish spinal cord

In zebrafish, global *fbxw7* mutations cause hypermyelination in both the PNS and CNS[221,225,228]. Previously published zebrafish *fbxw7* mutant alleles are late mutations within the region of the gene encoding the WD40 substrate recognition domain of the FBXW7 protein; therefore, existing mutants may not be complete loss-of-function alleles[212,221]. We used CRISPR-Cas9-mediated genome editing to create a new mutation, *fbxw7*^{vo86}. This mutation introduces a frameshift and early stop codon in exon 5, which encodes the F-Box domain that allows FBXW7 to interact with its E3 complex (Fig. 3.1a, b). Through *in situ* hybridization, live imaging, and qPCR, we found that the *fbxw7*^{vo86} mutation phenocopies the previously described N-ethyl-N-nitrosourea (ENU)-generated *fbxw*^{stl64} mutants, including increased *myelin basic protein* (*mbp*) RNA levels and myelin intensity in the dorsal spinal cord (Fig. 3.1c-e, Fig. 3.2a, b). Since *fbxw7*^{vo86} phenocopies the original ENU-generated mutation, we concluded that both mutations represent full loss-of-function alleles. As the *fbxw7*^{vo86} mutation disrupts the F-Box domain, the same region targeted in the Fbxw7$^{fl/fl}$ mouse line[254] also used in our studies (described below), this allele was used for all subsequent analyses. In prior work, global disruption of *fbxw7* in zebrafish led to enhanced OPC specification through disinhibition of Notch1 signaling, observed as an increase in *mbp* expression and numbers of *olig2:dsRED*-expressing cells[221]. Consistent with this, *fbxw7*^{vo86} mutants present with a significant increase in mbp:EGFP-caax expression and

olig2:dsRED^{+} cell numbers in the developing dorsal spinal cord relative to wild-type controls at 2-, 3-, and 5-days post-fertilization (dpf) (Fig. 3.2a-c). To examine later stages of the OL lineage, we crossed *fbxw7*^{vo86} mutants into a transgenic Tg(mbp-nls:eGFP) line to label mature OL nuclei. Relative to wild-type clutchmates, the density of mbp-nls:eGFP-expressing cells was significantly increased in *fbxw7*^{vo86} mutants, even when normalized to the increased numbers of OL lineage cells (olig2:dsRED^{+}) at 3 dpf (Fig. 3.2a, d, e). Additionally, we found that *fbxw7*^{vo86} mutant zebrafish displayed a significant number of neuronal cell bodies in the spinal cord wrapped in *mbp*$^{+}$ membrane in the stable Tg(mbp-nls:EGFP); Tg(mbp:EGFP-caax) transgenic background at 3 dpf (Fig. 3.2f-h). While this phenotype may be due to the increase in OLs numbers in the zebrafish spinal cord as previously reported[136], it may also suggest that loss of FBXW7 broadly disrupts OL myelin membrane organization and targeting. To determine whether *fbxw7* could regulate myelination via an OL intrinsic mechanism, we utilized a cell-specific CRISPR-Cas9-mediated gene disruption system our lab had previously developed[77]. We found that *sox10*-driven disruption of *fbxw7* in sparsely targeted OL lineage cells resulted in a significant increase in myelin sheath lengths at 6 dpf, with no change in the number of sheaths formed per individual OL (Fig. 3.2i-k). These data suggest that *fbxw7* regulates OL myelination though a cell-autonomous mechanism in the developing zebrafish spinal cord.

FBXW7 regulates OL myelin sheath length, paranodal organization, and myelin homeostasis in both grey and white matter

Our findings in zebrafish indicated that *fbxw7* regulates key aspects of myelin growth early in development. Whether this role is conserved in mammalian CNS and whether Fbxw7 regulates myelination past these early developmental stages has not been explored to date. To address this, we created an inducible *Fbxw7* knockout (icKO) mouse by crossing *Fbxw7*$^{fl/fl}$ mice[254] to the Plp1-Cre^{ERT} line[237], allowing for tamoxifen (TAM) -inducible knockout of *Fbxw7* in mature OLs. The Plp1-Cre^{ERT} line is a transgenic line, animals heterozygous for Cre show no observable phenotypes in the CNS. *Fbxw7*$^{fl/fl}$*; Plp1-Cre*$^{ERT+}$ mice (*Plp1-Cre*^{ERT} *-Fbxw7*$^{fl/fl}$) and their CreERT negative littermate controls (*Fbxw7*$^{fl/fl}$) were treated with TAM at 8 weeks of age, and tissue was taken 1-, 3-, and 6-months post-TAM for subsequent analyses (Fig. 3.3a).

To determine if loss of *Fbxw7* in mature OLs regulated myelin sheath maintenance, we sectioned cortical flat-mounts of layer I and performed immunofluorescence (IF) for myelin basic protein (MBP; compact myelin), 2',3'-cyclic nucleotide 3' phosphodiesterase (CNP1; non-compact myelin), and contactin-associated protein (CASPR; paranodes). At 1-month post-TAM, *Plp1-Cre*^{ERT}*-Fbxw7*$^{fl/fl}$ OLs showed a significant increase in myelin sheath length in the primary somatosensory cortex (pSS) (Fig. 3.3b, c), indicating that FBXW7 regulates myelin capacity in mature OLs. Additionally, we observed an increase in the number of MBP/CNP1^{+} focal hyperintensities that appeared to be myelin outfolds, which increased significantly as the animals aged (Fig. 3.3d, e). To investigate FBXW7's role in white matter, we performed IF on *Plp1-Cre*^{ERT}*-Fbxw7*$^{fl/fl}$ optic nerves at 6-months post-TAM. We found a pronounced breakdown of nodal organization with

a significant broadening in the distribution of CASPR intensity and length at each heminode (Fig. 3.3f, g). While *Plp1-Cre^{ERT}-Fbxw7$^{fl/fl}$* animals had no change in weight or general health (Supplemental Fig. 3.4a, b), we observed a significant reduction of OL numbers in the upper cortex (layers 1-4) at 6 months post-TAM in *Plp1-Cre^{ERT}-Fbxw7$^{fl/fl}$* animals relative to their age-matched control littermates (Fig. 3.4c). Interestingly, this reduction was only observed above layer IV, with no change in OL numbers in deeper cortical layers or the corpus callosum (Fig. 3.4d, e). Additionally, we found no change in OPC numbers at any of these timepoints or regions (Fig. 3.4f-h), nor changes in astrocyte reactivity (Fig. 3.4i). Collectively, these data suggest that FBXW7 functions in many aspects of OL biology, from early modulation of sheath lengths to long-term maintenance of paranode organization and myelin homeostasis in mammalian OLs. Given that both grey and white matter tracts in *Plp1-Cre^{ERT}-Fbxw7$^{fl/fl}$* animals showed evidence of disrupted nodal organization and outfolds at 6-months post-TAM, we next wanted to assess the ultrastructure of the myelin. We therefore performed transmission electron microscopy (TEM) on optic nerves from *Plp1-Cre^{ERT}-Fbxw7$^{fl/fl}$* and *Fbxw7$^{fl/fl}$* littermate controls 6 months post-TAM. Consistent with our observations in layer I of the cortex, we also found a significant increase in the number of myelin outfolds in *Plp1-Cre^{ERT}-Fbxw7$^{fl/fl}$* optic nerves (Fig. 3.5a, b). While control animals did have outfolds at low frequencies, as expected at 8 months of age[109], the number and average length of outfolds in the *Plp1-Cre^{ERT}-Fbxw7$^{fl/fl}$* was significantly higher (Fig. 3.5b, c). Although myelin ultrastructure was disrupted in the optic nerve, we found no change in the proportion of axons myelinated or their corresponding g-

ratios when severe outfolds were excluded from analyses (Fig. 3.5d, e). Along with outfolds, we also observed other myelin abnormalities throughout the optic nerve including myelin whorls, cellular accumulations, and double myelin sheaths (sheaths enveloped by an overlying sheath) (Fig. 3.5f-h). This double myelination was also observed by IF in layer I of the pSS cortex, where we found CASPR^{+} paranodes under MBP^{+} myelin sheaths in *Plp1-Cre^{ERT}-Fbxw7$^{fl/fl}$* mice, suggestive of double myelinated axons (Fig. 3.5i). The outfolds in the white matter tracts of the optic nerve and corpus callosum were so severe they were also visible at the light level by IF in *Plp1-Cre^{ERT}-Fbxw7$^{fl/fl}$* animals as hyperintense MBP+ puncta (Fig. 3.6a-c). Additionally, we also observed myelin sheath blebbing and outfolds in *fbxw7^{vo86}* mutant zebrafish when injected with a sox10:eGFP-caax plasmid to label individual OLs at 5 dpf (Fig. 3.6d). Taken together, these data show that FBXW7 is a conserved regulator of myelin sheath length, which was independent of myelin sheath thickness, as well as long-term maintenance of myelin homeostasis and nodal organization.

Loss of *Fbxw7* in mature OLs results in ectopic ensheathment of neuronal cell bodies with myelin

Myelination within the CNS is highly targeted, with populations of axons displaying preferential degrees of myelination[109,137,255] and OLs typically not myelinating structures such as blood vessels and neuronal cell bodies[138,139,256]. There are also precise regional borders of myelination, as occurs in the cerebellum, which has distinct myelinated (granular layer) and non-myelinated (molecular layer) layers[257]. Exactly how this selective process is regulated is not well understood. We found

that loss of *Fbxw7* in mature OLs did not alter the tight delineation of myelination between the granular and molecular layers of the cerebellum, with the molecular layer remaining unmyelinated (Fig. 3.7a, Fig. 3.8a). Strikingly, however, *Plp1-Cre^{ERT}-Fbxw7$^{fl/fl}$* animals displayed a significant number of granule cell bodies within the nuclear layer wrapped in MBP^{+} membrane, which drastically increased over time post-TAM (Fig. 3.7a-d). This mistargeting of myelin appeared to be selective to the cerebellar granule cell population; we did not observe any neuronal cell bodies wrapped in myelin in the cortex, nor did we find other structures, such as blood vessels, wrapped in MBP^{+} membrane in any regions of the CNS analyzed. Additionally, we did not observe a change in the number of OLs in our *Plp1-Cre^{ERT}-Fbxw7$^{fl/fl}$* cerebellums compared to controls (Fig. 3.7e). It is important to note that Bergman glia in the cerebellum express *Plp1* and, therefore, may have undergone *Fbxw7* recombination in our *Plp1-Cre^{ERT}-Fbxw7$^{fl/fl}$* animals[171]. While we cannot exclude *Fbxw7* KO Bergman glia as a contributing factor in our granule cell body ensheathment, we did not observe any obvious change in the number or morphology of the Purkinje cells, which are supported by Bergman glia, at 6 months post-TAM in the cerebellum (Fig. 3.8a). Additionally, we found no change in GFAP expression (expressed by Bergman glia and astrocytes in the cerebellum) or reactivity of microglia (Fig. 3.8b). To assess whether the myelin ensheathment was due to myelination of the cell bodies, or severe myelin outfolds that wrapped around the small somas of the granule cells, EM was performed of the cerebellum of the 6-month post-TAM animals. High-resolution IF imaging of MBP and NeuN (Fig. 3.7f) combined with TEM (Fig. 3.7g), showed that the observed

ensheathment of the granule cells with myelin was likely due to excessive myelin outfolds in *Plp1-Cre*^{ERT}*-Fbxw7*$^{fl/fl}$ animals. Since this ensheathment was not observed in any other area of the CNS analyzed, it is likely due to the high density and small size of the granule cell soma in the cerebellum. In addition to myelin outfolds, large cellular accumulations were also observed in putative Purkinje neuron axons in the *Plp1-Cre*^{ERT}*-Fbxw7*$^{fl/fl}$ animals (Fig. 3.7h). These accumulations have been previously shown to occur in Purkinje axons after Purkinje cell-type specific deletions of cathepsin D (CTSD), which resulted in a significant increase in stressed and apoptotic Purkinje cells[258]. Taken together we have shown that loss of *Fbxw7* in myelinating OLs of the cerebellum resulted in large outfolds that encircled and enwrapped the cell bodies of the granule cells, while also causing axon pathology.

FBXW7 binds and degrades the N-terminus of MYRF

FBXW7 is a recognition subunit of the SKP1-Cullin-Fbox (SCF) E3 ubiquitin ligase complex. Its role is to recognize protein substrates following their phosphorylation at a phosphodegron motif, bringing them into the complex for ubiquitin tagging and subsequent proteasomal degradation[251,252,254,259]. This raised the question of which FBXW7 substrates are dysregulated in OLs after deletion of *Fbxw7* to result in accelerated and ectopic myelin formation. As a preliminary analysis, we selected a set of known FBXW7 substrates from multiple cell types including mTOR, JNK, and cJun that are also known to regulate myelination[225,228,251,260] and screened them by western blot in si*Fbxw7*-treated rat primary OL cultures. Surprisingly, we found no detectable changes in protein levels of mTOR, p-mTOR^{ser2448}, JNK, or

cJun (Fig. 3.10a). To screen for FBXW7 substrates in OLs in an unbiased manner, we generated a dominant-negative FLAG-tagged version of FBXW7 missing its F-Box domain, driven under the CMV promoter (Fig. 3.9a). The F-Box domain of FBXW7 is required for its interaction with the SCF-E3 complex, allowing FBXW7 to disengage from its substrates[229,259]. Deletion of the F-Box domain while leaving the substrate recognition domains (WD40 repeats) intact results in a buildup of the 3xFLAG-FBXW7$^{\Delta F\text{-}Box}$ protein bound to its substrates, allowing for effective protein-protein pulldown[229]. We electroporated primary rat OPCs with CMV-3xFLAG-FBXW7$^{\Delta F\text{-}Box}$ or pMax-GFP controls and differentiated them for 3 days (at which point approximately 60-70% of the Olig2^{+} cells are MBP^{+}). We then lysed cells, performed co-immunoprecipitation (co-IP) with an anti-FLAG antibody and assessed the eluted proteins using unbiased Liquid Chromatography-Mass Spectrometry (LC-MS) (Fig. 3.9b). FBXW7 and MYCBP2, a known E3-independent negative regulator of FBXW7[261], were the most highly enriched proteins by LC-MS, validating the effectiveness of our pulldown. We also found that FBXW7$^{\Delta F\text{-}Box}$ bound MAP1B (a microtubule-associated protein), RAE1 (an RNA export protein), MYRF (a pro-myelination transcription factor), and MYO1D (an unconventional myosin). Of these targets, MYRF seemed the best-placed to mediate the phenotypes seen following loss of *Fbxw7*, and so it became our subsequent focus.

MYRF is initially produced as an endoplasmic reticulum (ER)-bound transmembrane protein. It undergoes a self-cleavage event allowing the N-terminal cleavage product (N-MYRF) to translocate to the nucleus, where it works

with SOX10 at the enhancers of many essential myelin genes to promote their transcription[150,161,164,166]. MYRF levels are tightly controlled within the OL lineage, and its expression is essential for OL differentiation as well as the production and maintenance of compact myelin[151,163,170,262]. Notably, MYRF has recently been reported as an FBXW7 target in hepatocarcinoma cells, suggesting the interaction may be broadly conserved across cell types[229]. While *Myrf* is expressed in the liver, its exact function in this tissue remains to be determined. To confirm the MYRF interaction with FBXW7 in primary OLs, we performed western blots on 3xFLAG-FBXW7$^{\Delta F\text{-}Box}$ co-IPs. Pull-down with anti-FLAG strongly enriched for endogenous N-MYRF, but not full-length MYRF (Fig. 3.9c). To determine the effects of this interaction on MYRF levels, we electroporated primary rat OPCs with si*Fbxw7* and siControl, differentiated them for 24-48 hours, and blotted for endogenous N-MYRF. Knockdown of *Fbxw7* led to a substantial increase in the levels of N-MYRF, consistent with FBXW7's role in proteasomal degradation[263] (Fig. 3.9d). To confirm that the increased N-MYRF levels were due to decreased degradation in the absence of FBXW7, we treated siControl and si*Fbxw7* OL cultures with cycloheximide (CHX) to inhibit protein translation. We found that after 4 hours of CHX treatment, control cells had degraded the majority of both full-length MYRF and N-MYRF. In contrast, *Fbxw7* knockdown cells showed little reduction in N-MYRF levels, but near complete loss of the full-length protein (Fig. 3.9e, f). Together, these findings strongly supported a role for FBXW7 in N-MYRF degradation.

When analyzing the N-MYRF blots we noticed two distinct molecular weights of N-MYRF separated by ~2 kDa, with the higher molecular weight band becoming more prevalent with *Fbxw7* knockdown (Fig. 3.9d, e). Nakayama and colleagues found that phosphorylation of N-MYRF at serine 138 and 142 by GSK3β was required for FBXW7 to interact with N-MYRF[229]. Additional analyses of N-MYRF at serine 138 and 142 by sequence analyses predicted CDK5 as an additional potential mediator of N-MYRF phosphorylation. To determine whether build-up of a phosphorylated form of N-MYRF accounted for the observed change in molecular weight, control and si*Fbxw7* OL lysates were treated with a lambda phosphatase, and molecular weights were evaluated by western blot (Fig. 3.10b). We found that treatment with phosphatase resulted in a near total loss of the larger molecular weight N-MYRF in both control and si*Fbxw7* OLs, consistent with phosphorylated N-MYRF constituting the majority of the increased N-MYRF in our *Fbxw7* knockdown OLs. To determine if GSK3β or CDK5 were the kinase responsible for phosphorylating the phospodegron motif in N-MYRF to induce its interaction with FBXW7, we electroporated OPC cultures with pooled siRNAs against *Gsk3b, Cdk5,* or both, and differentiated them for 3 days. We found no change in the level of N-MYRF or corresponding myelin proteins (Fig. 3.10c) in any of the knockdown conditions. While the GSK3β antibody showed a non-specific band around 50 kD, the band with a predicted molecular weight band corresponding to GSK3β showed effective protein knockdown. Additionally, knockdown efficacy for siRNA against *Fbxw7*, *Gsk3β*, and *Cdk5* was >60% as determined by qRT-PCR (Fig. 3.10d). Together, these data suggest that although

N-MYRF is phosphorylated in OLs and that this phosphorylated form is the target of FBXW7, this occurs through a GSK3β- and CDK5-independent mechanism.

Given MYRF's well-defined role in OL differentiation and myelination we next wanted to investigate the functional consequences of elevated MYRF levels in *Fbxw7* knockdown OLs. si*Fbxw7*-electroporated OLs differentiated for 48-72 hours showed a significant increase in the proportion of MBP^+ and myelin-associated glycoprotein $(MAG)^+$ cells compared to controls (Fig. 3.9g-i). In addition to an increased proportion of cells expressing myelin proteins, cultures also showed significant increases in *Mbp*, *Mag*, and *Plp1* mRNA as assessed by qRT-PCR (Fig. 3.9j). To determine if loss of *Fbxw7* in OPCs affected proliferation, si*Fbxw7* and control OPCs were kept in proliferation media for 2 days after siRNA electroporation to allow for effective knockdown, then pulsed with 5-ethynyl-2'-deoxyuridine (EdU) for 6 hours. Within that time, approximately 40% of OPCs had undergone a round of division, with no significant change seen in EdU incorporation between si*Fbxw7* or siControl treated OPCs (Fig. 3.9k), indicating that loss of *Fbxw7* in OPCs was not sufficient to induce *Myrf* expression and the transition to a post-mitotic OL. These results indicate that once OPCs begin to differentiate and express *Myrf*, FBXW7 serves to regulate N-MYRF protein levels to control the balance and timing of OL myelination.

To further understand the consequences of loss of *Fbxw7* on the OL proteome, we performed LC-MS on lysates from si*Fbxw7* and siContol electroporated rat OLs at 3 days of differentiation. Cell lysates were labeled with tandem mass tags (TMT), pooled, and run through LC-MS. Over 2,700 proteins were sequenced with an R^2

value of 0.99-1 within treatment groups. Select enriched proteins with validated antibodies were confirmed by western blot (Fig. 3.10e). We found that *Fbxw7* knockdown in primary OLs resulted in significant changes in 253 proteins with a false discovery rate (FDR) <0.01 and 426 proteins with an FDR <0.05. Within the 253 proteins with an FDR <0.01, 158 proteins showed increased levels with *Fbxw7* knockdown and 95 showed reduced levels (Appendix I). Proteins with significant changes and a fold change greater than $\pm$1.2 were sorted by Gene Ontology functions “lipid metabolism,” “myelin,” and “adhesion” (Fig. 3.9l-n) to provide a list of proteins with potential roles in FBXW7-dependent myelination.

During OL differentiation, N-MYRF directly binds the enhancer regions of genes underpinning myelination, with enrichment of N-MYRF chromatin-immunoprecipitation (ChIP) peaks seen within 50 kb of the transcription start sites of genes induced during OL differentiation[166]. Notably, when the proteins were ranked by fold change following *Fbxw7* knockdown, 7 of the top 10 upregulated proteins and 73% of all proteins with fold change >1.5 had a predicted N-MYRF binding motif within 50 kb of the transcriptional start site of their corresponding gene (Fig. 3.9o). When we assessed RNA from corresponding samples by qPCR, we found that all the top 10 enriched proteins showed significant increases in their transcript levels with *Fbxw7* knockdown, suggesting that many of the changes in protein abundance following loss of *Fbxw7* were secondary to elevated MYRF transcriptional activity (Fig. 3.9f). Interestingly, we observed that *Myrf* RNA was significantly down regulated in the si*Fbxw7* treated cells compared to controls over

time, suggesting an additional mechanism(s) by which OLs regulate N-MYRF levels (Fig. 3.10g).

Loss of *Fbxw7* in OLs increases nuclear MYRF levels *in vivo*

We next sought to determine whether the myelin changes seen in *Plp1-Cre^{ERT}-Fbxw7$^{fl/fl}$* mice may be mediated by elevated MYRF levels. Since the antibody we used to detect MYRF recognizes an epitope within the N-terminal 100 amino acids of MYRF, it recognizes both the full-length form, which is bound to the ER, and the N-terminal cleavage product, which is translocated to the nucleus[164,166]. To determine the abundance of each, we use the cellular localization of the cytoplasmic (full-length) or nuclear (N-terminal) for quantification of MYRF levels in *Plp1-Cre^{ERT}-Fbxw7$^{fl/fl}$* and control optic nerve OLs. In *Plp1-Cre^{ERT}-Fbxw7$^{fl/fl}$* animals, we found a significant increase in the levels of nuclear-MYRF relative to their control littermates at 1- and 3-months post-*Fbxw7* deletion (Fig. 3.11a, b, d). Interestingly, the levels of nuclear MYRF in *Plp1-Cre^{ERT}-Fbxw7$^{fl/fl}$* optic nerves returned to control levels by 6 months post-TAM. This was associated with a significant reduction in the ratio of cytoplasmic to total (nuclear + cytoplasmic) MYRF levels (Fig. 3.11e). Hypothesizing that this reduced ratio of full-length MYRF to nuclear MYRF may represent a homeostatic response by the OL to control MYRF protein levels in the absence of FBXW7 by down-regulating *Myrf* transcription, we first performed qRT-PCR for *Myrf* transcripts in the si*Fbxw7* electroporated rat OLs *in vitro*, finding a significant reduction relative to siControl electroporated cells from 5 days post-knock down (Fig. 3.10g). To determine whether *Myrf* mRNA was also reduced *in vivo*, we isolated from optic nerves from

1- and 12-months post-TAM animals. At 1-month post-TAM there was a 62.7% reduction in *Myrf* transcript levels compared to controls. This reduction persisted at 12-months post-TAM, which showed a 61.5% reduction in *Myrf* levels compared to age-matched controls (Fig. 3.11f).

To determine if the increase in MYRF protein levels were seen throughout the CNS, we next evaluated MYRF levels in the cerebellum. We found significantly increased MYRF levels across 1-, 3-, and 6-months post-TAM (Fig. 3.11c, g). Since MYRF levels remained elevated at 6-months post-TAM in the cerebellum, we wondered if this would lead to a continued accumulation of myelin ensheathed granule cells in our aged 12-month post-TAMed animals. Indeed, we found that there was a 4-fold increase in the number of ensheathed granule cell bodies between 6- and 12-months post-TAM in *Plp1-Cre^{ERT}-Fbxw7$^{fl/fl}$* animals (Fig. 3.11h). As in the optic nerve, there was also a significant decrease in *Myrf* transcript levels in the cerebellum of *Plp1-Cre^{ERT}-Fbxw7$^{fl/fl}$* animals at both 1- and 12-months post-TAM compared to age matched controls. Taken together these data demonstrate that FBXW7 negatively regulates MYRF protein levels within OLs across the life span of the animal, and that loss of FBXW7, and corresponding increases in MYRF protein levels, triggers an additional mechanism(s) that downregulates the transcription of *Myrf* in an attempt to balance the levels of this important transcription factor.

Myrf haploinsufficiency rescues myelin phenotype in zebrafish and mouse models

The elevation of N-MYRF proteins levels in *Plp1-Cre^{ERT}-Fbxw7$^{fl/fl}$* animals, combined with the significant downregulation of *Myrf* RNA *in vivo* and *in vitro*, strongly suggested that elevated N-MYRF levels may underlie the aberrant myelination seen following loss of *Fbxw7.* Since *Fbxw7* loss of function OLs appear to utilize an additional mechanism(s) to down regulate *Myrf* RNA, we wondered if crossing our *Plp1-Cre^{ERT}-Fbxw7$^{fl/fl}$* mutant animals into a *Myrf* heterozygous background would reduce the burden of N-MYRF protein levels and rescue *Fbxw7* KO myelin phenotypes. To address this we crossed our Plp1-Cre^{ERT}-Fbxw7$^{fl/fl}$ animals into the established *Myrf$^{fl/fl}$* line[151] to create both *Plp1-Cre^{ERT}-Fbxw7$^{fl/fl}$; Myrf$^{fl/wt}$* and *Plp1-Cre^{ERT}-Fbxw7$^{fl/fl}$; Myrf$^{wt/wt}$* mice line along with their CreERT negative littermate controls (*Fbxw7$^{fl/fl}$; Myrf$^{fl/wt}$*). TAM was administered at 8 weeks of age, and tissue was harvested at 1-, 3-, and 6-months post-TAM for subsequent analyses.

At 3-months post-TAM, when we observed the largest increase in MYRF protein levels in *Fbxw7* icKO optic nerves, we observed a significant decrease in MYRF intensity in *Plp1-Cre^{ERT}- Fbxw7$^{fl/fl}$; Myrf$^{fl/wt}$* animals compared to icKO animals (Fig. 3.12a, e). We next evaluated Myrf levels in the cerebellum. Again, we found that *Plp1-Cre^{ERT}- Fbxw7$^{fl/fl}$; Myrf$^{fl/wt}$* animals had a significant decrease in MYRF staining intensity at 6-month post-TAM (Fig. 3.12b, f). To determine if an additional floxed allele in our Plp1-CreERT animals reduced *Fbxw7* recombination, we performed qRT-PCR on the optic nerves in our *Plp1-Cre^{ERT}- Fbxw7$^{fl/fl}$; Myrf$^{fl/wt}$* 1-month post-TAM animals. We found no significant change in *Fbxw7* expression between *Fbxw7* icKO and *Plp1-Cre^{ERT}- Fbxw7$^{fl/fl}$; Myrf$^{fl/wt}$* animals at 1-month post-

TAM (Fig. 3.13a). We next wanted to assess how *Myrf* haploinsufficiency and normalization of MYRF protein levels would influence the myelin phenotypes observed in *Fbxw7* icKO mice. We found a significant decrease in granule cell bodies ensheathed by myelin outfolds in *Plp1-Cre^{ERT}- Fbxw7$^{fl/fl}$; Myrf$^{fl/wt}$* animals compared to *Fbxw7* icKO animals in the cerebellum at both 3- and 6-months post-TAM (Fig. 3.12b, h). Additionally, deletion of one allele of *Myrf* was sufficient to prevent the increase in myelin outfolds present in layer I of the pSS in *Fbxw7* icKO animals at 6-months post-TAM by IF (Fig. 3.12c, g).

To test if the epistatic relationship between *myrf* and *fbxw7* is evolutionarily conserved in zebrafish OLs, we crossed the *fbxw7$^{vo86/vo86}$* line to a *myrf* mutant line (*myrf$^{eu70/WT}$*)[231] to determine if reducing *myrf* levels could suppress *fbxw7* mutant phenotypes *in vivo*. At 3 dpf, we observed a significant reduction in the number of *mbp:nls-EGFP*$^{+}$ OLs in the spinal cord of *fbxw7$^{vo86/vo86}$, myrf$^{eu70/WT}$* animals compared to *fbxw7$^{vo86/vo86}$* mutants alone (Fig. 3.12d, i) as well as neuronal myelin ensheathment (Fig. 3.13b). These data, along with our work in primary OL cultures and conditional KO mouse models show that FBXW7 is an evolutionarily conserved negative regulator of N-MYRF in OLs required for many facets of OL biology, from OL sheath length, paranodal organization, to long-term homeostatic maintenance of myelin.

Discussion

FBXW7 regulation of myelin homeostasis

Here we present evidence that once cells are committed to the OL lineage, FBXW7 regulates OL myelin capacity, organization, and homeostasis, in part through the

negative regulation of the N-MYRF transcription factor. With the temporal control of inducible conditional knock-out mice we found that loss of *Fbxw7* in myelinating OLs resulted in increased myelin sheath length, severe myelin outfolds, disorganized paranodes, and surprisingly, wrapping of neuronal cell bodies in the cerebellum by severe outfolds. These phenotypes are particularly striking since *Fbxw7* was targeted in mature OLs, indicating that inactivation of FBXW7 reinitiates aspects of myelin growth in the adult CNS. While myelin sheath plasticity has been reported in the context of axonal activity[77,81,232], the underlying mechanisms that regulate these changes have not been fully characterized. Because loss of *Fbxw7* results in changes to many adhesion and cytoskeletal proteins, it is possible that FBXW7-mediated negative regulation of OL proteins may represent one of these underlying mechanisms of plasticity, potentially though its regulation of N-MYRF and its transcriptional targets.

Ensheathment of neuronal cell bodies occurs in zebrafish when OL numbers exceed their normal balance to receptive axons[136]. It is entirely possible that the increase in ensheathed neuronal cell bodies we observe in the *fbxw7*^{vo86} zebrafish is a consequence of increased OPC specification and OL numbers[221]. In contrast, myelin outfolds that ensheathed the cerebellar granule cell bodies of *Plp1-Cre*^{ERT}-*Fbxw7*$^{fl/fl}$ mice was not accompanied by an increase in the density of OLs, so is unlikely to be mediated by a mismatch between the myelinating cells and their targets. Interestingly, we did not observe myelin outfolds wrapping cell bodies or other structures in the cerebral cortex of *Plp1-Cre*^{ERT}*-Fbxw7*$^{fl/fl}$ animals, although outfolds were present. Why cerebellar granule cell bodies were the only observed

neurons wrapped in myelin outfolds in the *Fbxw7* conditional knockouts is puzzling. Perhaps the density and/or size of cerebellar granule cells makes them especially susceptible to ensheathment by redundant myelin outfolds. Indeed, ensheathment of granule cell bodies has also been observed in the normal development of the toad[264] and squirrel monkey cerebellum[265], following N-WASP inactivation within the OL lineage cells[266], and with over-expression of the extracellular domain of Cadm4 adhesion protein in OLs[267]. While aberrant cell body myelination has also been observed in the spinal cord of global KO of myelin-guidance protein JAM2, this was believed to driven by neuronal loss of JAM2[138]. Since the granular layer of the cerebellum is the primary region where cell body myelination is observed when OLs are targeted, it suggests that the unique architecture of this region is highly prone to ectopic myelin placement. Additionally, our findings that *Fbxw7* loss of function myelin causes putative Purkinje axon pathology also leads to interesting question of how this inappropriate myelin may affect the health and function of the underlying neurons and circuitry.

In Schwann cells, FBXW7 regulates myelin sheath thickness, with no obvious change to sheath length[225]. In OLs these roles seem to be reversed, with FBXW7 regulating myelin sheath length but not thickness. Although this may be due to inherent differences in the biology of these two cell types, it may also be due to the differences in the tools used to evaluate its function. In our prior Schwann cell work, *Fbxw7* was constitutively deleted in development using Desert hedgehog Cre (*Dhh-Cre*), which is expressed in Schwann cell precursors as early as E12.5[204,225]. In contrast, here we used a TAM-inducible system to delete *Fbxw7* from

myelinating OLs in 8-week-old Plp1-CreERT mice. Whether the effects of *Fbxw7* on myelination would change depending on the timing of OL deletion remains unclear but is an exciting proposition for future work.

Divergent FBXW7 targets across the OL lineage

Our studies and others highlight the complicated role FBXW7 plays in myelinating cell biology across species and cell types. *Fbxw7* is widely expressed in most, if not all cell types in the CNS, and its biological functions depend on the available substrates within each cell[259,263,268]. Therefore, FBXW7 is likely to have distinct targets and diverging roles at different stages of the OL lifespan. For instance, FBXW7 negatively regulates Notch1 levels in neural precursor cells (NPCs), to control OPC specification in zebrafish[221]. The same group also found that in later stages of the OL lineage, FBXW7 negatively regulates mTOR to control myelination in the spinal cord of zebrafish. Likewise, we previously showed that in the mammalian PNS, FBXW7 regulates early Schwann cell numbers, axonal ensheathment, and myelin thickness in an mTOR-dependent manner[225]. In contrast, here we present evidence that in mammalian OLs, mTOR was not a direct target of FBXW7, with knockdown of *Fbxw7* resulting in no detectable change in mTOR protein abundance, phosphorylation, or downstream signaling. Using an unbiased pull-down and LC-MS approach, we instead identified several direct FBXW7-interacting proteins in primary OLs; MYCBP2, MAP1B, RAE1, and MYRF. Of these, MYCBP2 was a previously identified FBXW7 interactor that likely inhibits its activity independent of the E3 complex[261]. Although we focus here on

MYRF, MAP1B and RAE1 also represent intriguing FBXW7 targets within myelinating cells for future studies.

Despite its well-established role as a substrate adaptor in the SCF E3 ubiquitin ligase complex, the upstream regulation of Fbxw7 in the OL lineage remains poorly defined. In other systems, *Fbxw7* transcription is positively regulated by p53 and negatively modulated by cell cycle-associated factors such as E2F1[216,219]. Additionally, multiple microRNAs, including miR-223, miR-27a, and miR-25, have been shown to suppress *Fbxw7* expression post-transcriptionally by targeting its 3' UTR[269,270]. While these regulatory mechanisms have been primarily studied in cancer and stem cell contexts, it is plausible that similar pathways operate in OLs to modulate Fbxw7 expression in response to differentiation cues, cellular stress, or metabolic demand. Elucidating how Fbxw7 is transcriptionally and post-transcriptionally controlled in myelinating glia may provide critical insight into how OLs fine-tune their proteome to maintain myelin integrity and respond to environmental changes.

Regulation of MYRF

As a critical regulator of OL differentiation and myelination, MYRF levels appear to be tightly regulated within the OL lineage. Not only is MYRF subject to tight transcriptional regulation by SOX10 and ZFP24[271], but its mRNA is subject to negative regulation by miR-145-5p in OPCs, presumably to discourage premature differentiation[272]. While we have shown that loss of FBXW7 results in an increase of the abundance of the N-terminal MYRF cleavage product, this increase in protein levels seems to have engaged a compensatory mechanism resulting in a

decrease in *Myrf* transcript levels, presumably in an attempt to return MYRF to normal levels. Our MS data from *Fbxw7* knock-down cells showed that ZFP24[271] was significantly down regulated compared to controls, presenting a possible link to the change in *Myrf* transcription[271], and highlights an exciting and unexplored mechanism that OLs use to regulate *Myrf* mRNA levels to control myelination. Additionally, while we showed *Myrf* mRNA was significantly down regulated in both the ON and cerebellum at later timepoints, it's interesting to note that this transcriptional downregulation was only sufficient to reduce nuclear MYRF proteins levels in the ON but not the cerebellum. This raises an intriguing question: does the underlying physiology of the myelinated circuit affect OLs requirement and expression of MYRF? While we have shown that FBXW7 binds N-MYRF to control its levels both *in vitro* and *in vivo*, this does not preclude the possibility that additional mechanisms are involved in MYRF protein stability, cleavage, and function.

The full length MYRF protein trimerizes and self-cleaves to enable release of the active transcription factor[164,166,168]. Although this process is negatively regulated by TMEM98, the protein product of one of MYRF's own target genes[165,168], the degree to which TMEM98 negatively regulates the production of the N-MYRF transcription factor at endogenous levels remains unclear. FBXW7 negatively regulates N-MYRF levels in primary OLs, corroborating the finding that FBXW7 targets N-MYRF in mHepa cells[229] and suggesting a conserved regulatory mechanism. Indeed, the fact that myelin and OL abnormalities could be suppressed in *Plp1-Cre^{ERT}- Fbxw7$^{fl/fl}$* mice and *fbxw7^{vo86}* fish by *Myrf*

haploinsufficiency highlights N-MYRF as a central FBXW7 target within the OL lineage. In contrast to mHepa cells, however, in primary OLs, the FBXW7 interaction does not seem to depend on the phosphorylation of the phosphodegron motif by GSK3β or CDK5. The intracellular pathways and mediating kinases that initiate N-MYRF turnover by FBXW7 will be important to determine in future work.

Notably, the dysregulated proteins seen in *Fbxw7* knockdown OLs included many cell adhesion and cell surface proteins. Previous research has highlighted the connection between adhesion molecules and proper myelination. For instance, when contactin-associated protein (*Caspr*), contactin-1 (*Cntn1*), neurofascin (*Nfasc155*), and myelin-associated glycoprotein (*Mag*) were globally deleted in both the zebrafish and mouse CNS, overlapping myelin phenotypes were observed as in *Plp1-Cre^{ERT}-Fbxw7$^{fl/fl}$* animals[273]. Specifically, loss of these adhesion proteins resulted in outfolds, double myelinated axons, and disorganized paranodal loops as well as neuronal cell body ensheathment in the zebrafish spinal cord. It is exciting that within our model, where *Fbxw7* deletion is restricted to myelinating OLs, we see such similar phenotypes when compared to global disruption of adhesion proteins in the CNS.

In summary, we have shown that FBXW7 is an evolutionary conserved regulator of OL myelin capacity and homeostasis. We found that FBXW7 regulates myelination by controlling sheath elongation independent of myelin wraps and is required for long-term maintenance of myelin integrity and paranodal organization within the adult CNS, in part, through its negative regulation of N-MYRF.

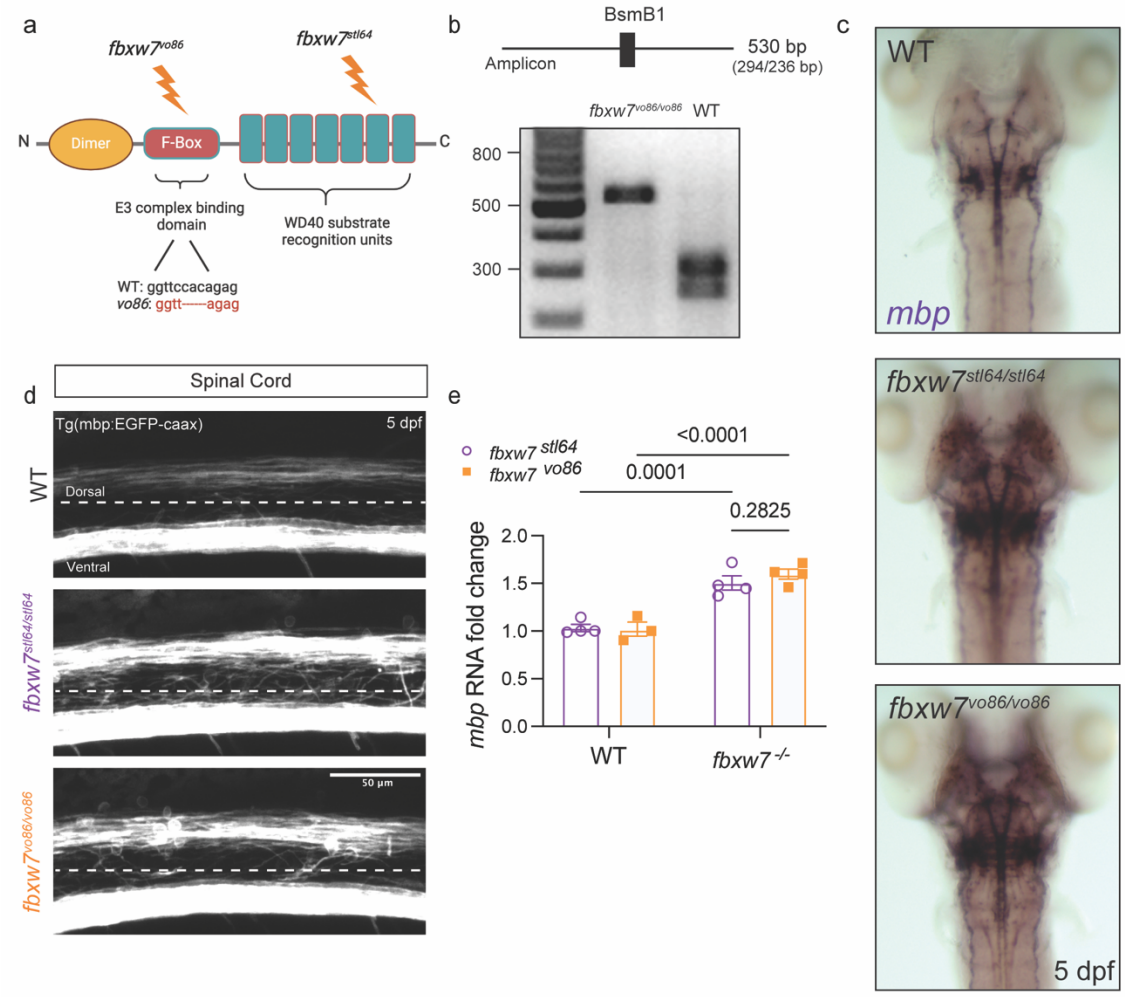
a
fbxw7vo86
fbxw7stl64
N
Dimer
F-Box
C
E3 complex binding domain
WD40 substrate recognition units
WT: ggttccacagag
vo86: ggtt-----agag
b
BsmB1
Amplicon
530 bp
(294/236 bp)
fbxw7vo86/vo86
WT
800
500
300
c
WT
mbp
fbxw7stl64/stl64
fbxw7vo86/vo86
5 dpf
d
Spinal Cord
Tg(mbp:EGFP-caax)
5 dpf
WT
Dorsal
Ventral
fbxw7stl64/stl64
fbxw7vo86/vo86
50 µm
e
fbxw7 stl64
fbxw7 vo86
<0.0001
0.0001
0.2825
mbp RNA fold change
2.0
1.5
1.0
0.5
0.0
WT
fbxw7 -/-

Figure 3.1 Creation and validation of fbxw7^{vo86} zebrafish mutant allele

a Diagram of FBXW7 functional domains showing the locations of the previous ENU-induced mutation (*fbxw7*^{stl64})[26] and the new CRISPR-Cas9 generated mutation (*fbxw7*^{vo86}). **b** Diagram of BsmB1 restriction enzyme digestion of a 560 bp amplicon of *fbxw7*^{vo86} allele to generate a 294 and 236 bp band. Example of *fbxw7*^{vo86} 560 bp genotyping PCR digested with BsmB1 restriction enzyme run on a 2% gel for WT and *fbxw7*$^{vo86/vo86}$ zebrafish larvae. **c** Representative images of *in situ* hybridization for *mbp* in 5 dpf WT, *fbxw7*$^{stl64/stl64}$, and *fbxw7*$^{vo86/vo86}$ zebrafish larvae. **d** Representative images of the spinal cord from *fbxw7*$^{stl64/stl64}$ and *fbxw7*$^{vo86/vo86}$ Tg(mbp:EGFP-caax) zebrafish lines showing an increase in *mbp:EGFP-caax* intensity in both mutant alleles compared to WT control. **e** qRT-PCR for *mbp* from *fbxw7*$^{stl64/stl64}$ and *fbxw7*$^{vo86/vo86}$ whole zebrafish larvae relative to WT controls. Average ± SEM, WT controls N = 3, *fbxw7*$^{-/-}$ N=4, biological replicates (larvae). Statistical significance determined by two-way ANOVA. Created in BioRender.

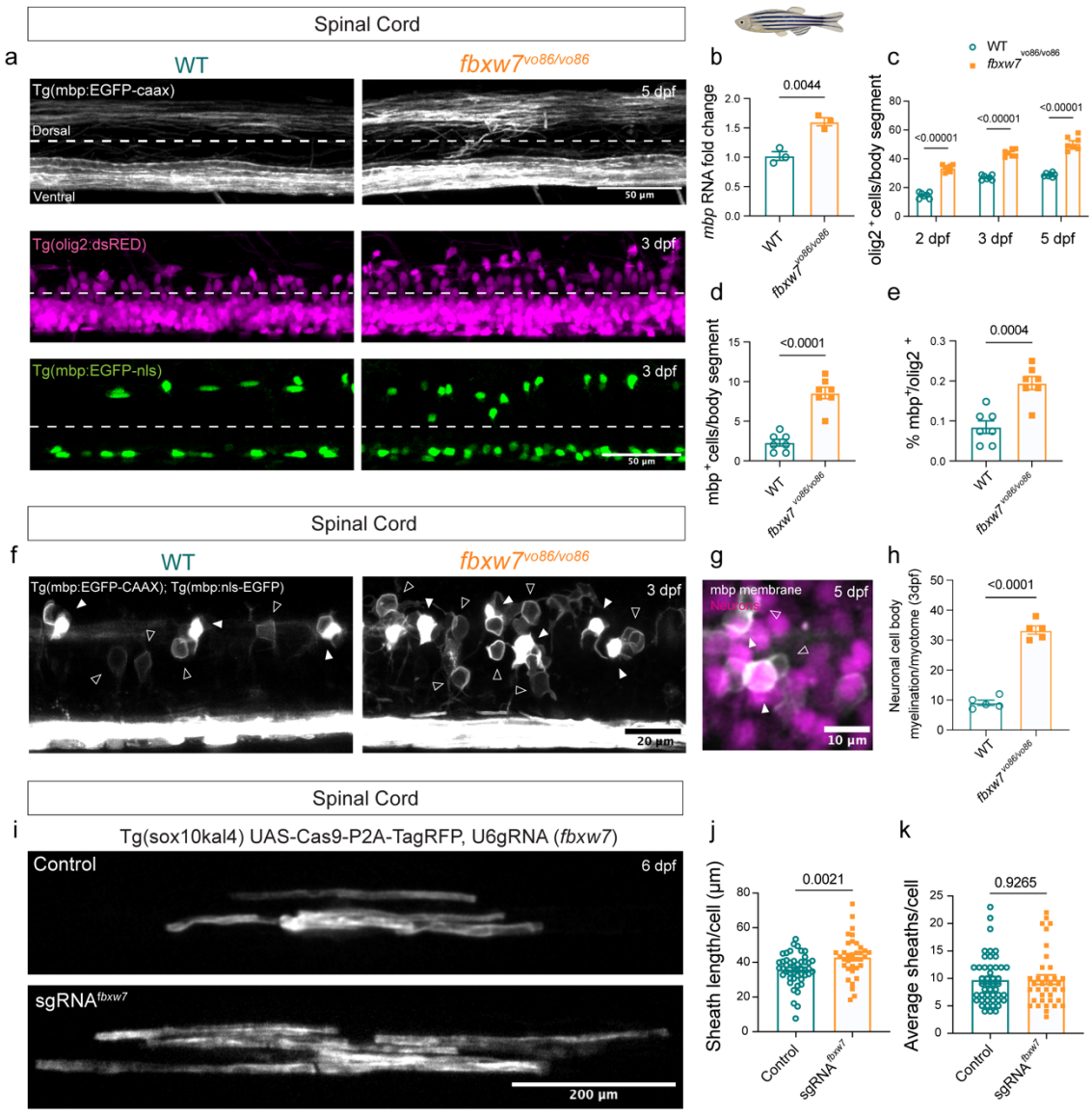
Spinal Cord
a
WT
fbxw7vo86/vo86
Tg(mbp:EGFP-caax)
Dorsal
Ventral
5 dpf
50 µm
Tg(olig2:dsRED)
3 dpf
Tg(mbp:EGFP-nls)
3 dpf
50 µm
b
0.0044
mbp RNA fold change
WT
fbxw7vo86/vo86
c
WT
fbxw7vo86/vo86
olig2+ cells/body segment
<0.00001
<0.00001
<0.00001
2 dpf
3 dpf
5 dpf
d
<0.0001
mbp+ cells/body segment
WT
fbxw7vo86/vo86
e
0.0004
% mbp+/olig2+
WT
fbxw7vo86/vo86
Spinal Cord
f
WT
fbxw7vo86/vo86
Tg(mbp:EGFP-CAAX); Tg(mbp:nls-EGFP)
3 dpf
20 µm
g
mbp membrane
Neurons
5 dpf
10 µm
h
<0.0001
Neuronal cell body
myelination/myotome (3dpf)
WT
fbxw7vo86/vo86
Spinal Cord
i
Tg(sox10kal4) UAS-Cas9-P2A-TagRFP, U6gRNA (fbxw7)
Control
6 dpf
sgRNAfbxw7
200 µm
j
0.0021
Sheath length/cell (µm)
Control
sgRNAfbxw7
k
0.9265
Average sheaths/cell
Control
sgRNAfbxw7

Figure 3.2 fbxw7 regulates OPC specification and OL myelination in the zebrafish spinal cord

a Spinal cords of *fbxw7*^{vo86} and WT controls in (top) *Tg(mbp:eGFP-caax)*, (middle) *Tg*(*olig2:dsRED*$^{+}$*),* and (bottom) *Tg(mbp:nls-eGFP)* transgenic backgrounds at 3 and 5 days post-fertilization (dpf; dotted-line delineates dorsal and ventral spinal cord tracts). **b** *mbp* RNA levels evaluated by qRT-PCR in 5 dpf *fbxw7*^{vo86} and WT control whole larvae. Average ± SEM, N = 3 (larvae). Statistical significance determined by unpaired, two-tailed Student's t test. **c** Quantification of *olig2:dsRED*$^{+}$ cells/body segment in the dorsal spinal cord at 2, 3, and 5 dpf. Average ± SEM, N = 7 (larvae). Statistical significance determined by two-way ANOVA. **d** Quantification of *mbp:nls-eGFP*$^{+}$ OLs in the dorsal spinal cord/body segment at 3 dpf. Average ± SEM, N = 7 (larvae). Statistical significance determined by unpaired, two-tailed Student's t test. **e** *mbp-nls:eGFP*$^{+}$ OLs divided by the average number of *olig2:dsRED*$^{+}$ cells/body segments in dorsal spinal cord at 3 dpf. Average ± SEM, statistical significance determined by unpaired, two-tailed Student's t test. **f** Spinal cords of *fbxw7*^{vo86} and WT control zebrafish in *Tg(mbp:eGFP-caax)* and *Tg(mbp:nls-eGFP)* transgenic backgrounds live-imaged at 3 dpf. Solid arrowheads denote OL somas, hollow arrowheads denote neuronal cell body wrapping. **g** Representative image of an *fbxw7*^{vo86} embryo in *Tg(mbp:eGFP-caax)* (white) and *Tg(nbt:dsRED)* (magenta) backgrounds showing neuronal cell bodies in the spinal cord wrapped in *mbp*$^{+}$ membrane. **h** Quantification of wrapped neuronal cell bodies in the spinal cord in both *fbxw7*^{vo86} and WT controls at 3 dpf. Average ± SEM, N = 5 (larvae). Statistical significance

determined by unpaired, two-tailed Student's t test. **i** Representative images of individual labelled OLs from cell-type specific CRISPR-Cas9 knock-down of *fbxw7* in *sox10* expressing cells in the zebrafish spinal cord at 6 dpf. The UAS-nlscas9-P2A-TagRFPT-caax construct allows visualization of Cas9-expressing cells. **j** Quantification of average sheath length and **k** number per OL in controls and with *fbxw7* knockdown. Average ± SEM, Control N = 47 (cells from 40 animals), sgRNA^{fbxw7} N=36 (cells from 29 animals). Statistical significance determined by unpaired, two-tailed Student's t test. Created in BioRender.

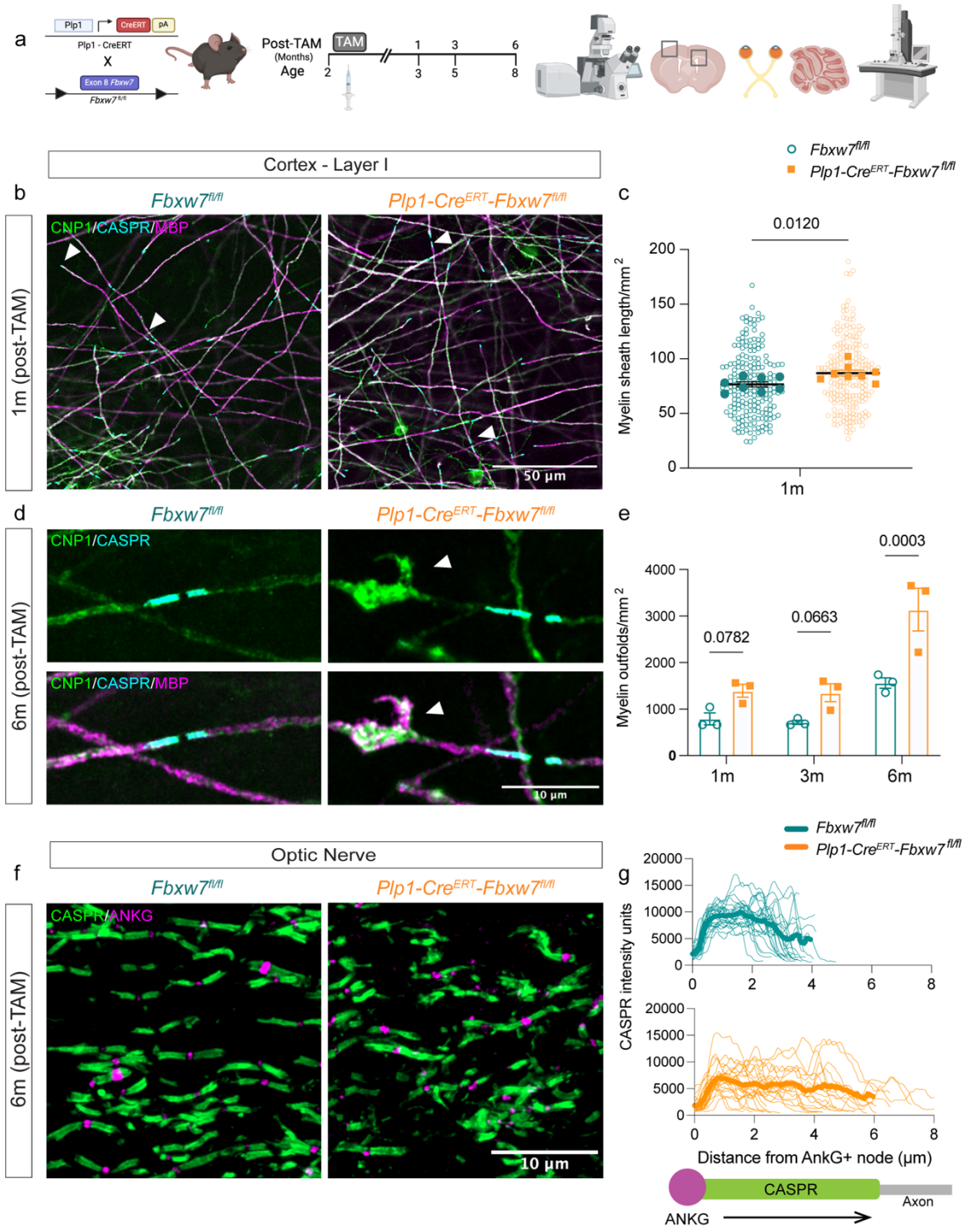
a
Plp1
CreERT
pA
Plp1 - CreERT
X
Exon 8 Fbxw7
Fbxw7 fl/fl
Post-TAM
(Months)
Age
TAM
2
1
3
5
6
8
Cortex - Layer I
Fbxw7fl/fl
Plp1-CreERT-Fbxw7fl/fl
b
1m (post-TAM)
CNP1/CASPR/MBP
50 µm
c
0.0120
Myelin sheath length/mm2
200
150
100
50
0
1m
d
6m (post-TAM)
CNP1/CASPR
CNP1/CASPR/MBP
10 µm
e
0.0003
0.0663
0.0782
Myelin outfolds/mm2
4000
3000
2000
1000
0
1m
3m
6m
Optic Nerve
f
6m (post-TAM)
CASPR/ANKG
10 µm
g
CASPR intensity units
20000
15000
10000
5000
0
2
4
6
8
Distance from AnkG+ node (µm)
CASPR
Axon
ANKG

Figure 3.3 Fbxw7 regulates OL internode length, myelin homeostasis, and paranode organization in mouse grey and white matter

a Schematic of *Fbxw7*$^{fl/fl}$ and *Plp1-Cre*^{ERT}*-Fbxw7*$^{fl/fl}$ mouse line and experimental pipeline. **b** Representative images of myelin internodes in *Fbxw7*$^{fl/fl}$ and *Plp1-Cre*^{ERT}*-Fbxw7*$^{fl/fl}$ 1-month post-tamoxifen (TAM) in mouse layer I of the primary somatosensory cortex (pSS), stained with MBP (magenta), CNP1 (green), and CASPR (cyan). Arrowheads show CASPR^{+} boundaries of internodes. **c** Quantification of sheath length from layer I pSS. Colored bolded dots represent average of ROI from individual biological replicates *Fbxw7*$^{fl/fl}$ N=4, *Plp1-Cre*^{ERT}*-Fbxw7*$^{fl/fl}$ N=4 (mice), small hollow dots represent values from individual sheaths (*Fbxw7*$^{fl/fl}$ N=197, *Plp1-Cre*^{ERT}*-Fbxw7*$^{fl/fl}$ N=210). Statistical significance determined by unpaired, two-tailed Student's t-test on ROI averages. **d** Higher magnification images of myelin outfolds (arrowheads) in pSS cortex 6 months post-TAM. **e** Quantification of myelin outfolds in the pSS. Biological replicates as per b and c. **f** Representative images of CASPR and ANKG stained longitudinal optic nerve sections from *Fbxw7*$^{fl/fl}$ and *Plp1-Cre*^{ERT}*-Fbxw7*$^{fl/fl}$ mice at 6-months post-TAM. **g** Quantification of CASPR straining intensity as a function of distance from ANKG^{+} node. Thick lines represent mean for the genotype, thin lines represent individual heminode intensity histograms. *Fbxw7*$^{fl/fl}$ N=4 (total nodes= 27), *Plp1-Cre*^{ERT}*-Fbxw7*$^{fl/fl}$ N=4 (total nodes=32) from 3 technical replicates. Created in BioRender.

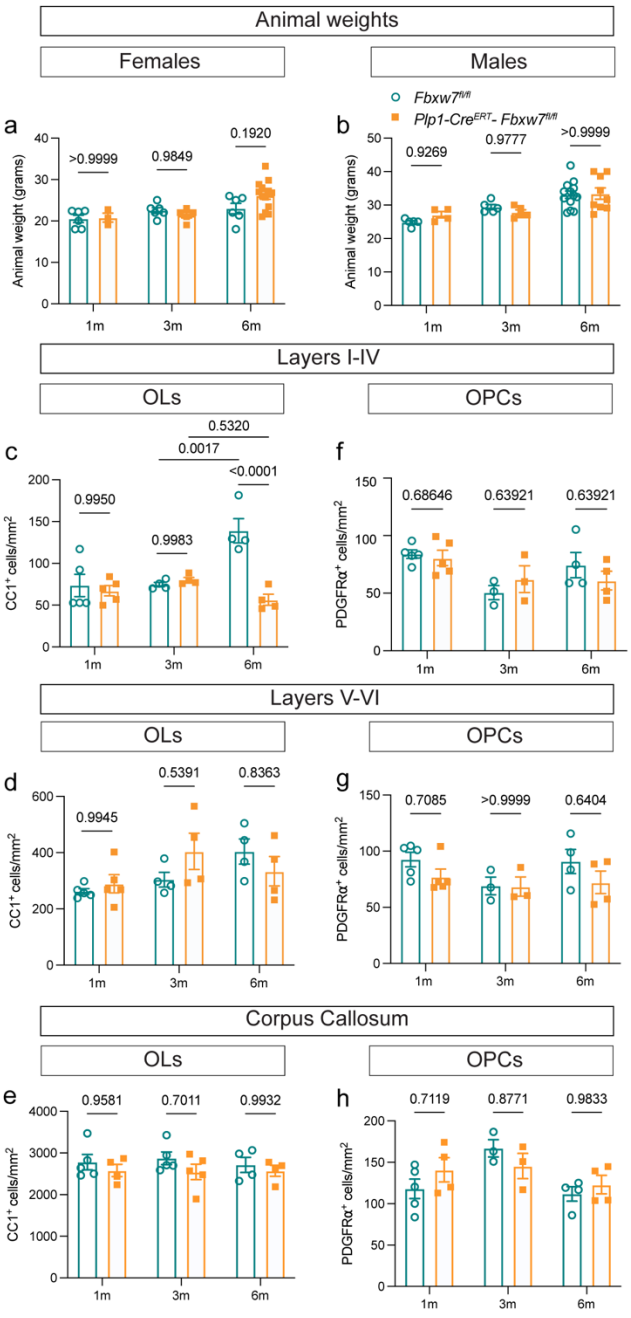
Animal weights
Females
Males
a
b
Fbxw7fl/fl
Plp1-CreERT- Fbxw7fl/fl
Animal weight (grams)
>0.9999
0.9849
0.1920
0.9269
0.9777
>0.9999
1m
3m
6m
Layers I-IV
OLs
OPCs
c
f
0.5320
0.0017
<0.0001
0.9950
0.9983
CC1+ cells/mm2
PDGFRα+ cells/mm2
0.68646
0.63921
0.63921
Layers V-VI
OLs
OPCs
d
g
0.9945
0.5391
0.8363
0.7085
>0.9999
0.6404
Corpus Callosum
OLs
OPCs
e
h
0.9581
0.7011
0.9932
0.7119
0.8771
0.9833

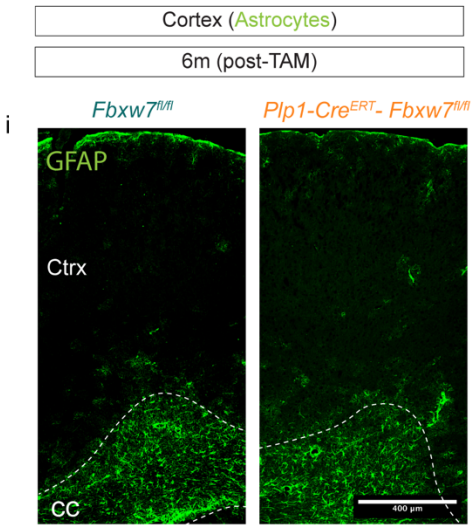
Cortex (Astrocytes)
6m (post-TAM)
i
Fbxw7fl/fl
Plp1-CreERT- Fbxw7fl/fl
GFAP
Ctrx
CC
400 µm

Figure 3.4 Plp1-CreERT-Fbxw7$^{fl/fl}$ mouse line characterization

a Animal weights for males and **b** females in *Fbxw7$^{fl/fl}$* and *Plp1-Cre^{ERT}-Fbxw7$^{fl/fl}$* mice at 1-, 3-, and 6-months post-TAM. **c** Quantification of OL number in cortical layers 1-4, **d** layers 5-6, **e** corpus callosum. Quantification of OPC number in **f** cortical layers 1-4, **g** layers 5-6, and **h** corpus callosum. 1-month (*Fbxw7$^{fl/fl}$* N= 4-5, *Plp1-Cre^{ERT}-Fbxw7$^{fl/fl}$* N= 4-5), 3-months (*Fbxw7$^{fl/fl}$* N= 3-4, *Plp1-Cre^{ERT}-Fbxw7$^{fl/fl}$* N= 3-4), and 6-months post-TAM (*Fbxw7$^{fl/fl}$* N=4, *Plp1-Cre^{ERT}-Fbxw7$^{fl/fl}$* N=4). Average ± SEM, statistical significance determined by two-way ANOVA. **i** Representative images of cortical GFAP IF at 6-months post-TAM in *Fbxw7$^{fl/fl}$* and *Plp1-Cre^{ERT}-Fbxw7$^{fl/fl}$*. White dotted line delineates the border between the corpus callosum (CC) and cortex.

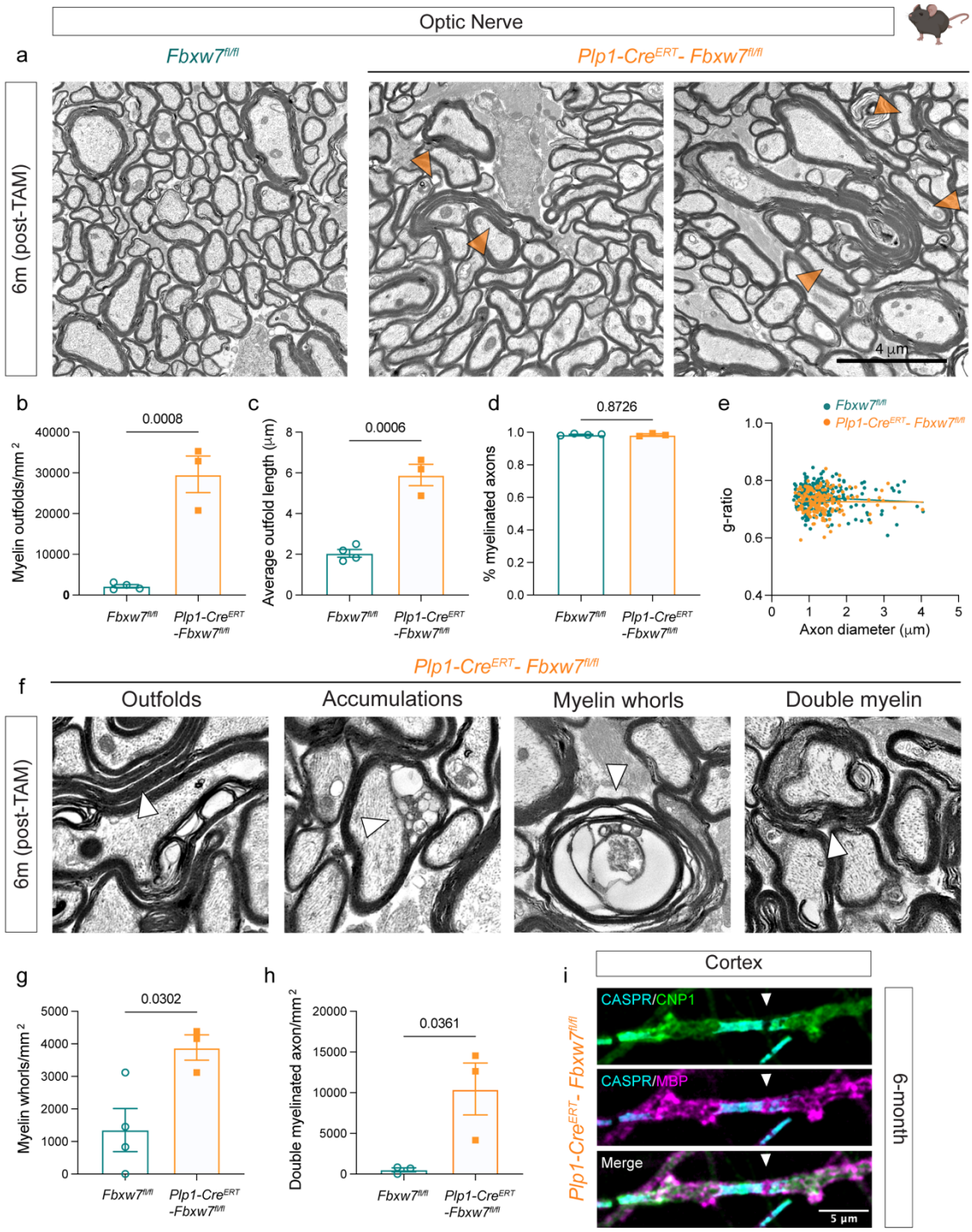
Optic Nerve
a
Fbxw7fl/fl
Plp1-CreERT- Fbxw7fl/fl
6m (post-TAM)
4 µm
b
0.0008
Myelin outfolds/mm 2
Fbxw7fl/fl
Plp1-CreERT -Fbxw7fl/fl
c
0.0006
Average outfold length (µm)
d
0.8726
% myelinated axons
e
Fbxw7fl/fl
Plp1-CreERT- Fbxw7fl/fl
g-ratio
Axon diameter (µm)
f
Outfolds
Accumulations
Myelin whorls
Double myelin
g
0.0302
Myelin whorls/mm 2
h
0.0361
Double myelinated axon/mm 2
i
Cortex
CASPR/CNP1
CASPR/MBP
Merge
5 µm
6-month

Figure 3.5 Loss of Fbxw7 in OLs results in severe myelin outfolds in the optic nerve

a Representative image from transmission electron microscopy (TEM) micrographs of optic nerves from *Fbxw7*$^{fl/fl}$ and *Plp1-Cre*^{ERT}*-Fbxw7*$^{fl/fl}$ mice at 6-months post-TAM. Outfolds highlighted by arrow. **b-e** Quantification of number of outfolds (**b)**, severity of outfolds (**c**), number of myelinated axons (**d**), and g-ratios (**e**). **f** Representative images of different myelin abnormalities in *Plp1-Cre*^{ERT}*-Fbxw7*$^{fl/fl}$ optic nerves at 6-months post-TAM. **g-h** Quantification of OL myelin whorls and double myelin. All data displayed as average ± SEM. *Fbxw7*$^{fl/fl}$ (N=4), *Plp1-Cre*^{ERT}*-Fbxw7*$^{fl/fl}$ (N=3). Statistical significance determined by unpaired, two-tailed Student's t test on animal averages. **i** Example image from pSS cortex of a Caspr^{+}, CNP1^{+} paranode under MBP^{+} myelin sheath. Created in BioRender.

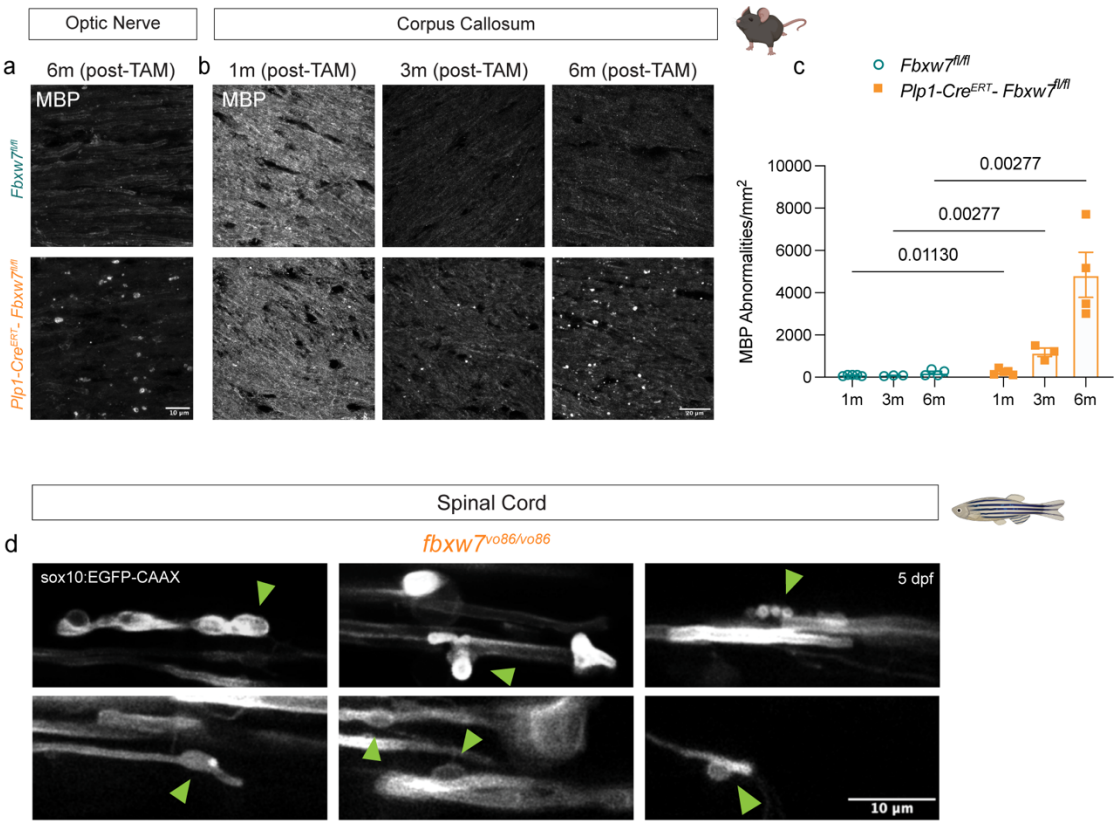
Optic Nerve
Corpus Callosum
a
6m (post-TAM)
b
1m (post-TAM)
3m (post-TAM)
6m (post-TAM)
MBP
MBP
Fbxw7fl/fl
Plp1-CreERT- Fbxw7fl/fl
c
Fbxw7fl/fl
Plp1-CreERT- Fbxw7fl/fl
MBP Abnormalities/mm2
10000
8000
6000
4000
2000
0
0.00277
0.00277
0.01130
1m
3m
6m
1m
3m
6m
Spinal Cord
d
fbxw7vo86/vo86
sox10:EGFP-CAAX
5 dpf
10 µm

Figure 3.6 Deletion of Fbxw7 results in myelin abnormalities in both zebrafish and mouse models

a Representative images of MBP IF at 6-months post-TAM in the optic nerve. **b** Representative images of MBP IF at 1-, 3-, and 6-months post-TAM in the corpus callosum. **c** Quantification of the density of MBP outfolds in the corpus callosum at 1-month (*Fbxw7*$^{fl/fl}$ N=4, *Plp1-Cre*^{ERT}*-Fbxw7*$^{fl/fl}$ N=4), 3-months (*Fbxw7*$^{fl/fl}$ N=3, *Plp1-Cre*^{ERT}*-Fbxw7*$^{fl/fl}$ N=3), and 6-months post-TAM (*Fbxw7*$^{fl/fl}$ N=4, *Plp1-Cre*^{ERT}*-Fbxw7*$^{fl/fl}$ N=4). Average ± SEM, statistical significance determined by two-way ANOVA. **d** Representative *fbxw7*$^{vo86/vo86}$ mutant embryo injected with a plasmid driving EGFP under the *sox10* promoter at the single-cell stage showing membrane blebbing and outfolds by individual EGFP^{+} OLs at 5 dpf.

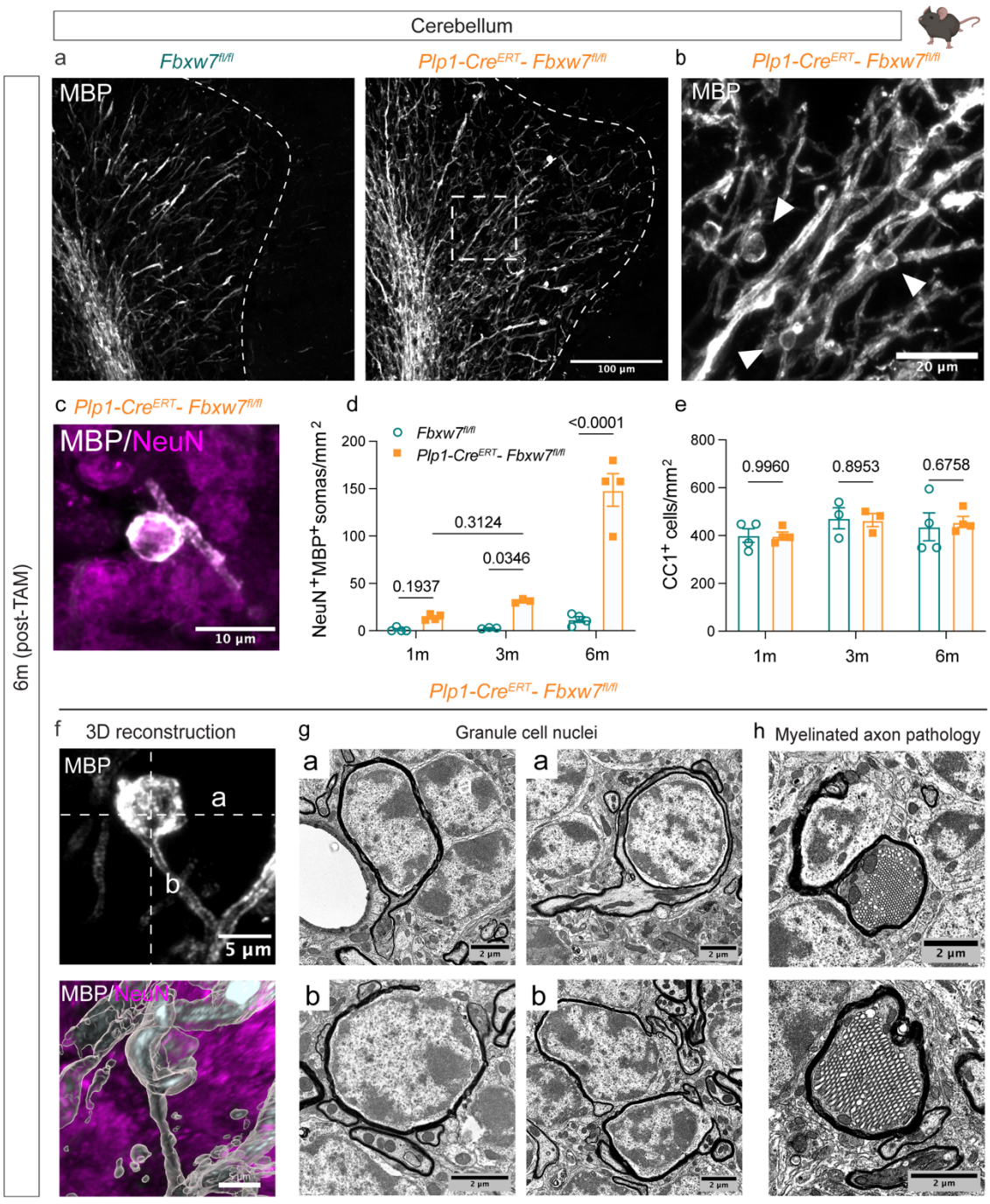
Cerebellum
6m (post-TAM)
a
Fbxw7fl/fl
Plp1-CreERT- Fbxw7fl/fl
b
Plp1-CreERT- Fbxw7fl/fl
MBP
MBP
100 µm
20 µm
c Plp1-CreERT- Fbxw7fl/fl
MBP/NeuN
10 µm
d
Fbxw7fl/fl
Plp1-CreERT- Fbxw7fl/fl
NeuN+MBP+somas/mm2
<0.0001
0.3124
0.0346
0.1937
1m
3m
6m
e
CC1+ cells/mm2
0.9960
0.8953
0.6758
1m
3m
6m
Plp1-CreERT- Fbxw7fl/fl
f
3D reconstruction
MBP
a
b
5 µm
MBP/NeuN
g
Granule cell nuclei
a
a
b
b
2 µm
h
Myelinated axon pathology
2 µm

Figure 3.7 Loss of Fbxw7 results in ectopic ensheathment of neuronal cell bodies in the cerebellum.

a Representative images of anti-MBP stained cerebellums from *Fbxw7$^{fl/fl}$* and *Plp1-Cre^{ERT}-Fbxw7$^{fl/fl}$* animals at 6-months post-TAM. Dotted line denotes boarder of the granular and molecular layers. **b** Higher magnification image of MBP staining in the nuclear layer of a *Plp1-Cre^{ERT}-Fbxw7$^{fl/fl}$* animal showing cupped myelin structures, which surround NeuN+ nuclei (shown at higher magnification in **c**). **d** Quantification of NeuN^{+} cells wrapped in MBP positive membrane in the granule cell layer of the cerebellum of *Fbxw7$^{fl/fl}$* and *Plp1-Cre^{ERT}-Fbxw7$^{fl/fl}$* mice at 1-, 3-, and 6-months post-TAM. **e** Quantification of CC1^{+} OLs in the white matter and nuclear layer of *Fbxw7$^{fl/fl}$* and *Plp1-Cre^{ERT}-Fbxw7$^{fl/fl}$* mice at 1-, 3-, and 6-months post-TAM. For **d** and **e**, 1m (N=4), 3m (N=3), 6m (N=4). Data shown as average ± SEM. Statistical significance determined by two-way ANOVA. **f** Image of MBP^{+} myelin outfold (white) around a granule cell (magenta) by IF at 6-months post-TAM reconstructed in Imaris. a and b dotted lines represent orientation of EM images in g. **g** Representative images of myelin outfolds around granule cell nuclei in the granule layer of the cerebellum at 6-months post-TAM. **h** Images of severe cellular accumulations in the axons of putative Purkinje cells in *Plp1-Cre^{ERT}-Fbxw7$^{fl/fl}$* mice at 6-months post-TAM. Created in BioRender.

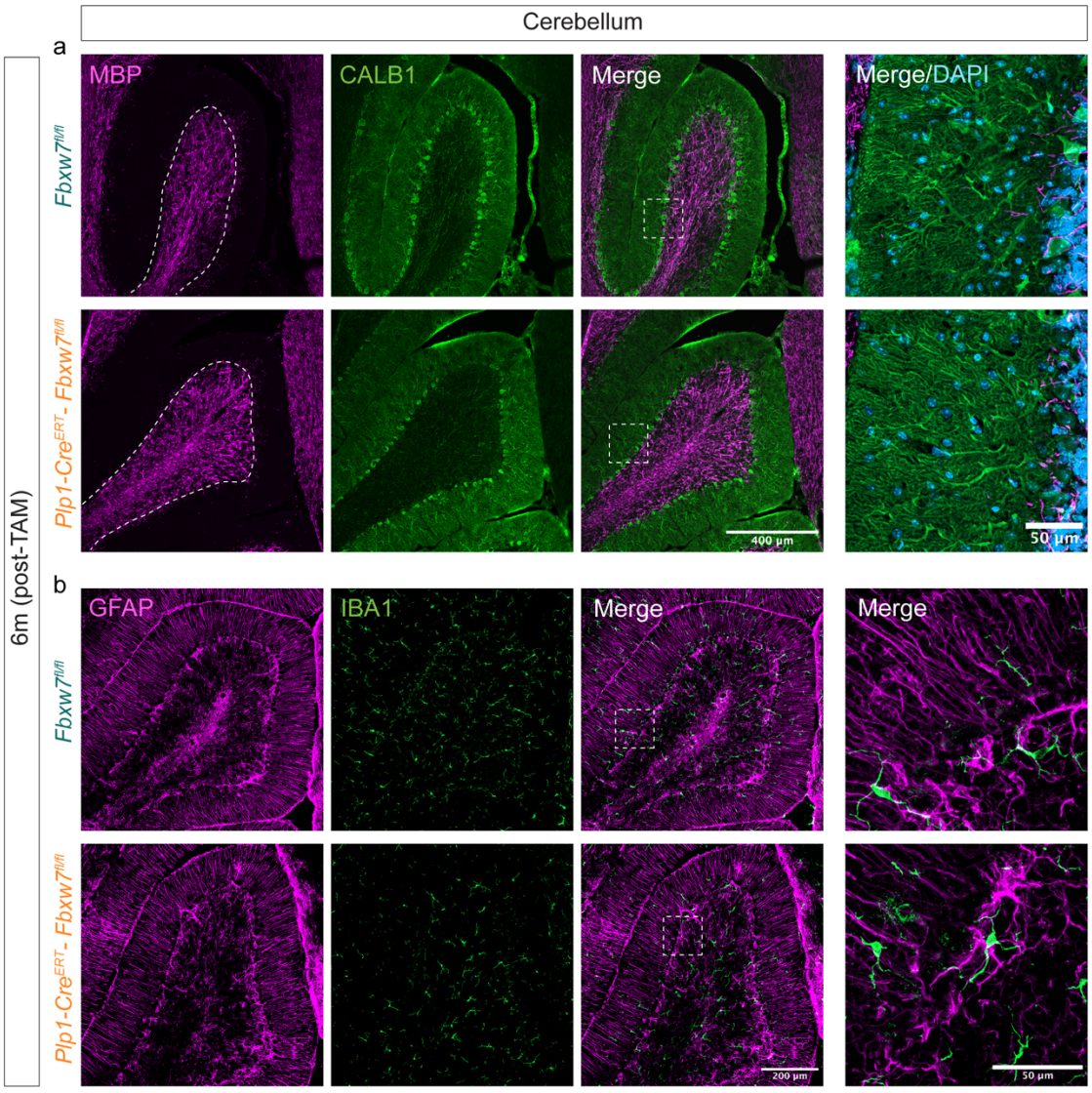
Cerebellum
a
MBP
CALB1
Merge
Merge/DAPI
Fbxw7fl/fl
Plp1-CreERT- Fbxw7fl/fl
400 µm
50 µm
b
GFAP
IBA1
Merge
Merge
Fbxw7fl/fl
Plp1-CreERT- Fbxw7fl/fl
200 µm
50 µm
6m (post-TAM)

Figure 3.8 Plp1-Cre^{ERT}-Fbxw7$^{fl/fl}$ mice have normal appearing cerebellar organization at 6-months post-TAM.

a Representative images of MBP and Calbindin1 (CALB1) IF in the cerebellum of *Fbxw7$^{fl/fl}$* and *Plp1-Cre^{ERT}-Fbxw7$^{fl/fl}$* mice at 6-months post-TAM. High-resolution images of Calbindin1^{+} Purkinje cells show intact morphology in *Plp1-Cre^{ERT}-Fbxw7$^{fl/fl}$* in the molecular layer of the cerebellum 6-months post-TAM. **b** Representative images of GFAP and IBA1 IF in the cerebellum of *Fbxw7$^{fl/fl}$* and *Plp1-Cre^{ERT}-Fbxw7$^{fl/fl}$* mice at 6-months post-TAM.

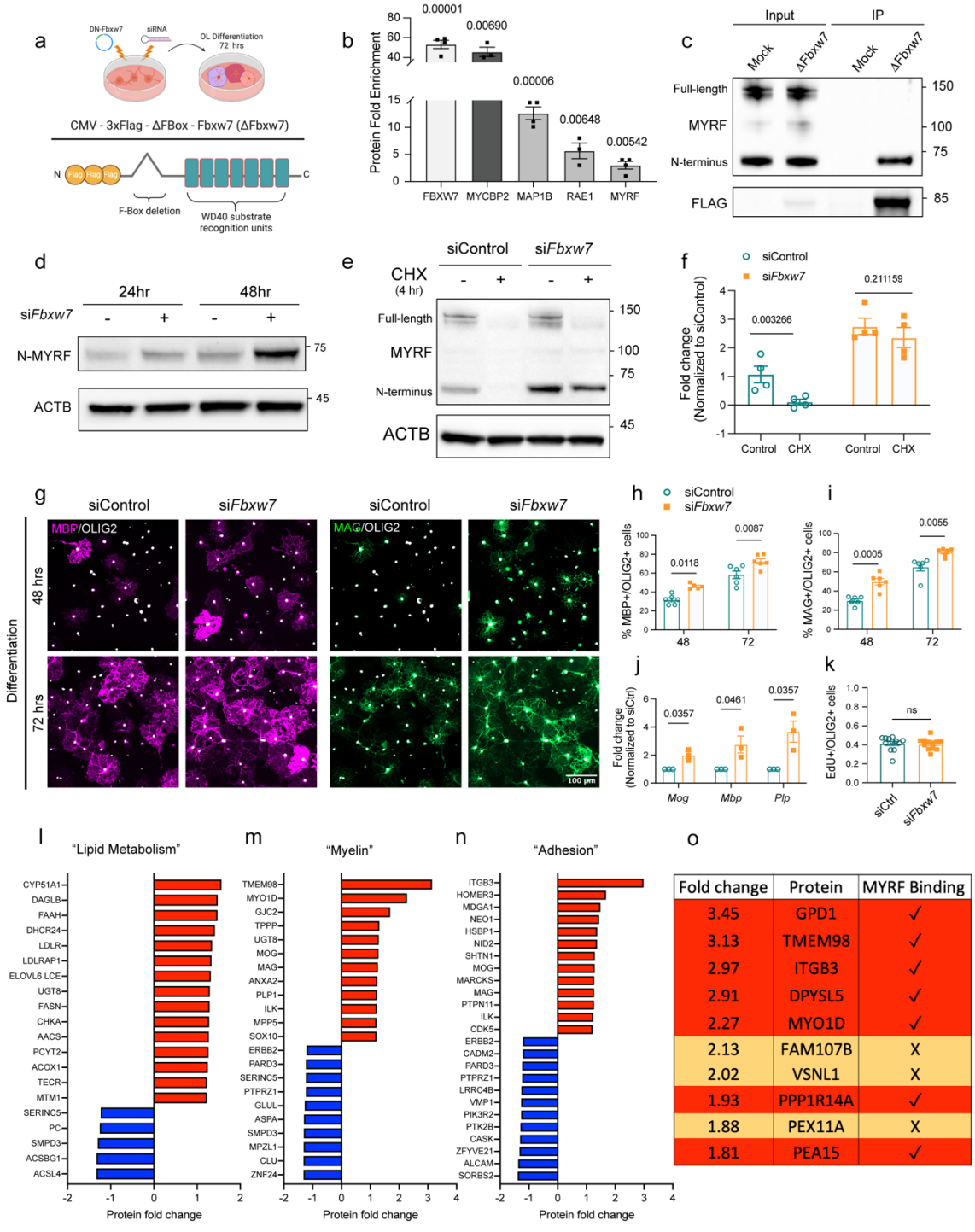

o

Fold change	Protein	MYRF Binding
3.45	GPD1	✓
3.13	TMEM98	✓
2.97	ITGB3	✓
2.91	DPYSL5	✓
2.27	MYO1D	✓
2.13	FAM107B	X
2.02	VSNL1	X
1.93	PPP1R14A	✓
1.88	PEX11A	X
1.81	PEA15	✓

Figure 3.9 FBXW7 binds and degrades the N-terminal MYRF

a Schematic showing workflow of primary rat OPC isolation, expansion, and electroporation with either a dominant-negative FBXW7 construct (CMV-3xFLAG-FBXW7$^{\Delta FBox}$) or pooled siRNAs against *Fbxw7* or non-targeting controls. **b** LC-MS peptide counts for significant proteins enriched by anti-FLAG pull-down in 3xFlag-FBXW7$^{\Delta FBox}$ electroporated cells normalized to GFP electroporated controls. Average ± SEM, (N = 4) (independent cell isolations). Statistical significance determined by multiple unpaired, two-tailed Student's t test. **c** IP-western blot for MYRF following pull down of FBXW7$^{\Delta FBox}$ from cultured rat OLs at 72h differentiation. **d** Western blot analysis of the N-MYRF cleavage product in pooled siRNAs against *Fbxw7* or non-targeting controls at 24 or 48 hr differentiation. **e** Western blot of MYRF in siRNA electroporated OLs treated with cycloheximide (CHX) for 4 hours. Relative intensity of the N-MYRF band quantified in **f**. Average ± SEM, (N = 4) (independent cell isolations). Statistical significance determined by unpaired, two-tailed Student's t test. **g** Representative images of MBP and MAG expression in cultured OLs differentiated for 48 or 72 hours after electroporation with siControl or si*Fbxw7*. **h,i** MBP+ and MAG+ OLs normalized to total OLIG2+ cells. Average ± SEM, (N = 3) (independent cell isolations) with 2 technical replicates (coverslips) per isolation. Statistical significance determined by two-way ANOVA. **j** qRT-PCR for myelin genes on siRNA treated cells. Average ± SEM, (N = 3) (independent cell isolations) with 2 technical replicates (qRT-PCR). Statistical significance determined by multiple unpaired, two-tailed Student's t test. **k** Quantification of EdU incorporation in primary rat OPCs following

siControl or si*Fbxw7* electroporation. Average ± SEM, (N = 3) (independent cell isolations) with 4 technical replicates (coverslips). Statistical significance determined by unpaired, two-tailed Student's t test. **l-n** LC-MS proteins with +/- >1.2 fold change were sorted by gene ontology (GO) terms "lipid metabolism," "myelin," and "adhesion" (N=4) (independent cell isolations) with 2 technical replicates. Table of the top 10 enriched proteins by TMT-LS/MS in si*Fbxw7* electroporated OLs relative to siControl electroporated OLs at 3 days differentiation. Proteins with 1 or more MYRF ChIP-Seq binding domains within 50 KB of the transcription start site of their corresponding gene were identified based on previously published ChIP-Seq data[166]. Created in BioRender.

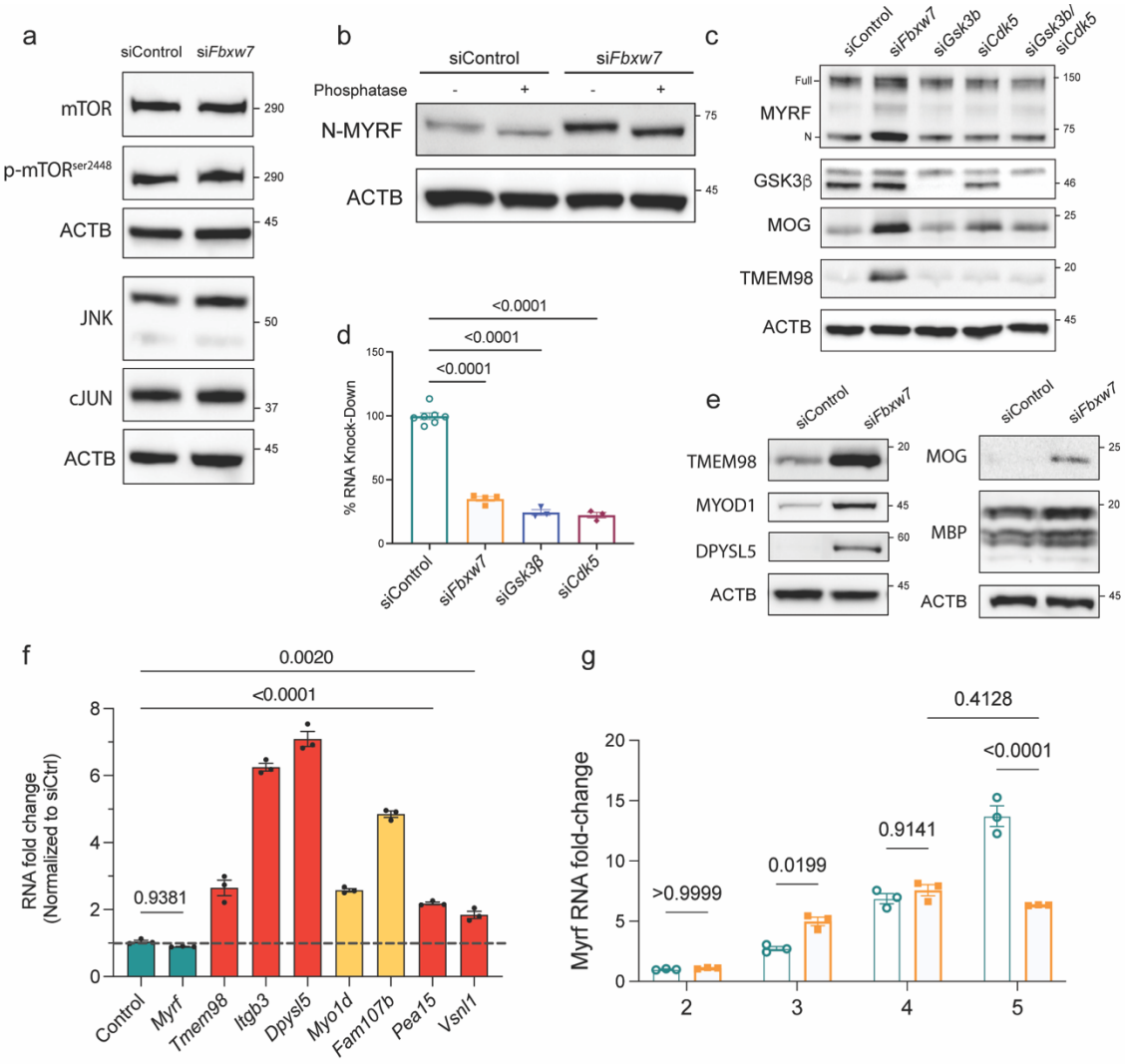
a
siControl
siFbxw7
mTOR
290
p-mTORser2448
290
ACTB
45
JNK
50
cJUN
37
ACTB
45
b
siControl
siFbxw7
Phosphatase
-
+
-
+
N-MYRF
75
ACTB
45
c
siControl
siFbxw7
siGsk3b
siCdk5
siGsk3b/ siCdk5
Full
MYRF
N
150
75
GSK3β
46
MOG
25
TMEM98
20
ACTB
45
d
<0.0001
<0.0001
<0.0001
% RNA Knock-Down
150
100
50
0
siControl
siFbxw7
siGsk3β
siCdk5
e
siControl
siFbxw7
TMEM98
20
MYOD1
45
DPYSL5
60
ACTB
45
siControl
siFbxw7
MOG
25
MBP
20
ACTB
45
f
0.0020
<0.0001
RNA fold change (Normalized to siCtrl)
8
6
4
2
0
0.9381
Control
Myrf
Tmem98
Itgb3
Dpysl5
Myo1d
Fam107b
Pea15
Vsnl1
g
0.4128
<0.0001
0.9141
0.0199
>0.9999
Myrf RNA fold-change
20
15
10
5
0
2
3
4
5

Figure 3.10 Western blot and qRT-PCR assessment of potential FBXW7 targets in OLs

a Western blots for candidate FBXW7 targets mTOR, p-mTOR^{ser2448}, JNK, and cJun in siControl- and si*Fbxw7*-electroporated rat OLs at 72-hours differentiation. **b** Western blot analysis for N-MYRF in siControl- and si*Fbxw7*-electroporated rat OL lysates with lambda phosphatase treatment of the lysates to reveal phosphorylation-dependent changes in molecular weight. **c** Western blot analysis of GSK3β, N-MYRF, TMEM98, and MOG in lysates from siControl-, si*Fbxw7-,* si*Gsk3b-,* si*Cdk5-,* and si*Gsk3b* + si*Cdk5*- electroporated rat OLs at 3 days differentiation. **d** Knock-down efficiency of all siRNA used by qRT-PCR (siControl N=7, si*Fbxw7* N=4, si*Gsk3b* N=3, si*Cdk5* N=3) (independent isolations) with 2 technical replicates. **e** Western blot analysis for top LC-MS hits TMEM98, MYOD1, DPYSL5, as well as myelin proteins MOG and MBP in siControl- and si*Fbxw7*-electroporated rat OLs at 72 hours differentiation. ACTB serves as a loading control for all western blots. **f** qRT-PCR analysis of corresponding transcripts for enriched proteins from si*Fbxw7*-electroporated OLs relative to siControl at 72-hours differentiation (* $p < 0.05$, ** $p < 0.005$). Average ± SEM, (N = 3) (independent isolations) with 2 technical replicates. **g** qRT-PCR of *Myrf* RNA levels in si*Fbxw7* treated cells at 2-6 days in vitro (DIV) relative to siControl. (N=3) (independent isolations) with 2 technical replicates. Statistical significance determined by multiple unpaired, two-tailed Student's t test.

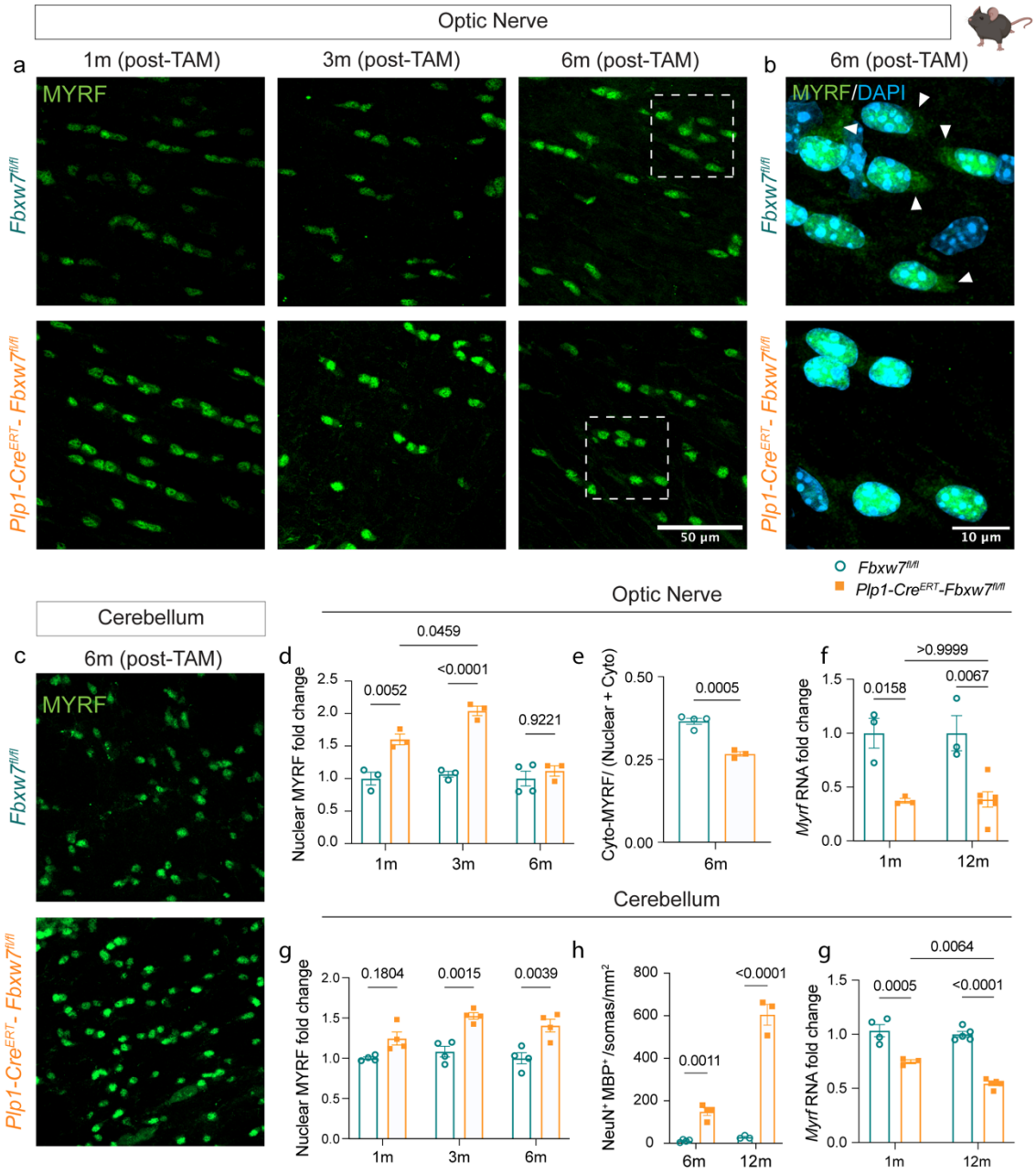
Optic Nerve
a
1m (post-TAM)
3m (post-TAM)
6m (post-TAM)
MYRF
Fbxw7fl/fl
Plp1-CreERT- Fbxw7fl/fl
50 µm
b
6m (post-TAM)
MYRF/DAPI
10 µm
Fbxw7fl/fl
Plp1-CreERT-Fbxw7fl/fl
Cerebellum
c
6m (post-TAM)
MYRF
Optic Nerve
d
Nuclear MYRF fold change
0.0459
0.0052
<0.0001
0.9221
1m
3m
6m
e
Cyto-MYRF/ (Nuclear + Cyto)
0.0005
6m
f
Myrf RNA fold change
>0.9999
0.0158
0.0067
1m
12m
Cerebellum
g
Nuclear MYRF fold change
0.1804
0.0015
0.0039
1m
3m
6m
h
NeuN+ MBP+/somas/mm2
0.0011
<0.0001
6m
12m
g
Myrf RNA fold change
0.0064
0.0005
<0.0001
1m
12m

Figure 3.11 FBXW7 regulates OL MYRF levels in vivo

a Representative images of optic nerves from *Fbxw7*$^{fl/fl}$ and *Plp1-Cre*^{ERT}*-Fbxw7*$^{fl/fl}$ mice at 1-, 3-, and 6-months post-TAM stained for MYRF. **b** High-resolution images showing cytoplasmic localization of MYRF in the optic nerve OLs of 6-months post-TAM animals. Arrowheads indicate cytoplasmic localization of MYRF (likely uncleaved precursor) in the *Fbxw7*$^{fl/fl}$ control. **c** Representative images of cerebellums from *Fbxw7*$^{fl/fl}$ and *Plp1-Cre*^{ERT}*-Fbxw7*$^{fl/fl}$ mice at 6-months post-TAM stained for MYRF. **d** Quantification of nuclear MYRF intensity in *Plp1-Cre*^{ERT}*-Fbxw7*$^{fl/fl}$ optic nerves normalized to controls at 1-, 3-, and 6-months post-TAM. Data shown as average ± SEM. Statistical significance determined by two-way ANOVA. **e** Ratio of cytoplasmic relative to total (cytoplasmic and nuclear) MYRF at 6-months post-TAM. Statistical significance determined by unpaired, two-tailed Student's t test. For both genotypes, 1m (N=4), 3m (N=3), 6m (N=4). **f** qRT-PCR quantification of *Myrf* RNA fold change in the optic nerve from of *Fbxw7*$^{fl/fl}$ and *Plp1-Cre*^{ERT}*-Fbxw7*$^{fl/fl}$ mice at 1- and 12- months post-TAM. **g** Quantification of nuclear MYRF intensity in *Plp1-Cre*^{ERT}*-Fbxw7*$^{fl/fl}$ cerebellums normalized to controls at 1-, 3-, and 6-months post-TAM. For both genotypes, 1m (N=4), 3m (N=4), 6m (N=4). **h** Quantification of NeuN^{+} cells wrapped in MBP positive membrane in the granule cell layer of the cerebellum in 6- and 12-month post-TAMed *Plp1-Cre*^{ERT}*-Fbxw7*$^{fl/fl}$ and control animals. Data shown as average ± SEM. Statistical significance determined by two-way ANOVA. **g** qRT-PCR quantification of *Myrf* RNA fold change in the cerebellum from of *Fbxw7*$^{fl/fl}$ and *Plp1-Cre*^{ERT}*-Fbxw7*$^{fl/fl}$ mice at 1- and 12- months post-TAM. Created in BioRender.

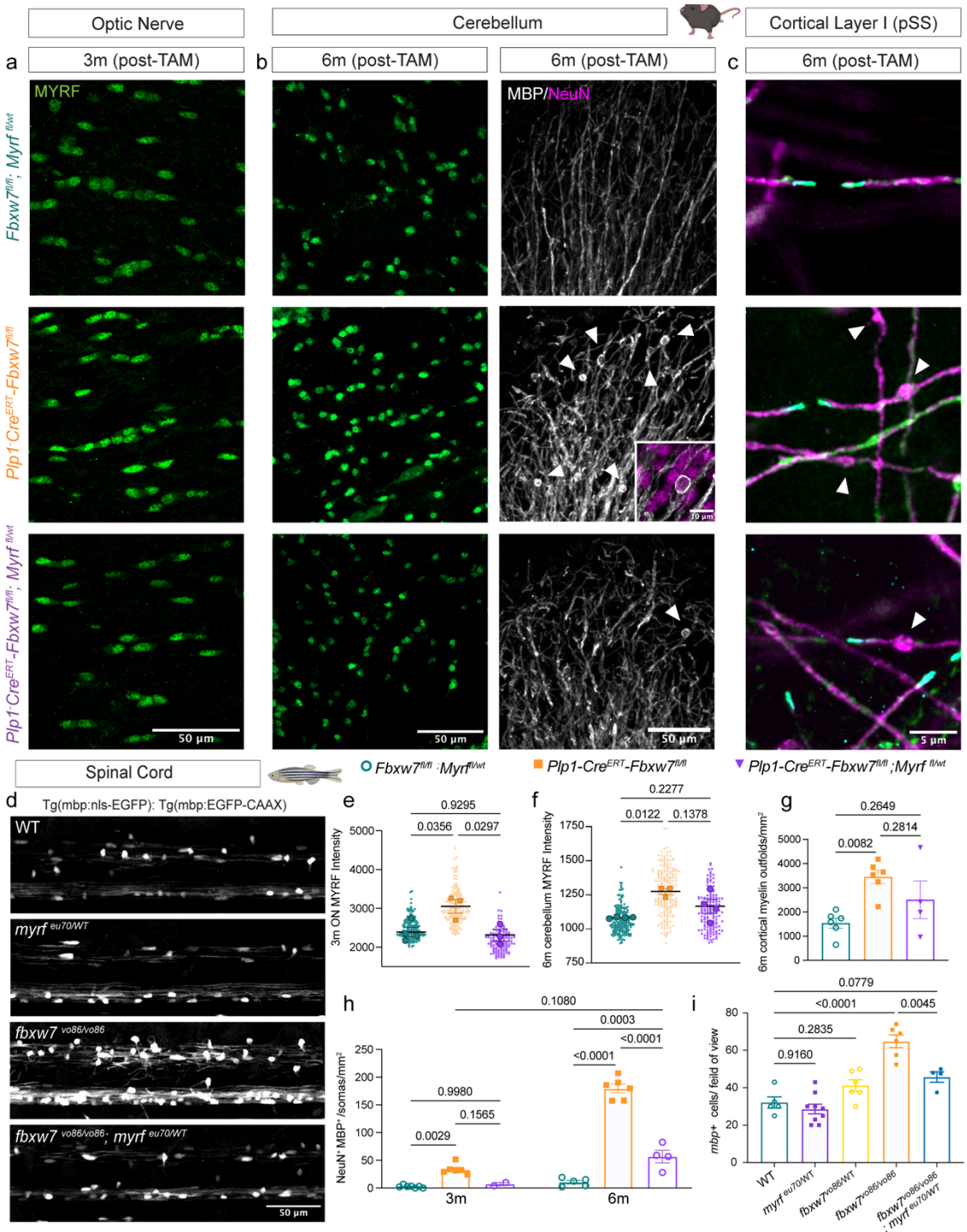
Optic Nerve
Cerebellum
Cortical Layer I (pSS)
a
3m (post-TAM)
b
6m (post-TAM)
6m (post-TAM)
c
6m (post-TAM)
MYRF
MBP/NeuN
Fbxw7fl/fl; Myrffl/wt
Plp1CreERT-Fbxw7fl/fl
Plp1CreERT-Fbxw7fl/fl; Myrffl/wt
50 µm
5 µm
Spinal Cord
Fbxw7fl/fl ;Myrffl/wt
Plp1-CreERT-Fbxw7fl/fl
Plp1-CreERT-Fbxw7fl/fl ;Myrffl/wt
d
Tg(mbp:nls-EGFP): Tg(mbp:EGFP-CAAX)
WT
myrf eu70/WT
fbxw7 vo86/vo86
fbxw7 vo86/vo86; myrf eu70/WT
e
3m ON MYRF Intensity
0.9295
0.0356
0.0297
f
6m cerebellum MYRF Intensity
0.2277
0.0122
0.1378
g
6m cortical myelin outfolds/mm2
0.2649
0.2814
0.0082
h
NeuN+ MBP+/somas/mm2
0.1080
0.0003
<0.0001
<0.0001
0.9980
0.1565
0.0029
3m
6m
i
mbp+ cells/ feild of view
0.0779
<0.0001
0.0045
0.2835
0.9160
WT
myrf eu70/WT
fbxw7vo86/WT
fbxw7vo86/vo86
fbxw7vo86/vo86 ; myrf eu70/WT

Figure 3.12 Myrf haploinsufficiency suppresses myelin phenotypes in Fbxw7 mutant models

a Representative images of optic nerves from *Fbxw7*$^{fl/fl}$, *Plp1-Cre*^{ERT}*-Fbxw7*$^{fl/fl}$, and *Plp1-Cre*^{ERT}*-Fbxw7*$^{fl/f}$*; Myrf* $^{fl/wt}$ mice at 3-months post-TAM stained for MYRF. **b** Representative images of cerebellums from *Fbxw7*$^{fl/fl}$, *Plp1-Cre*^{ERT}*-Fbxw7*$^{fl/fl}$, and *Plp1-Cre*^{ERT}*-Fbxw7*$^{fl/f}$*; Myrf* $^{fl/wt}$ mice at 6-months post-TAM stained for MYRF, MBP, and NeuN. **c** Representative images of myelin internodes layer I of the pSS in *Fbxw7*$^{fl/fl}$, *Plp1-Cre*^{ERT}*-Fbxw7*$^{fl/fl}$, and *Plp1-Cre*^{ERT}*-Fbxw7*$^{fl/f}$*; Myrf* $^{fl/wt}$ mice at 6-months post-TAM stained with MBP (magenta), CNP1 (green), and CASPR (cyan). **d** Representative images of the spinal cords of *fbxw7*$^{vo86/vo86}$ and *fbxw7*$^{vo86/vo86}$*; myrf*$^{eu70/WT}$ zebrafish on Tg(mbp:eGFP-caax) and Tg(mbp:nls-eGFP) transgenic backgrounds at 3 dpf. **e** Quantification of nuclear MYRF intensity in *Fbxw7*$^{fl/fl}$, *Plp1-Cre*^{ERT}*-Fbxw7*$^{fl/fl}$, and *Plp1-Cre*^{ERT}*-Fbxw7*$^{fl/f}$*; Myrf* $^{fl/wt}$ normalized to controls at 3-months post-TAM in the optic nerve (N=4, 3, 3). **f** Quantification of nuclear MYRF intensity in *Fbxw7*$^{fl/fl}$, *Plp1-Cre*^{ERT}*-Fbxw7*$^{fl/fl}$, and *Plp1-Cre*^{ERT}*-Fbxw7*$^{fl/f}$*; Myrf* $^{fl/wt}$ normalized to controls at 6- months post-TAM in the cerebellum (N=4, 3, 4). For both e and f, hollow dots represent individual cell intensities, solid dots represent animal averages ± SEM. Statistical significance determined by one-way ANOVA. **g** Quantification of myelin outfolds in layer I of the pSS in *Fbxw7*$^{fl/fl}$, *Plp1-Cre*^{ERT}*-Fbxw7*$^{fl/fl}$, and *Plp1-Cre*^{ERT}*-Fbxw7*$^{fl/fl}$*; Myrf* $^{fl/wt}$ mice at 6-months post-TAM (N=5, 6, 4). Statistical significance determined by one-way ANOVA. **h** Quantification of NeuN^{+} cells wrapped in MBP^{+} membrane in the granular layer of the cerebellum of *Fbxw7*$^{fl/fl}$ and *Plp1-Cre*^{ERT}*-Fbxw7*$^{fl/fl}$ mice at 3- and 6- months

post-TAM. *Fbxw7*$^{fl/fl}$ (3m: N=7, 6m: N=5), *Plp1-Cre*^{ERT}*-Fbxw7*$^{fl/fl}$ (3m: N=6, 6m: N=6), and *Plp1-Cre*^{ERT}*-Fbxw7*$^{fl/f}$*; Myrf* $^{fl/wt}$ (3m: N=4, 6m: N=4). Data shown as average ± SEM. Statistical significance determined by two-way ANOVA. **i** Quantification of *mbp:nls*$^{+}$ OLs in the zebrafish dorsal spinal cord of each genotype. WT (N=5), *myrf*$^{eu70/wt}$ (N=9), *fbxw7*$^{vo86/WT}$ (N=6), *fbxw7*$^{vo86/vo86}$ (N=6), *fbxw7*$^{vo86/vo86}$*; myrf*$^{eu70/WT}$ (N=4). Average ± SEM, statistical significance determined by two-way ANOVA. Created in BioRender.

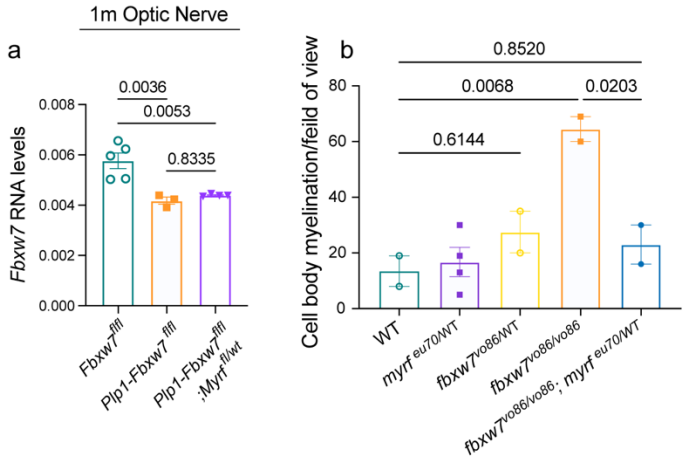
1m Optic Nerve
a
Fbxw7 RNA levels
0.008
0.006
0.004
0.002
0.000
0.0036
0.0053
0.8335
Fbxw7fl/fl
Plp1-Fbxw7fl/fl
Plp1-Fbxw7fl/fl ;Myrfl/wt
b
Cell body myelination/feild of view
80
60
40
20
0
0.8520
0.0068
0.0203
0.6144
WT
myrf eu70/WT
fbxw7vo86/WT
fbxw7vo86/vo86
fbxw7vo86/vo86; myrf eu70/WT

Figure 3.13 Additional characterization of Myrf haploinsufficient Fbxw7 mutant models

a Analyses of *Fbxw7* Cre-recombination efficacy by qRT-PCR for *Fbxw7* from 1-month post-TAM optic nerves. (N=5, 3, 4) (independent isolations, 2 technical replicates). **b** Quantification of cell body ensheathment in the zebrafish dorsal spinal cord of mbp:nls-EGFP and mbp:EGFP-caax for each genotype. WT (N=5), *myrf*$^{eu70/WT}$ (N=9), *fbxw7*$^{vo86/WT}$ (N=6), *fbxw7*$^{vo86/vo86}$ (N=6), *fbxw7*$^{vo86/vo86}$*; myrf*$^{eu70/WT}$ (N=4). Average ± SEM, statistical significance determined by two-way ANOVA.

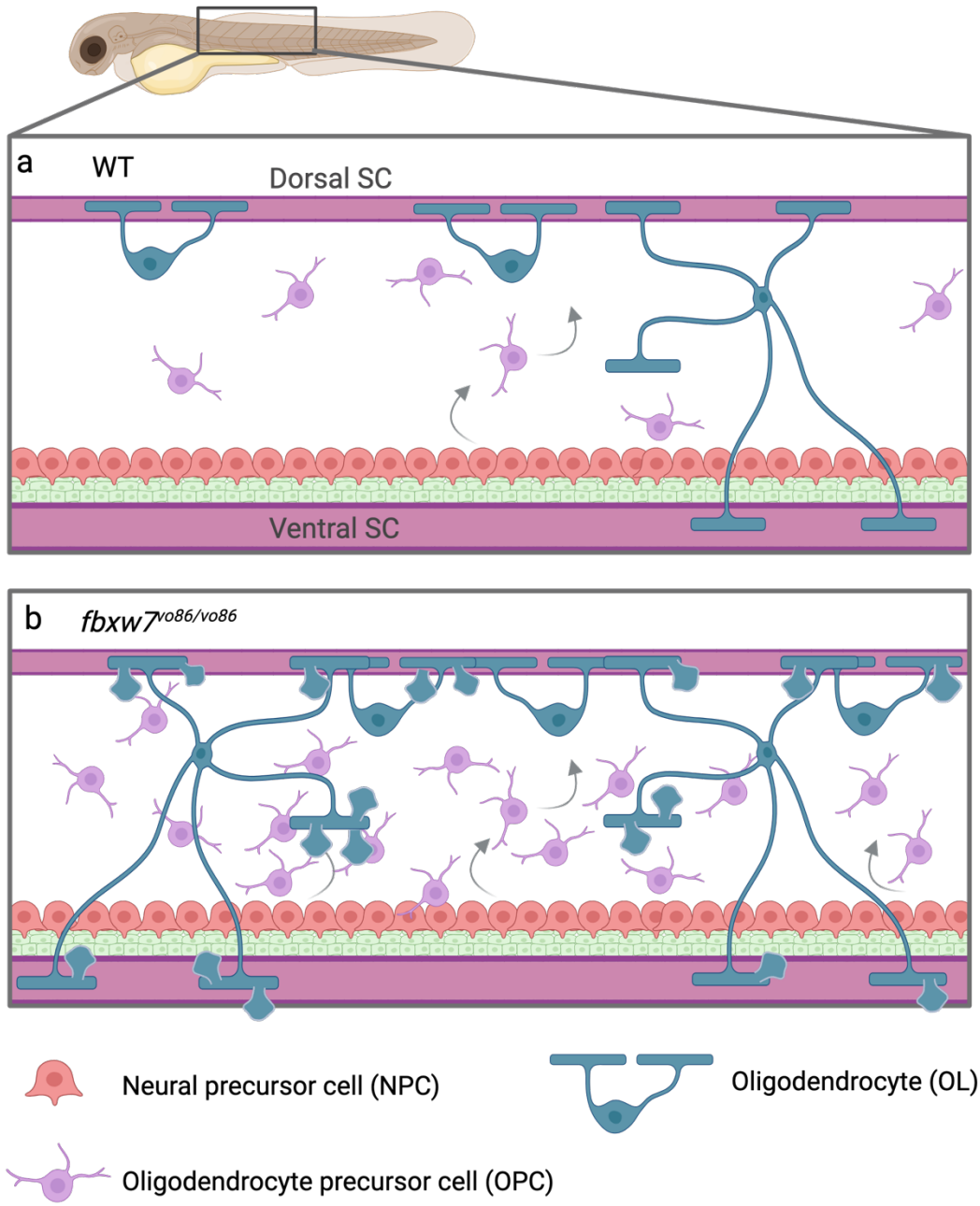
a
WT
Dorsal SC
Ventral SC
b
fbxw7vo86/vo86
Neural precursor cell (NPC)
Oligodendrocyte (OL)
Oligodendrocyte precursor cell (OPC)

Figure 3.14 Disruption of fbxw7 alters OL lineage dynamics in the zebrafish spinal cord

a Schematic of the wild-type (WT) zebrafish spinal cord showing balanced distribution of NPCs, OPCs, and OLs in dorsal and ventral regions of the spinal cord. **b** *fbxw7*$^{vo86/vo86}$ mutant zebrafish, there is an increase in OPC number and density throughout the spinal cord, with elevated differentiation into mature OLs which wrapped their membrane around neuronal cell bodies. NPCs (red), OPCs (purple), and OLs (blue) with directional arrows indicating OPC migration and differentiation. Created in BioRender.

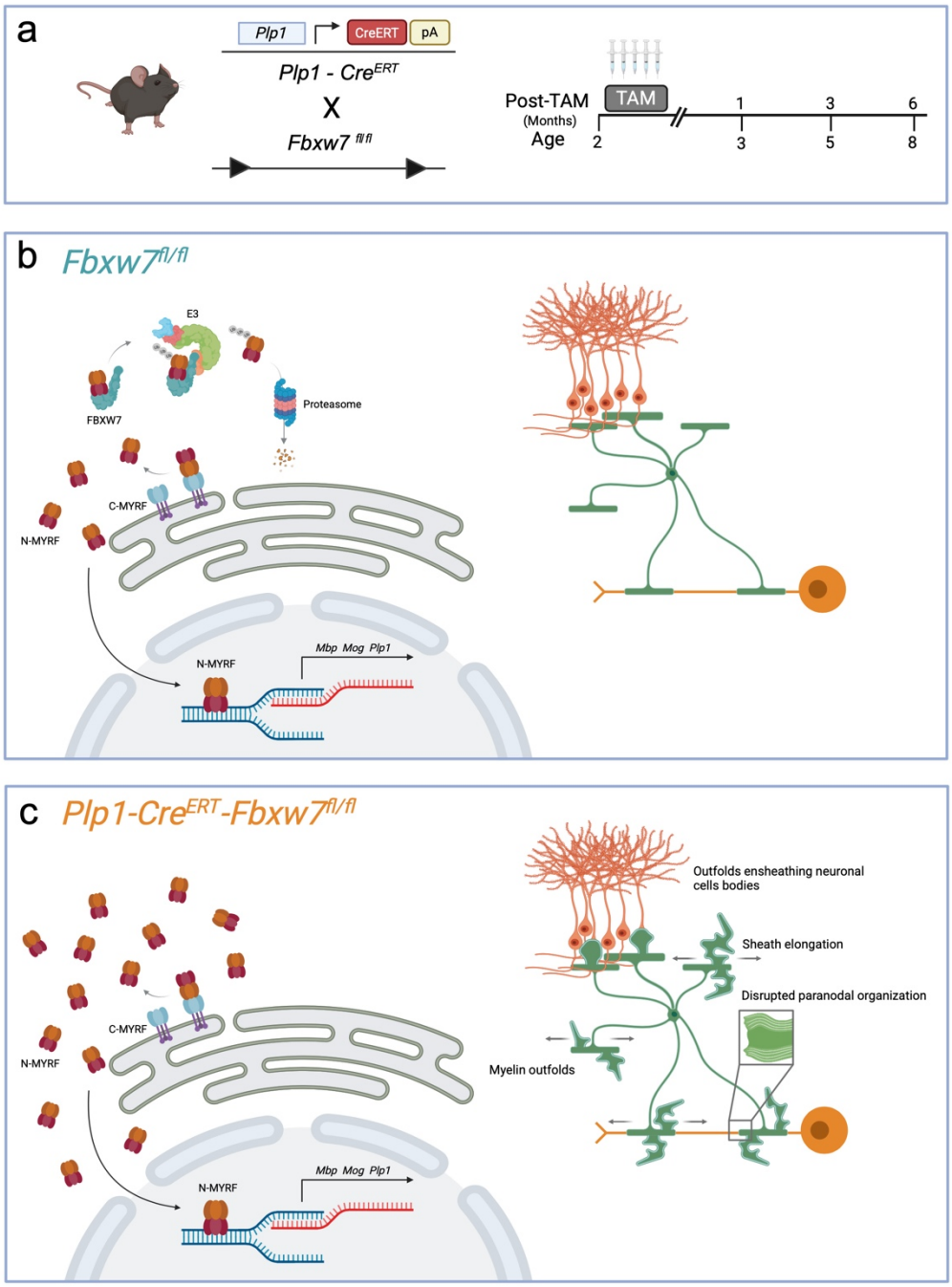
a
Plp1
CreERT
pA
Plp1 - CreERT
X
Fbxw7 fl/fl
Post-TAM
(Months)
Age
TAM
2
1
3
6
3
5
8
b
Fbxw7fl/fl
E3
FBXW7
Proteasome
C-MYRF
N-MYRF
N-MYRF
Mbp Mog Plp1
c
Plp1-CreERT-Fbxw7fl/fl
C-MYRF
N-MYRF
N-MYRF
Mbp Mog Plp1
Outfolds ensheathing neuronal cells bodies
Sheath elongation
Disrupted paranodal organization
Myelin outfolds

Figure 3.14 Conditional deletion of Fbxw7 in mature OL disrupts myelin organization and homeostasis

a Schematic of the *Plp1-Cre*^{ERT}*-Fbxw7*$^{fl/fl}$ inducible knockout strategy, with TAM administration at 2 months postnatal by analysis at 1-, 3-, and 6-months post-TAM. **b** In control *Fbxw7*$^{fl/fl}$ mice, FBXW7 targets MYRF for ubiquitin-mediated proteasomal degradation, maintaining balanced myelination. **c** In *Plp1-Cre*^{ERT}*-Fbxw7*$^{fl/fl}$ mice, loss of FBXW7 leads to MYRF accumulation, excessive myelin gene expression, formation of myelin outfolds, disorganized paranodes, and aberrant wrapping of neuronal cell bodies. Created in BioRender.

VIII. CHAPTER 4: Loss of *Fbxw7* in OL lineage cells results in OL loss, increased MYRF levels, and severe gliosis

Introduction

While we have demonstrated that FBXW7 binds and targets N-MYRF for proteasomal degradation to modulate myelin production and maintain homeostasis in mature OLs in the adult CNS, many critical questions remain regarding FBXW7's broader roles during earlier stages of OL lineage development. Previous studies have established FBXW7 as a key regulator of NSC maintenance, proliferation, and lineage commitment, acting through the degradation of canonical targets such as NOTCH1, C-JUN, and CYCLIN E[216,221,223,225,228]. In the zebrafish spinal cord, both our work and that of others have shown that *fbxw7* influences the specification of glial progenitors (Fig. 3.1, 3.2), likely through modulation of Notch1 pathway activity in NPCs[221]. Given the tightly timed transition from NPC to OPC during early CNS development[72,87], FBXW7's regulation of NOTCH1 could set the foundation for glial lineage commitment. However, whether FBXW7's role during this critical developmental window extends to the regulation of MYRF, or whether it impacts subsequent stages of OPC proliferation, differentiation, and survival, remains unresolved.

The experiments in this chapter were designed to directly address these open questions and define the stage-specific roles of FBXW7 during OL lineage progression. Specifically, we aimed to determine whether FBXW7-mediated degradation of MYRF occurs as early as the onset of OPC maturation and whether

this represents a critical checkpoint balancing transcriptional activation of the myelination program with environmental and developmental cues. Moreover, because prior zebrafish studies showed increased OPC numbers following *fbxw7* loss but could not distinguish whether this reflected enhanced specification from progenitors or increased proliferation of committed OPCs[221], the *Olig2-Cre* conditional knockout model provided an opportunity to disentangle these mechanisms in the mammalian CNS.

To investigate these questions, I generated conditional knockout (cKO) animals by crossing *Fbxw7*$^{fl/fl}$ mice[254] with *Olig2-Cre*[274] knock-in mice, a widely used tool for targeting the OL lineage due to Olig2's sustained expression from specification to mature OL stages. Recognizing that *Olig2-Cre* heterozygosity can modestly reduce OL number, *Olig2-Cre- Fbxw7*$^{wt/wt}$ littermates were used as controls in all experiments. Experimental and control cohorts were aged to postnatal and adult timepoints (P10, P21, P60, P90, and 6 months) for detailed molecular and cellular analyses.

Results

Developmental deletion of *Fbxw7* in Olig2-Cre animals results in elevated MYRF levels, OL loss, and severe gliosis

We observed that conditional deletion of *Fbxw7* in Olig2-expressing cells resulted in a significant increase in MYRF protein levels at postnatal day P10 and P21, without a corresponding change in the total number of OLs in the corpus callosum (Fig. 4.1a). Although there was a trend toward increased OL numbers at P21 (Fig. 4.1a, b), the study was underpowered to detect statistical significance.

Interestingly, by P60 we observed a significant reduction in OL density in the corpus callosum of *Olig2-Cre-Fbxw7*$^{fl/fl}$ animals relative to controls (Fig. 4.1a, b), a phenotype that persisted into adulthood (P90 and 6 months). While OL numbers did increase with age in the *Olig2-Cre-Fbxw7*$^{fl/fl}$ animals, they failed to reach control levels at any time point analyzed (Fig. 4.1a, b). Notably, despite the reduced number of OLs, MYRF protein levels remained aberrantly elevated in *Olig2-Cre-Fbxw7*$^{fl/fl}$ OLs at P60, as well as having increased intensity of CC1 and a hypertrophic morphology (Fig. 4.2a, b). While MYRF intensity did not reach significance at 6-months in *Olig2-Cre-Fbxw7*$^{fl/fl}$ OLs, there was an obvious trend to high MYRF levels, and additional data points would likely bring this difference to significance (Fig. 4.2c, d). This data suggests a sustained dysregulation of MYRF turnover in the absence of FBXW7.

To determine whether the observed OL loss was due to a cell-autonomous defect in OPCs, we isolated OPCs from P9 *Olig2-Cre-Fbxw7*$^{wt/wt}$ and *Olig2-Cre-Fbxw7*$^{fl/fl}$ mice for *in vitro* proliferation and differentiation assays. When cultured with PDGF-AA and pulsed with EdU for 6 hours, *Fbxw7*-deficient OPCs showed a significant reduction in EdU incorporation compared to controls (Fig. 4.1c), indicating impaired proliferative capacity. In parallel, differentiation assays revealed a significant decrease in the proportion of MBP+ OLs in *Fbxw7*-deficient cultures between 48 and 72 hours of differentiation (Fig. 4.1d, e), further supporting a functional role for FBXW7 in OPC expansion and survival.

Developmental deletion of *Fbxw7* in Olig2-Cre animals results in astrogliosis in the cortex

Given the significant *in vivo* and *in vitro* loss of OLs in *Olig2-Cre-Fbxw7*$^{fl/fl}$ mice, we next investigated whether this phenotype was associated with glial reactivity, which often accompanies demyelination. Astrocyte activation was quantified via GFAP immunoreactivity through the cerebral cortex. At early postnatal stages P10 and P21 before the onset of OL loss, there were no differences in astrocyte activation between control and *Olig2-Cre-Fbxw7*$^{fl/fl}$ animals (Fig. 4.3a). However, starting at P60 and persisting into later adulthood, we observed a robust increase in GFAP^{+} astrocytes, as well as increased microglial numbers by IBA1 staining in the cortex of *Olig2-Cre-Fbxw7*$^{fl/fl}$ animals (Fig. 4.3a-c), consistent with a chronic gliotic response. Although not quantitatively assessed, qualitative observations also revealed increased cortical volume and ventricular enlargement in several knockout brains, suggestive of broader structural abnormalities.

Olig2-Cre specificity

While unpublished data from the Emery lab suggest that elevated MYRF protein levels may be cytotoxic to differentiating OPCs, which could potentially account for the observed OL loss, it is important to note that *Olig2* is also transiently expressed in NPCs that give rise to both astrocytes and OLs[22]. Given the widespread and sustained astrocytic gliosis observed in *Olig2-Cre-Fbxw7*$^{fl/fl}$ animals, we questioned whether *Fbxw7* deletion in astrocyte precursors might also contribute to the observed phenotypes.

To assess the specificity of Cre-mediated recombination in this model, we crossed *Olig2-Cre* mice with the *Sun1-EGFP* Cre-reporter line[238], which drives nuclear envelope-localized EGFP in all *Cre* expressing cells. Immunohistochemical

analyses of P60 *Olig2-Cre-Sun1-EGFP* animals revealed a substantial number of GFP$^+$ nuclei co-localizing with GFAP$^+$ astrocytes in multiple brain regions, including the corpus callosum, cortex, hippocampus, and striatum (Fig. 4.4a). Additionally, in the hippocampus many PDGFRα$^+$ OPCs did not have GFP+ nuclei, suggesting that *Olig2-Cre* was not inducing recombination of the reporter allele in all Olig2$^+$ OPCs in the hippocampus (Fig. 4.4b). These results indicate that *Olig2-Cre* drives recombination in a broader population than the OL lineage alone, including a substantial subset of astrocytes. While the Sun1-EGFP reporter serves as an indirect proxy for likely recombination of the *loxP* flanked *Fbxw7* allele, the widespread labeling of GFAP$^+$ astrocytes underscores the limitations of the *Olig2-Cre* driver in achieving OL-lineage specificity. Together, these data raise the possibility that astrocytic loss of *Fbxw7* may contribute to both the observed gliosis and possibly a secondary effect on OL survival in the *Olig2-Cre-Fbxw7$^{fl/fl}$* model.

Myrf haploinsufficiency was not sufficient to reduce gliosis

To directly test whether elevated MYRF levels in OLs were sufficient to cause the observed OL loss and gliosis, we performed a genetic epistasis experiment by crossing *Olig2-Cre-Fbxw7$^{fl/fl}$* animals to the established *Myrf$^{fl/fl}$* line to generate *Olig2-Cre-Fbxw7$^{fl/fl}$; Myrf$^{fl/wt}$* mice. If elevated MYRF were the sole driver of OL loss and astrocyte activation, partial reduction of MYRF could alleviate these phenotypes as we found in our *Plp1-Cre^{ERT}-Fbxw7$^{fl/fl}$* characterized in chapter 3. However, at P60, GFAP immunostaining revealed no reduction in astrocyte reactivity in *Olig2-Cre-Fbxw7$^{fl/fl}$; Myrf$^{fl/wt}$* compared to *Olig2-Cre-Fbxw7$^{fl/fl}$* (Fig. 4.5a).

Discussion

In the developing CNS, OPCs arise from NPCs within the SVZ[72], a process tightly controlled by intrinsic transcription factors and extrinsic cues. A key player in this transition is OLIG2[71,87], which suppresses neuronal fate and promotes commitment to the glial lineage via downstream regulators like SOX10[150,161,162]. Because of its expression throughout the OL lineage, *Olig2-Cre* has been widely used to study OL development, though its activity in early progenitors complicates interpretation of cell-type-specific phenotypes.

Our data reveal a critical role for FBXW7 in maintaining OL homeostasis during postnatal development. Conditional deletion of *Fbxw7* using *Olig2-Cre* led to elevated MYRF protein levels at P60, which showed a similar trend at 6-months of age. Additionally, we found that around P60 there was a significant loss of OLs in the corpus callosum of *Olig2-Cre-Fbxw7$^{fl/fl}$* animals, and while the number of OLs did increase over time, it never reached control levels.

These results are consistent with our findings that FBXW7 targets MYRF for degradation to constrain myelin production in mature OLs. This work extends those findings to earlier stages of the lineage, suggesting that disruption of FBXW7-MYRF signaling during early OPC differentiation may impair lineage progression and long-term cell survival. Notably, these observations align with emerging evidence from the Hill lab and others showing that newly differentiated, immature OLs are particularly vulnerable to cell death compared to their mature counterparts, likely due to the metabolic demands and cellular stress associated with initiating myelin production[275]. Our data raise the possibility that loss of

FBXW7 amplifies this vulnerability by disrupting the fine-tuning of MYRF activity, pushing immature OLs into a dysregulated state that compromises their survival and reduces the pool of mature, myelinating cells.

In vitro assays revealed that OPCs lacking *Fbxw7* had reduced proliferation and differentiation capacity, indicating a cell-intrinsic requirement for FBXW7 in maintaining OPC function. This aligns with previous studies linking FBXW7 to the control of NPC viability and lineage commitment through degradation of key signaling proteins such as NOTCH1 and c-JUN[216,223]. In the OL lineage, NOTCH1 signaling plays a well-established role in maintaining OPCs in an undifferentiated, proliferative state and inhibiting their terminal differentiation[90,162,175,245]. Similarly, c-JUN, a component of the AP-1 transcriptional complex, has been implicated in stress responses and cell survival in glial cells[170,276]. Studies in neural stem and progenitor populations have shown that FBXW7-mediated degradation of NOTCH1 and c-JUN is critical for balancing proliferation, differentiation, and survival[221,223,225]. By analogy, our findings suggest that FBXW7 may act as a gatekeeper throughout multiple stages of glial development, ensuring the proper transition from proliferative OPCs to differentiated OLs by modulating the abundance of these and possibly other regulatory proteins. Disruption of this balance, as seen in *Fbxw7*-deficient OPCs, likely contributes to impaired lineage progression and compromised OL survival.

Additionally, we observed widespread astrogliosis and microglial activation beginning at P60 in FBXW7-deficient animals. *Cre*-reporter analysis using Sun1-EGFP revealed recombination in GFAP$^+$ astrocytes, confirming that *Olig2-Cre*

activity extends beyond the OL lineage. This raised the possibility that astrocyte-intrinsic loss of FBXW7 could contribute to OL loss and neuroinflammation through non-cell-autonomous mechanisms.

To test whether MYRF elevation alone accounted for these effects, we performed an epistasis experiment by crossing our *Olig2-Cre-Fbxw7*$^{fl/fl}$ animals into a *Myrf* heterozygous background. However, *Myrf* haploinsufficiency failed to rescue the observed gliosis and neuroinflammation, indicating that in differentiating OPCs, either *Myrf* haploinsufficiency was not sufficient to bring MYRF levels back down to acceptable levels, or loss of *Fbxw7* function astrocytes was contributing to OL loss. Additionally, it is also possible that other FBXW7 substrates besides N-MYRF were contributing to the observed phenotypes.

Collectively, our findings support a model in which FBXW7 acts as a multifaceted regulator of OPC biology, with distinct functions in lineage specification, proliferation, differentiation, and long-term OL survival and maintenance. While elevated MYRF contributes to dysregulation of myelin homeostasis, FBXW7's influence extends beyond a single substrate, and may help coordinate broader transcriptional and signaling programs essential for glial health.

Future work employing temporally inducible and lineage-restricted *Cre* drivers will be critical to definitively separate the OL-intrinsic versus astrocyte-mediated consequences of FBXW7 loss. For example, the *Sox10-Cre*^{ERT} lines[108] allow for tamoxifen-inducible, OL-specific recombination in postnatal and adult animals, minimizing off-target recombination in astrocytes and avoiding potential developmental effects. These drivers would enable precise dissection of FBXW7

function in mature OLs, bypassing earlier lineage stages. On the other hand, astrocyte-specific Cre lines such as *Aldh1l1-CreERT*[277] or *Gfap-Cre*^{ERT}[278] could be employed to directly assess the contribution of astrocytic *Fbxw7* loss to the gliotic phenotype. While inducible systems offer the advantage of temporal control and cell-type specificity, they also have limitations, including variable recombination efficiency and potential tamoxifen toxicity or off-target effects[279]. Therefore, combining multiple *Cre* drivers, along with careful recombination validation and complementary *in vitro* approaches, will be essential to fully delineate the cell-autonomous and non–cell-autonomous roles of FBXW7 in CNS glial population.

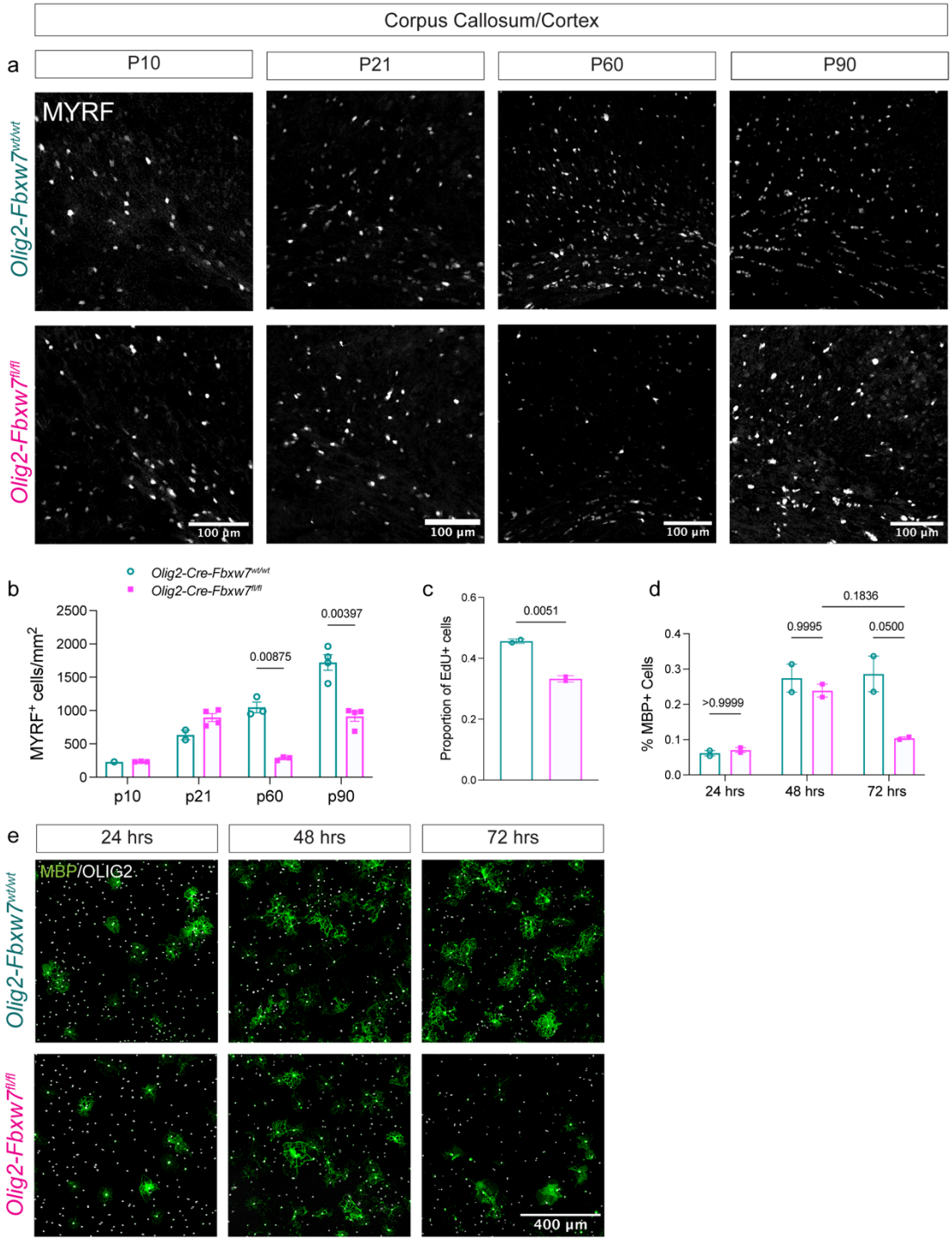
Corpus Callosum/Cortex
a
P10
P21
P60
P90
MYRF
Olig2-Fbxw7wt/wt
Olig2-Fbxw7fl/fl
100 µm
b
Olig2-Cre-Fbxw7wt/wt
Olig2-Cre-Fbxw7fl/fl
MYRF+ cells/mm2
0.00875
0.00397
p10
p21
p60
p90
c
Proportion of EdU+ cells
0.0051
d
% MBP+ Cells
>0.9999
0.9995
0.0500
0.1836
24 hrs
48 hrs
72 hrs
e
MBP/OLIG2
400 µm

Figure 4.1 Developmental deletion of Fbxw7 in Olig2-Cre animals results in OL loss

a Representative images of the corpus callosum from *Olig2-Cre-Fbxw7*$^{wt/wt}$ and *Olig2-Cre-Fbxw7*$^{fl/fl}$ mice at P10, P21, P60, and P90 stained for MYRF. **b** Quantification of MYRF^{+} cells in the corpus callosum from *Olig2-Cre-Fbxw7*$^{wt/wt}$ and *Olig2-Cre-Fbxw7*$^{fl/fl}$ mice at P10 (N=1, 3), P21 (N=2, 4), P60 (N=3, 3), and P90 (N=4, 4). Data shown as average ± SEM. Statistical significance determined by two-way ANOVA. **c** Quantification of EdU incorporation in primary OPCs from *Olig2-Cre-Fbxw7*$^{wt/wt}$ and *Olig2-Cre-Fbxw7*$^{fl/fl}$ mice at P10. Average ± SEM, (N = 2) (independent cell isolations) with 2 technical replicates (coverslips). Statistical significance determined by unpaired, two-tailed Student's t test. **d** Quantification of MBP+ OLs normalized to total OLIG2+ cells. Average ± SEM, (N = 2 independent cell isolations). **e** Representative images of cultured *Olig2-Cre-Fbxw7*$^{wt/wt}$ and *Olig2-Cre-Fbxw7*$^{fl/fl}$ OLs after 24, 48, and 72 hrs of differentiation stained with MBP and OLIG2.

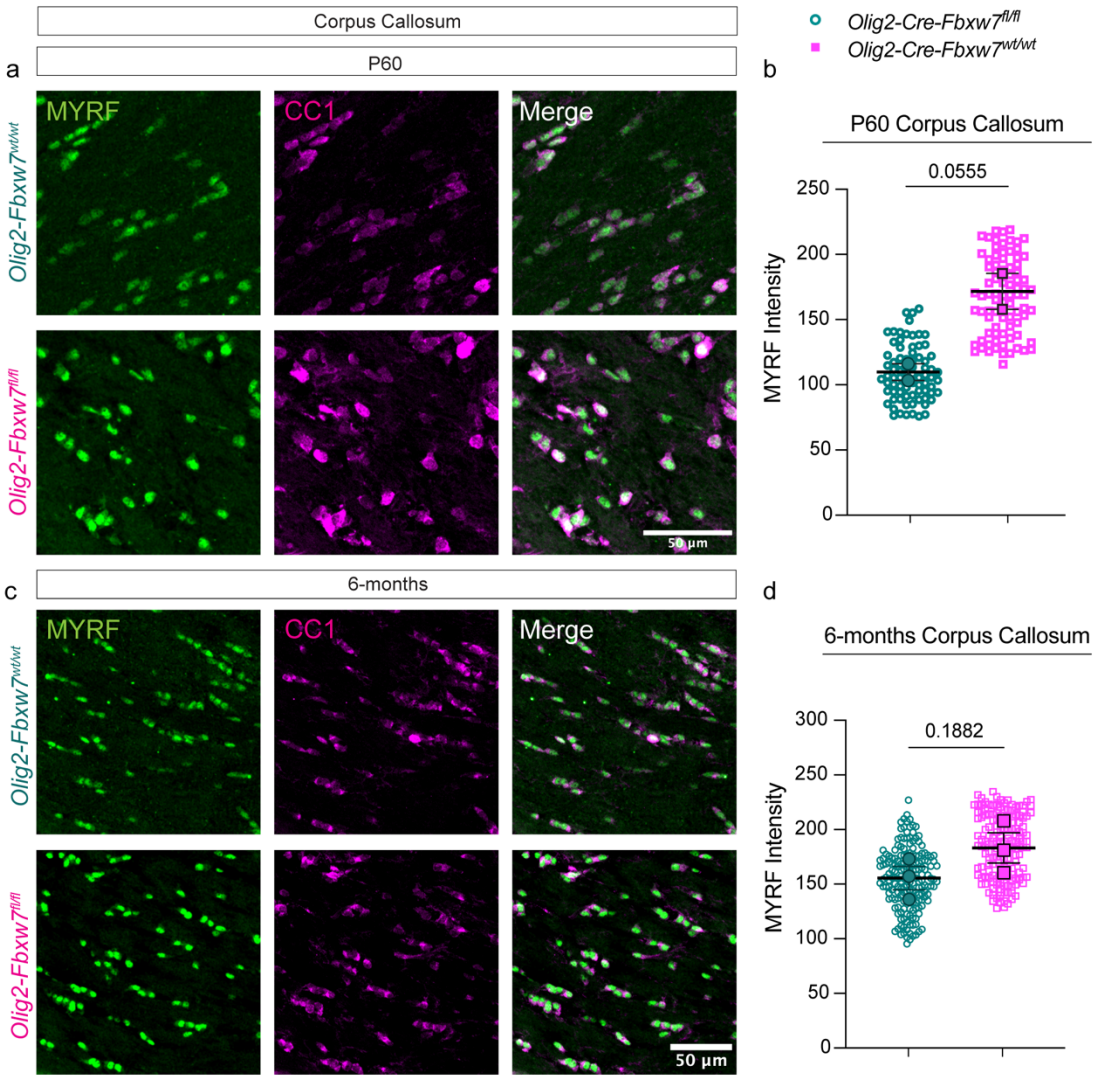
Corpus Callosum
a
P60
MYRF
CC1
Merge
Olig2-Fbxw7wt/wt
Olig2-Fbxw7fl/fl
50 µm
b
Olig2-Cre-Fbxw7fl/fl
Olig2-Cre-Fbxw7wt/wt
P60 Corpus Callosum
0.0555
MYRF Intensity
250
200
150
100
50
0
c
6-months
MYRF
CC1
Merge
Olig2-Fbxw7wt/wt
Olig2-Fbxw7fl/fl
50 µm
d
6-months Corpus Callosum
0.1882
MYRF Intensity
300
250
200
150
100
50
0

Figure 4.2 Developmental deletion of Fbxw7 in Olig2-Cre animals results in increase MYRF levels in the corpus callosum

a Representative images of the corpus callosum from *Olig2-Cre-Fbxw7*$^{wt/wt}$ and *Olig2-Cre-Fbxw7*$^{fl/fl}$ mice at P21 for MYRF and CC1. **b** Quantification of nuclear MYRF intensity in the corpus callosum of *Olig2-Cre-Fbxw7*$^{wt/wt}$ and *Olig2-Cre-Fbxw7*$^{fl/fl}$ mice at P21 (N=2, 2). **c** Representative images of the corpus callosum from *Olig2-Cre-Fbxw7*$^{wt/wt}$ and *Olig2-Cre-Fbxw7*$^{fl/fl}$ mice at P60 for MYRF and CC1. **d** Quantification of nuclear MYRF intensity in the corpus callosum of *Olig2-Cre-Fbxw7*$^{wt/wt}$ and *Olig2-Cre-Fbxw7*$^{fl/fl}$ mice at P60 (N=3, 3). Statistical significance determined by unpaired, two-tailed Student's t test. Average ± SEM. Statistics were performed on animal averages.

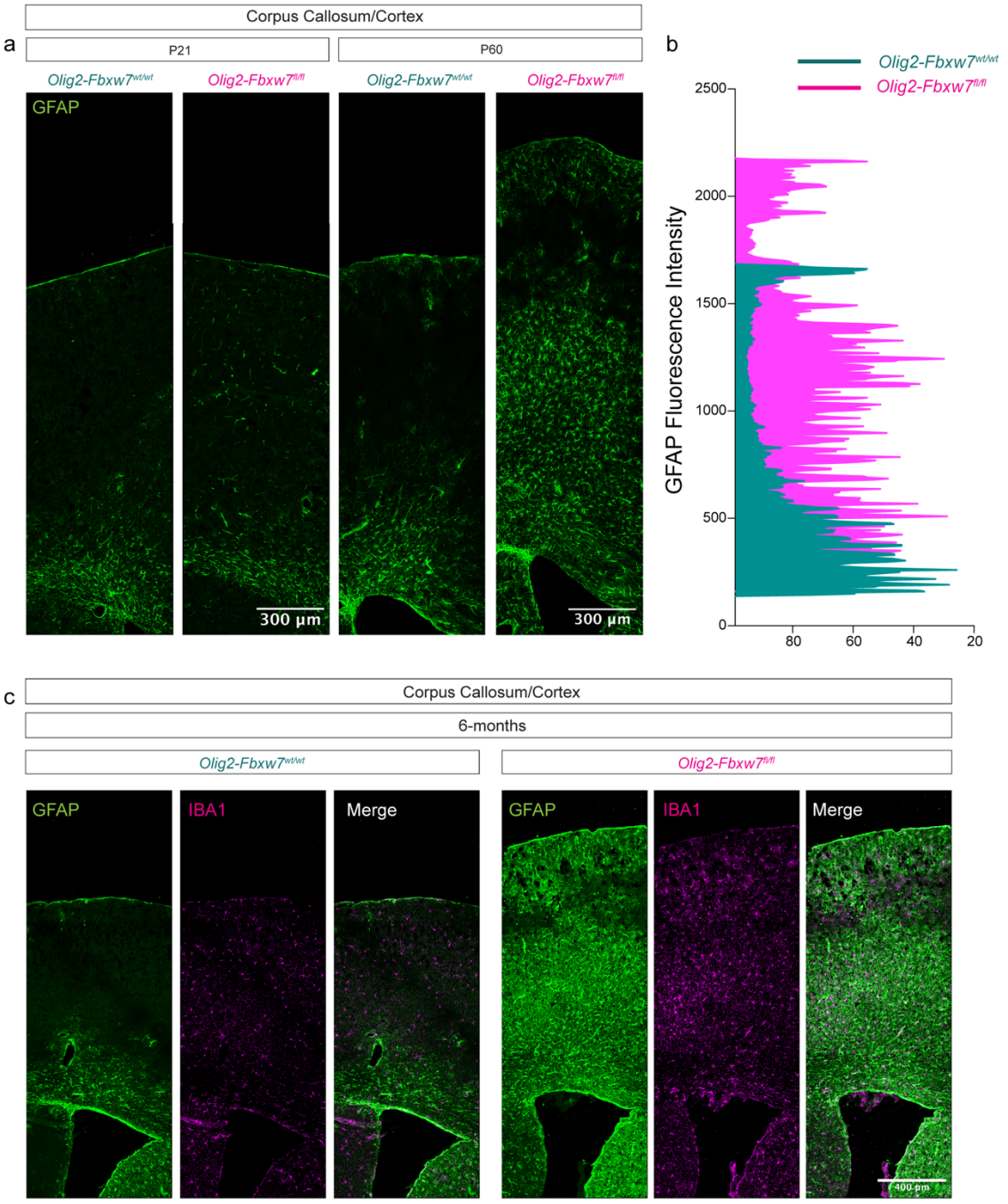
a
Corpus Callosum/Cortex
P21
P60
Olig2-Fbxw7wt/wt
Olig2-Fbxw7fl/fl
Olig2-Fbxw7wt/wt
Olig2-Fbxw7fl/fl
GFAP
300 µm
300 µm
b
Olig2-Fbxw7wt/wt
Olig2-Fbxw7fl/fl
GFAP Fluorescence Intensity
2500
2000
1500
1000
500
0
80
60
40
20
c
Corpus Callosum/Cortex
6-months
Olig2-Fbxw7wt/wt
Olig2-Fbxw7fl/fl
GFAP
IBA1
Merge
GFAP
IBA1
Merge
400 µm

Figure 4.3 Developmental deletion of Fbxw7 in Olig2-Cre animals results in astrogliosis in the cortex

a Representative images of the corpus callosum and cortex from *Olig2-Cre-Fbxw7*$^{wt/wt}$ and *Olig2-Cre-Fbxw7*$^{fl/fl}$ mice at P21 and P60 stained for GFAP **b** Intensity histograms for GFAP intensity from the corpus callosum up through the cortex in P60 *Olig2-Cre-Fbxw7*$^{wt/wt}$ and *Olig2-Cre-Fbxw7*$^{fl/f}$ animals. **c** Representative images of the corpus callosum and cortex from *Olig2-Cre-Fbxw7*$^{wt/wt}$ and *Olig2-Cre-Fbxw7*$^{fl/fl}$ mice at 6-months stained for GFAP and IBA1.

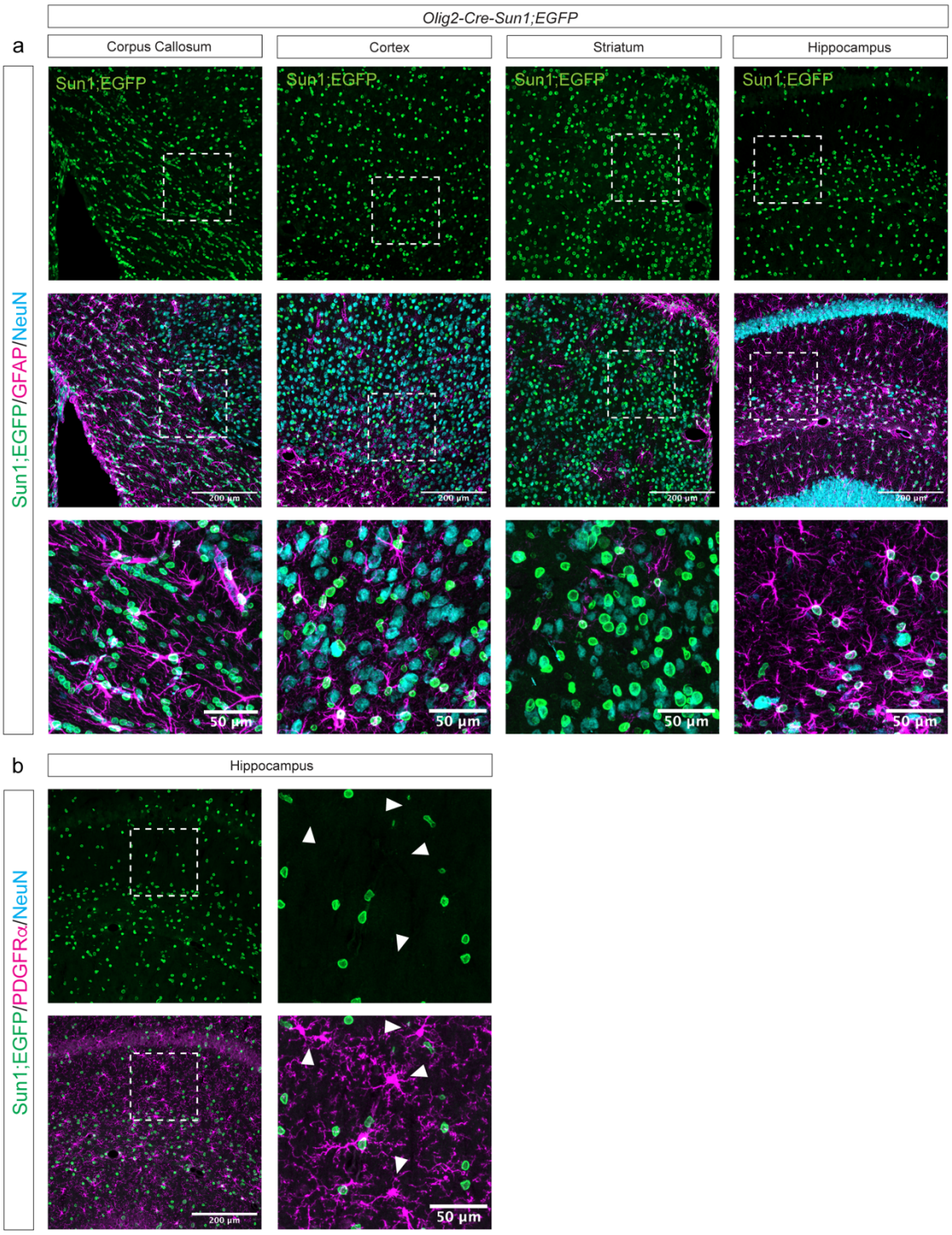
Olig2-Cre-Sun1;EGFP
a
Corpus Callosum
Cortex
Striatum
Hippocampus
Sun1;EGFP
Sun1;EGFP/GFAP/NeuN
200 µm
50 µm
b
Hippocampus
Sun1;EGFP/PDGFRα/NeuN
200 µm
50 µm

Figure 4.4 Olig-Cre;Sun1-EGFP animals show significant recombination in non-OL lineage cells

a Representative images of the corpus callosum, cortex, striatum, and hippocampus from *Olig-Cre;Sun1-EGFP* mice at P60 stained for GFP (green), GFAP (magenta), and NeuN (cyan). **b** Representative images of hippocampus from *Olig-Cre;Sun1-EGFP* mice at P60 stained for GFP and PDGFRα. Arrowheads are pointing to PDGRFα^{+}/GFP^{-} cells.

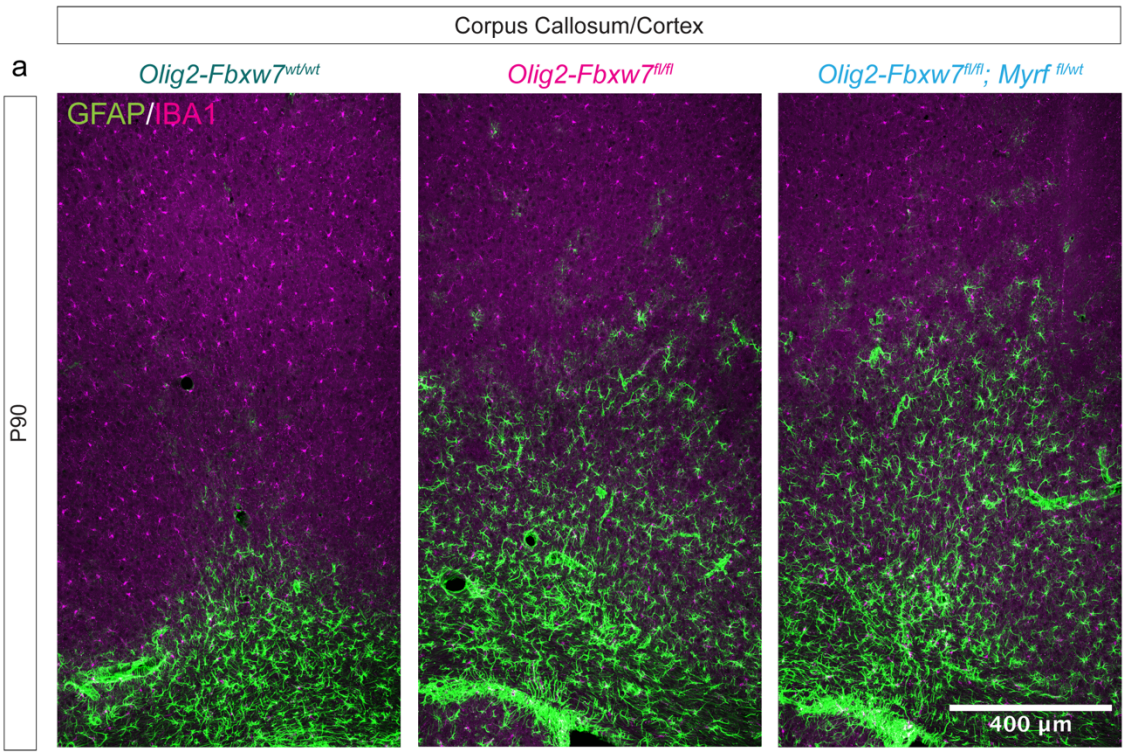
Corpus Callosum/Cortex
a
Olig2-Fbxw7wt/wt
Olig2-Fbxw7fl/fl
Olig2-Fbxw7fl/fl; Myrf fl/wt
GFAP/IBA1
P90
400 µm

Figure 4.5 Myrf haploinsufficiency was not sufficient to suppress in the cortex of Olig2-Cre-Fbxw7$^{fl/fl}$ animals

a Representative images of the corpus callosum and cortex from *Olig2-Cre-Fbxw7$^{wt/wt}$*, *Olig2-Cre-Fbxw7$^{fl/fl}$* and *Olig2-Cre-Fbxw7$^{fl/fl}$; Myrf$^{fl/wt}$* mice at P60 stained for GFAP and IBA1.

IX. CHAPTER 5: SUMMARY, CONCLUSIONS, AND FUTURE DIRECTIONS

Myelination in the CNS is a tightly orchestrated biological process that enables rapid impulse conduction and supports long-term neuronal health[199]. OLs, the myelinating glial cells of the CNS, achieve this by extending and wrapping their membranes around axons to form multilamellar myelin sheaths[94,154,250]. These sheaths insulate axons, optimize signal propagation, and provide metabolic support critical for neuronal survival[81,102,104]. While extrinsic cues such as axon diameter[81,98,102] and neuronal activity modulate OL behavior[80,82,111,174], it is increasingly clear that intrinsic transcriptional and post-translational mechanisms define the competence of OLs to differentiate, myelinate, and maintain sheath integrity across the lifespan[92,140,151,163].

Our work identifies F-box and WD repeat domain-containing protein 7 (FBXW7), a substrate recognition subunit of the SCF (SKP1–CUL1–F-box) E3 ubiquitin ligase complex, as a pivotal negative regulator of OL myelination and homeostasis. FBXW7 is a known tumor suppressor, broadly expressed across tissues, and functions through the selective degradation of key intracellular proteins[216,218,219]. In this study, we establish that FBXW7 is not only expressed throughout the OL lineage but is essential for balancing myelin growth, sheath organization, and overall OL health in both development and adulthood.

Using an integrative approach combining zebrafish models, primary OL cultures, and inducible cKO mouse lines, we demonstrate that FBXW7 modulates OL behavior in a temporally dynamic and context-dependent manner. In early

development, FBXW7 restricts OPC production by repressing NOTCH1 signaling in NPCs[221,223], thus fine-tuning the transition from progenitor to glial lineage. We found that in adult myelinating OLs, FBXW7 restrains excessive myelin production and prevents structural anomalies such as sheath outfolds, disorganized paranodes, and the ectopic wrapping of neuronal cell bodies.

Central to FBXW7's function in mature OLs is its regulation of MYRF, a membrane-bound transcription factor required for OL differentiation and myelin gene expression[151,163]. We demonstrate that the N-terminal cleavage product of MYRF (N-MYRF) is a direct target of FBXW7 in OLs. Upon *Fbxw7* deletion, levels of N-MYRF accumulate, leading to transcriptional dysregulation and overproduction of myelin components. Notably, *Myrf* haploinsufficiency significantly rescues both OL numbers in the zebrafish spinal cord and myelin structural anomalies in *Fbxw7*-deficient mice, underscoring FBXW7 as a key mediator of MYRF function. Importantly, both in zebrafish and in mouse models, loss of *fbxw7*/*Fbxw7* triggers rapid, short-term increases in myelin sheath length, followed by the emergence of aberrant myelin outfoldings and structural abnormalities. These two-phase phenotypes highlight the critical role of FBXW7 in fine-tuning MYRF-driven myelin production, ensuring that initial sheath growth is properly calibrated, and that long-term myelin architecture is maintained. Together, these findings position FBXW7 as a central checkpoint in regulating MYRF activity and maintaining myelin homeostasis across vertebrate species. The distinct phenotypes observed following *Fbxw7* deletion at different lineage stages emphasize the importance of temporal specificity in its regulatory role. For instance, early deletion via *Olig2-Cre*

leads to OL loss, astrogliosis, and neuroinflammation, possibly due to impaired OPC maturation and increased cellular stress, while deletion in mature OLs via *Plp1-Cre*^{ERT} induced sheath elongation and pathological remodeling without overt cell death. These findings highlight a dual role for FBXW7: it acts as a developmental gatekeeper, ensuring orderly OPC-to-OL transition, and as a homeostatic regulator in mature OLs, maintaining sheath architecture and preventing aberrant growth.

Interestingly, the divergent phenotypes we observed in the CNS differ markedly from those reported in the PNS, where FBXW7 restricts Schwann cell (SC) number and myelin thickness without affecting sheath length[225]. These discrepancies may reflect fundamental differences in the biology of CNS versus PNS glia[199,202] or may be attributed to the developmental timing and regional specificity of *Cre* drivers used in each context. In the SC studies, FBXW7 was ablated early during development using *Dhh-Cre*, whereas OL deletion was restricted to adulthood in our *Plp1-Cre*^{ERT}. This raises compelling questions about whether FBXW7 regulates different targets at distinct lineage stages and how temporal context determines its functional outcomes. In OLs, we have shown that FBXW7 targets MYRF, a CNS-restricted transcription factor critical for initiating and maintaining myelin gene expression. By contrast, in SCs, FBXW7 may preferentially regulate proteins such as c-Jun, a key negative regulator of PNS myelination[280], or components of the NRG1/ErbB pathway, which are essential for axon-caliber–dependent myelin growth[209]. Thus, both cellular context and developmental timing

likely shape the substrate specificity and downstream consequences of FBXW7 activity.

Indeed, our proteomic studies support the notion of cell-type and stage-specific FBXW7 targets. Unbiased LC-MS analysis of FBXW7-interacting proteins in primary OLs revealed several novel candidates in addition to MYRF[92,163], including MYCBP2[261], MAP1B[281,282], and RAE1[283]. While MYRF emerged as a critical effector of FBXW7-mediated myelin regulation, the roles of MAP1B and RAE1 remain largely unexplored in the context of OLs. Notably, MAP1B is a microtubule-associated protein that has been implicated in cytoskeletal organization, process outgrowth, and membrane trafficking in OLs, all of which are essential for proper myelin sheath formation and maintenance[281,282]. Given that *Fbxw7* mutants display early increases in myelin sheath length followed by the development of abnormal outfoldings, it is tempting to speculate that dysregulated MAP1B turnover could contribute to these phenotypes by disrupting cytoskeletal dynamics and impairing the fine-tuning of sheath architecture. Future studies aimed at testing whether MAP1B is a functional substrate of FBXW7 in OLs, and whether its dysregulation accounts for some of the observed morphological abnormalities, will be important for further elucidating the mechanistic network downstream of FBXW7. MYCBP2, previously identified as a non-E3 FBXW7 interactor in neurons[261], may also modulate FBXW7 activity independently, presenting a potential additional layer of regulation in OLs.

Our findings regarding *Myrf* transcriptional regulation are particularly intriguing. *Myrf* is subject to transcriptional control by SOX10[161] and ZFP24[271], and post-

transcriptional inhibition by miR-145-5p[272]. Following *Fbxw7* deletion, we observed an increase in N-MYRF protein that was accompanied by a compensatory reduction in *Myrf* mRNA, suggesting a feedback loop aimed at restoring homeostasis. This transcriptional downregulation correlated with reduced ZFP24 levels in FBXW7-deficient OLs, indicating that FBXW7 may indirectly regulate *Myrf* transcription via modulation of upstream transcription factors. Furthermore, despite similar transcript reductions in both optic nerve and cerebellum, N-MYRF protein was only reduced in the optic nerve at later timepoints, hinting at regional variability in MYRF stability or translation. These results open exciting avenues to explore circuit-specific regulation of OL transcriptional programs and the possibility that neuronal context shapes the requirements for MYRF in mature OLs.

Another compelling observation is the regional specificity of ectopic cell body myelination in the cerebellum of *Plp1-CreERT-Fbxw7*$^{fl/fl}$ mice. This phenotype, characterized by myelin outfolds ensheathing cerebellar granule cell nuclei, was not observed in other brain regions despite widespread *Fbxw7* deletion. It is tempting to speculate that the dense packing and small diameter of granule cell bodies render them especially susceptible to mistargeted myelin. Similar phenotypes have been reported in the cerebellum of toads[264], squirrel monkeys[265], and mice with perturbed myelin-associated adhesion molecules[267,273]. Our findings align with these reports and suggest that the cerebellum may be uniquely vulnerable to OL-intrinsic dysregulation of adhesion or growth control mechanisms.

Consistent with this, deletion of *Fbxw7* in OLs dysregulated the expression of numerous cell adhesion molecules previously implicated in sheath targeting and structural integrity. These include MAG[284], CNTP1[101], CNTN1[285], and NFASC155[273] adhesion proteins essential for paranodal loop formation and axon-glia communication. Intriguingly, global deletion of these molecules in zebrafish and mice phenocopies the structural anomalies observed in our *Fbxw7* cKO model[267,273]. This supports a model wherein FBXW7 ensures appropriate myelin targeting and sheath organization.

Our study also sheds light on potential consequences of myelin dysregulation for neuronal health. The presence of pathological myelin structures in *Fbxw7*-deficient mice coincides with signs of axonal stress, particularly in the cerebellum, where myelinated axons, potentially Purkinje axons, exhibited intracellular accumulations and abnormalities[257]. Whether these changes result from impaired metabolic support, disrupted axon-glia signaling, or mechanical stress imposed by redundant myelin remains to be elucidated. Given the critical importance of OL-axon interactions for long-term neuronal viability[103], understanding how inappropriate myelination affects circuit function will be a key focus of future research.

Looking forward, several important questions arise from our work. First, how does FBXW7 select distinct targets at different stages of OL development? The mechanisms underlying substrate specificity remain poorly understood. While canonical FBXW7 targets require a phosphodegron motif and priming by GSK3β or CDK5, our data suggest that N-MYRF degradation in OLs may occur independently of these kinases. Identifying the priming events, cofactors, and

structural requirements for FBXW7-substrate interaction in OLs will be critical to map the broader regulatory landscape.

Second, what are the consequences of FBXW7 dysregulation in pathological contexts? Given that OLs remain plastic throughout adulthood and continue to remodel sheaths in response to experience and injury[107,203,250], FBXW7 may represent a molecular brake that curtails excessive or aberrant myelin remodeling. In diseases such as multiple sclerosis[148], where remyelination is often incomplete or dysfunctional, transient inhibition of FBXW7 might boost MYRF levels and enhance repair. Conversely, chronic downregulation of FBXW7, as seen in certain cancers or in response to inflammation[216], could contribute to myelin pathology. Exploring the context-dependent roles of FBXW7 in disease and repair settings may uncover new therapeutic avenues.

Third, how does FBXW7 interact with other known regulators of OL development and function? FBXW7 is embedded in a complex regulatory network that includes upstream signals like NOTCH1[221] and mTOR[222,228], as well as downstream effectors such as MYRF[229] and adhesion molecules. Dissecting these interactions will help clarify whether FBXW7 serves as an integrative hub or functions in parallel with other signaling pathways to sculpt myelination.

Finally, our work points to the broader importance of proteostatic mechanisms in OL biology. As long-lived cells[73,109] operating in a high-demand metabolic environment[129], OLs must precisely balance protein synthesis, trafficking, and degradation. The selective degradation of key transcription factors and structural proteins by E3 ligases like FBXW7 likely plays a crucial role in this balance. Future

efforts aimed at profiling the OL ubiquitinome across development, aging, and disease may reveal additional layers of regulation and new molecular targets.

In conclusion, this work identifies FBXW7 as a central regulator of OL lineage progression and myelin homeostasis. By targeting N-MYRF and potentially other lineage-specific substrates, FBXW7 restrains excessive myelin growth and preserves sheath organization in the adult CNS. Its loss disrupts these processes, leading to striking structural and potentially functional abnormalities. As a molecular brake on the myelination program, FBXW7 provides a critical checkpoint in OL development and maintenance, with important implications for understanding myelin plasticity, disease, and repair.

X. APPENDIX I

LC/MS proteins with a > +/- 1.2 fold change in primary rat *Fbxw7* knockdown OLs

Proteins were sorted by fold change and values for: log fold change (logFC), fold change (FC), P-value, false discovery rate (FDR), average siControl peptide count, average *siFbxw7* peptide count, direction change, candidate ranking sorted based on FDR (non > 0.1, low < 0.1, med < 0.05, high < 0.01), primary protein name, alternative protein names, identifier, accession, other accessions, uniprot gene name, other gene synonyms, species, uniprot link, key words, gene ontology terms (GO): biological process, GO: cellular component, GO: molecular function, reactome pathway, were reported. Experimental details are in chapter 2.13 and 2.15.

logFC	FC	PValue	FDR	UniProt Gene Name
1.788240361	3.45	6.9877E-41	6.95276E-38	GPD1
1.647259756	3.134602975	0.005305377	0.040509008	TMEM98
1.570711137	2.970547158	1.97101E-63	2.94173E-60	ITGB3
1.543154397	2.914295671	1.8946E-110	5.6555E-107	DPYSL5
1.180766343	2.266971431	2.97746E-17	5.22807E-15	MYO1D
1.093772397	2.134305689	1.1143E-20	2.21745E-18	FAM107B
1.011188602	2.015572543	6.47568E-28	2.76142E-25	VSNL1
0.948908871	1.930403274	1.75041E-05	0.000367955	PPP1R14A
0.91277008	1.882696748	0.000118677	0.00200142	PEX11A
0.854822759	1.808536478	7.47562E-32	4.46294E-29	PEA15
0.787218841	1.725728477	5.38433E-08	2.26369E-06	PEX5L
0.773325471	1.709203043	2.88449E-26	1.07628E-23	SGK2
0.749411329	1.68110557	3.64367E-09	1.84345E-07	GJC2
0.734552137	1.663880864	5.29943E-10	3.16376E-08	BCAN
0.734262172	1.663545266	1.05257E-24	3.14193E-22	HOMER3
0.710998968	1.63693501	9.1596E-07	2.84806E-05	ENTPD5
0.698659829	1.62298977	3.34837E-24	9.08626E-22	SV2A
0.690963526	1.614351455	1.57397E-22	3.61407E-20	GRM7
0.677658449	1.599541144	5.13284E-11	3.56314E-09	EML2
0.670996601	1.592168345	0.001611849	0.01676435	GMFG
0.655980315	1.575685806	6.04394E-32	4.46294E-29	ACY1A
0.638972556	1.557219646	1.89286E-13	1.94834E-11	CYP51A1
0.592635006	1.507997156	4.20485E-17	6.97305E-15	APLP2
0.582413122	1.497351525	4.34929E-07	1.4753E-05	GPD2
0.578200378	1.492984608	4.32226E-19	8.06372E-17	FAH
0.577927823	1.492700067	0.004316259	0.035421628	FASTKD2
0.559107049	1.473357577	0.000202162	0.00311059	MDGA1
0.55722646	1.471436185	1.1959E-14	1.37298E-12	ALAD
0.554109609	1.468257254	0.00029225	0.004168615	DAGLB
0.549500843	1.463578649	1.22327E-11	1.04328E-09	FAAH
0.538534129	1.452495386	1.1323E-16	1.77891E-14	FAM162A
0.512021924	1.426047131	4.4155E-26	1.46447E-23	NEO1
0.490628053	1.405055785	6.77625E-24	1.68559E-21	DHCR24
0.488355717	1.40284492	3.53341E-05	0.000689362	PLCL1
0.484014621	1.398629974	2.24342E-13	2.16019E-11	EML1
0.483596711	1.398220979	4.64287E-06	0.000111394	IL6ST
0.479382539	1.394147045	1.48032E-16	2.20938E-14	EHD1
0.473022599	1.388012285	4.66881E-10	2.88921E-08	UGT1A8
0.472182608	1.387206316	4.23863E-12	3.83403E-10	GATM
0.470468076	1.385556504	1.77487E-15	2.1192E-13	RAP2B
0.466585649	1.381834195	1.75299E-11	1.37702E-09	MAN2A1
0.462878669	1.378289243	0.133944324	0.369181725	FABP7
0.454127413	1.369947378	7.42318E-07	2.3826E-05	ST3GAL4
0.453314838	1.369180692	4.01923E-08	1.71391E-06	CDH6
0.445306671	1.36160324	4.1593E-16	5.91214E-14	HSBP1

0.443755287	1.360139934	5.04784E-09	2.47013E-07	ACAT2
0.441099601	1.357632951	0.078609539	0.264841393	NID2
0.439546775	1.35617834	8.15034E-05	0.001431104	INPP4A
0.427276411	1.344692292	6.54285E-16	8.64437E-14	CPOX
0.426624575	1.344084912	3.72995E-21	7.95279E-19	PICALM
0.424121988	1.341816344	0.78381303	0.917467732	CKMT2
0.419489198	1.33745345	2.5698E-06	6.84897E-05	LDLR
0.409019514	1.327783084	1.27807E-11	1.05973E-09	IDH1
0.405209398	1.324277687	0.015463424	0.087541284	LDLRAP1
0.404429962	1.323562065	8.05827E-11	5.4668E-09	UBE2Z
0.393608333	1.313673977	1.00854E-06	3.07226E-05	MINDY1
0.393388961	1.313475122	9.65964E-09	4.50532E-07	TXN
0.392020255	1.312229271	2.16363E-13	2.15281E-11	SLC15A4
0.39131721	1.311590353	1.40344E-05	0.00030357	FABP5
0.389637223	1.310062857	1.33737E-06	3.99206E-05	SYT11
0.388833341	1.30932154	0.00144604	0.015526729	ELOVL6 LCE
0.386789877	1.307481061	2.47595E-12	2.3096E-10	TPPP
0.385824575	1.306606122	3.40885E-07	1.18319E-05	TRAPPC3
0.385355663	1.306181143	0.001783039	0.017741233	LRRN1
0.380911622	1.302164406	9.05763E-07	2.846E-05	DBI
0.376216876	1.297935689	0.002937535	0.026675752	MGAT1
0.375479457	1.297270363	0.000109398	0.00187675	AMPH
0.375216141	1.297033909	1.76072E-07	6.48858E-06	CDK18
0.368427312	1.290944763	0.006878132	0.048869714	REXO2
0.36843377	1.290932893	0.001865619	0.01823966	ATF2
0.364639837	1.287559978	2.37752E-09	1.27775E-07	UGT8
0.363900564	1.286881469	0.039865919	0.169999668	PIGL
0.362457185	1.285612828	6.70825E-08	2.71608E-06	FEM1B
0.360625816	1.28398219	0.009946605	0.063713765	PNP
0.359700967	1.283159893	5.53192E-07	1.81459E-05	FASN
0.352371461	1.276656849	2.64277E-05	0.000536644	PAK5
0.35148853	1.275870996	0.000958839	0.011093541	SHTN1
0.350618234	1.27509811	0.001297129	0.014131132	REEP4
0.349862439	1.274437659	4.52498E-09	2.25118E-07	UBL3
0.347405556	1.272270414	0.006388846	0.046400744	MOG
0.346313789	1.271310694	2.39712E-09	1.27775E-07	CHKA
0.338178144	1.264159022	0.000665556	0.008175634	AACS
0.337004002	1.263064211	0.008901826	0.058787505	KAZN
0.335819254	1.262094239	1.09943E-07	4.31815E-06	CTPS2
0.333630301	1.260180363	0.047150537	0.191380925	TPPP3
0.331030637	1.257911682	8.68412E-05	0.001507099	MARCKS
0.330711945	1.257633745	1.0411E-13	1.151E-11	REEP5
0.32927813	1.256383673	0.000195784	0.003043824	VAMP2
0.329184047	1.256302188	1.10398E-05	0.000253491	PCYT2
0.326673801	1.25411848	1.46996E-05	0.000315672	MAG
0.32659646	1.254041614	0.028951854	0.136526516	TXNIP

0.326124288	1.253637788	0.034593346	0.154121101	BTD
0.32566734	1.25324398	2.50588E-06	6.7388E-05	CASR
0.324309115	1.252064385	2.46812E-11	1.84183E-09	ADD1
0.322773094	1.250732509	0.05410914	0.208138895	MFN2
0.322310644	1.250331608	1.45989E-13	1.55635E-11	PTPN11
0.319333272	1.247753606	1.34753E-09	7.73532E-08	ALDOC
0.315661539	1.244584491	0.002844902	0.026049178	UBE2W
0.313857594	1.243023581	0.004355021	0.035421628	TRAPPC1
0.311717745	1.241186538	1.49958E-05	0.000319732	ATL1
0.310147168	1.239834472	6.14877E-05	0.001140004	ACOX1
0.308860644	1.238729129	1.82249E-05	0.000377787	PANX1
0.308190829	1.238130889	0.019509865	0.103994547	C1GALT1C1
0.306778763	1.236942975	7.52127E-05	0.001352443	SCARB2
0.304998548	1.235409011	0.026922256	0.13045931	ADAMTS1
0.304737216	1.235194119	6.66065E-16	8.64437E-14	BCAT1
0.302189461	1.233014159	1.24896E-05	0.000281687	ANXA2
0.29593861	1.227683182	2.53506E-08	1.12943E-06	CNDP2
0.294893575	1.226795176	2.48486E-05	0.000508035	TUBB3
0.293781007	1.225848756	0.001766198	0.017632442	PLP1
0.291908595	1.224258302	0.002097008	0.020192156	SNX15
0.291904211	1.224251297	4.38367E-06	0.000107256	PHLPP1
0.291854016	1.224212204	3.70152E-06	9.35624E-05	RAB4A
0.29038334	1.222965182	6.73334E-08	2.71608E-06	LDHA
0.289697571	1.222383826	0.010221071	0.065121464	TECR
0.286774691	1.219909787	3.15951E-07	1.10955E-05	SNAP29
0.28666785	1.219819448	4.80106E-07	1.61024E-05	ILK
0.286550577	1.219731693	0.00423034	0.035151926	MTM1
0.282061381	1.215930879	1.50891E-06	4.37291E-05	GPI
0.281422832	1.215392729	1.73979E-07	6.48858E-06	CSAD
0.280522277	1.214634965	0.036744838	0.161536587	HPDL
0.2792133	1.213532793	0.006602903	0.047723161	CLIC4
0.278612112	1.213012338	0.065942891	0.23489204	RIOX1 NO66
0.278552733	1.212973086	0.001564462	0.016443378	NAF1
0.277558405	1.212141158	4.03438E-07	1.38421E-05	ARHGEF2
0.276051903	1.21087507	1.44264E-07	5.52087E-06	MPP5
0.274948412	1.209950583	0.000193755	0.003036299	RAP1A
0.274275911	1.209386197	6.5334E-07	2.1198E-05	SOX10
0.272450231	1.207886452	0.001702529	0.017227287	ISCA1
0.271446422	1.207016947	0.000496642	0.006362564	MPP2
0.270187089	1.205963054	0.000966348	0.011137256	MFF
0.269836003	1.205656954	0.000267239	0.003835137	HDAC8
0.268168119	1.204272166	0.00123039	0.013502621	LHPP
0.26374451	1.200590523	0.008059223	0.054799042	RNPS1
0.263744512	1.200589524	4.91013E-07	1.62853E-05	CDK5
-0.26330581	-1.200213317	0.038636983	0.166093324	ERBB2
-0.263846892	-1.200677848	5.56824E-05	0.001045359	RIOX2

-0.268729474	-1.204746726	0.005644466	0.04244013	CADM2
-0.269090791	-1.205051291	0.091817583	0.294072408	ALDH1A2
-0.270704182	-1.20639611	0.00568582	0.042606917	AFAP1
-0.272476543	-1.207884029	0.009226375	0.060132596	FIP1L1
-0.272498245	-1.207897495	0.129867964	0.362973663	ARFIP1
-0.273319951	-1.208582387	0.000358613	0.004821896	GPR108
-0.273763402	-1.208952098	0.015484689	0.087541284	UHRF1
-0.275046348	-1.21003237	0.000124148	0.002070286	GPM6A
-0.277650487	-1.212218551	5.87918E-08	2.43741E-06	NUBP1
-0.27832414	-1.212785373	1.08578E-08	4.98624E-07	OSTF1
-0.278514037	-1.21294424	9.08206E-06	0.000210155	RAB31
-0.279562266	-1.213825332	0.000399699	0.005255954	LIG1
-0.279749388	-1.213984391	2.93182E-05	0.000587347	NAGA
-0.27988526	-1.214097225	0.004507612	0.0365631	GPR17
-0.280154409	-1.214319816	0.003447585	0.030090763	NR2F2
-0.285934565	-1.219182072	0.018557434	0.100169876	MPHOSPH8
-0.285959393	-1.219264976	0.102611595	0.313302654	KALRN HAPIP
-0.287670198	-1.22066647	1.92272E-07	6.99918E-06	CDC42BPB
-0.289076945	-1.221853113	0.001696579	0.017225469	PARD3
-0.289654403	-1.222593909	0.059212495	0.219837433	TDP1
-0.290185513	-1.222797754	3.12988E-06	8.19534E-05	SERINC5
-0.290343022	-1.22293104	0.026633847	0.130117894	PTPRZ1
-0.292984559	-1.225176148	0.002188813	0.020941049	MAP3K11
-0.294559312	-1.226508014	0.001170058	0.01298373	ATCAY
-0.296840355	-1.228449329	0.002754161	0.025314818	LXN
-0.29920111	-1.230461854	1.4028E-06	4.14591E-05	GRIA2
-0.299210014	-1.230510586	0.081718964	0.272166646	NRADD
-0.303066425	-1.233759212	0.007426306	0.051721911	RASSF2
-0.304096957	-1.234636412	0.007088831	0.049794722	PIP4P2
-0.304666402	-1.235141064	5.69327E-05	0.001062152	SH3GL2
-0.304683249	-1.235155431	0.139553166	0.378009255	POLD2
-0.306071309	-1.236336184	0.327946643	0.614513954	TMSB4X
-0.309450657	-1.239232334	3.47918E-08	1.50512E-06	NACC1
-0.31010215	-1.239792718	0.005695196	0.042606917	CDK1
-0.315091603	-1.24408724	8.21185E-05	0.001433472	PPP1CC
-0.315191272	-1.244176636	0.000437849	0.005633533	PC
-0.316843364	-1.245601645	2.76744E-10	1.75762E-08	TIMM8A
-0.317324005	-1.246032068	0.045643621	0.187666953	SLC6A11
-0.317861361	-1.246474884	2.17938E-06	5.9683E-05	RAPGEF2
-0.320312543	-1.248593647	0.065024173	0.23259768	LRRC4B
-0.322814934	-1.250772709	0.029893563	0.139207936	CDKN2AIP
-0.323764666	-1.251580097	0.004790777	0.037930873	ZKSCAN1
-0.325710314	-1.253281964	0.004831818	0.038014434	VMP1
-0.326946977	-1.254355911	4.15586E-11	2.95363E-09	NIT2
-0.329362712	-1.256449175	0.000175203	0.002811725	PIK3R2
-0.333066201	-1.259687859	8.07098E-06	0.000188218	PHYHIPL

-0.335142584	-1.261502	0.028598743	0.135935108	GLUL
-0.335549996	-1.261861093	0.35845782	0.642640596	SMIM7
-0.337023616	-1.263140732	0.000201349	0.00311059	TANC1
-0.345681156	-1.270749068	0.007855024	0.053532524	TSC22D1
-0.346936083	-1.271849883	0.027014574	0.130483017	HS3ST1
-0.350571625	-1.275063004	7.49525E-09	3.6086E-07	IRF2BPL
-0.354556097	-1.278590898	0.001406761	0.015159496	TLE4
-0.354762232	-1.278809616	0.010599335	0.066190407	COL11A1
-0.356245657	-1.280178104	0.007522833	0.052055345	PTK2B
-0.357672769	-1.281338624	0.000120416	0.002019331	TYMS
-0.360429633	-1.283802731	3.72996E-06	9.35624E-05	CNTFR
-0.3669264	-1.289596404	0.000356595	0.004816457	DCX
-0.368173852	-1.290717962	1.0435E-06	3.14631E-05	ASPA
-0.368295871	-1.29082755	9.13611E-11	6.06029E-09	CASK
-0.369134351	-1.291575832	8.02894E-09	3.80419E-07	LGMN
-0.371127321	-1.293364996	0.003259455	0.028956769	ABLIM2
-0.371563582	-1.293963932	0.087925657	0.28435329	SMPD3
-0.375991001	-1.297728278	1.00865E-06	3.07226E-05	PDLIM5
-0.378822249	-1.300279856	0.000854575	0.010042934	MPZL1
-0.379438776	-1.300834692	0.038925438	0.166703635	MRRF
-0.379946624	-1.301302648	7.07724E-05	0.001288144	CLU
-0.380798699	-1.302064734	0.000331021	0.004643034	DHTKD1
-0.382540652	-1.303633164	2.24194E-06	6.08382E-05	ZNF24
-0.385433737	-1.306252444	0.000111109	0.001884435	GFAP
-0.389446878	-1.309886665	0.129055273	0.361378979	ZFYVE21
-0.393335862	-1.313426775	0.006143313	0.045166965	ABAT
-0.394366619	-1.314364212	0.000177175	0.002828171	SMAD9
-0.399952963	-1.319490148	0.009183112	0.059981596	PLK1
-0.403421564	-1.322641251	1.77351E-05	0.000370205	ACSBG1
-0.407282479	-1.326186145	1.26352E-08	5.71455E-07	ACSL4
-0.408441757	-1.327310079	0.078771817	0.265088922	ZFYVE26
-0.420650653	-1.338539392	0.004239428	0.035151926	HAT1
-0.42067866	-1.338557122	1.70345E-11	1.37427E-09	POU3F3
-0.424867099	-1.342454596	0.0003734	0.004998198	RRM2
-0.426890129	-1.344334807	4.74276E-10	2.88921E-08	SLC1A1
-0.428583021	-1.345934445	0.004573633	0.036894149	GRN
-0.433376803	-1.350403993	0.001341102	0.014504312	CTU1
-0.438444141	-1.3551448	0.005156762	0.039950064	PLSCR3
-0.444660778	-1.360993838	9.0486E-12	7.94414E-10	OXCT1
-0.448447179	-1.36456929	3.38267E-08	1.48489E-06	ALCAM
-0.450254941	-1.366281892	5.4267E-06	0.000128561	PDGFRA
-0.46259039	-1.378014325	0.014025346	0.080978063	SORBS2
-0.471621838	-1.386666614	0.028584594	0.135935108	KRT27
-0.526575395	-1.440502144	1.06189E-15	1.32072E-13	SLC12A7
-0.537893801	-1.451851569	0.002305735	0.021989202	KPNA5
-0.552218579	-1.466338326	4.08176E-11	2.95363E-09	PDE1C

-0.578257947	-1.493044512	2.77546E-09	1.45346E-07	GPR37L1
-0.62866215	-1.546130444	0.034756301	0.154587818	MTARC2
-0.644280064	-1.562969573	2.07308E-05	0.000426768	CASKIN1
-0.669940201	-1.590998233	3.6658E-05	0.000710546	HDAC4
-0.712757203	-1.63893366	4.80929E-31	2.39262E-28	PADI2
-0.726841605	-1.655011644	2.90556E-09	1.49536E-07	HTRA1
-0.746862491	-1.678140882	2.52175E-10	1.6364E-08	SLC38A3
-0.857236531	-1.811555162	0.013606599	0.080133209	UBE2S
-1.010771486	-2.014987686	0.001211149	0.013340516	KRT72
-1.349108863	-2.547560427	0.050419456	0.199167224	NAPRT

XI. References

1. Allen, N. J. & Barres, B. A. Glia — more than just brain glue. *Nature* **457**, 675–677 (2009).
2. Cristobal, C. D. & Lee, H. K. Development of myelinating glia: An overview. *Glia* **70**, 2237–2259 (2022).
3. Preston, M. A. & Macklin, W. B. Zebrafish as a model to investigate CNS myelination. *Glia* **63**, 177–193 (2015).
4. Wu, Y., Dissing-Olesen, L., MacVicar, B. A. & Stevens, B. Microglia: Dynamic Mediators of Synapse Development and Plasticity. *Trends Immunol.* **36**, 605–613 (2015).
5. Lyons, D. A. & Talbot, W. S. Glial Cell Development and Function in Zebrafish. *Cold Spring Harb. Perspect. Biol.* **7**, a020586 (2015).
6. Godinho, L. Live Imaging of Zebrafish Development. *Cold Spring Harb. Protoc.* **2011**, pdb.top119 (2011).
7. Thyagarajan, T., Totey, S., Danton, M. J. S. & Kulkarni, A. B. Genetically Altered Mouse Models: the Good, the Bad, and the Ugly. *Crit. Rev. Oral Biol. Med.* **14**, 154–174 (2003).
8. McLellan, M. A., Rosenthal, N. A. & Pinto, A. R. Cre-loxP-Mediated Recombination: General Principles and Experimental Considerations. *Curr. Protoc. Mouse Biol.* **7**, 1–12 (2017).
9. Allen, N. J. & Lyons, D. A. Glia as Architects of Central Nervous System Formation and Function. *Science* **362**, 181–185 (2018).

10. Redmond, S. A. *et al*. Development of Ependymal and Postnatal Neural Stem Cells and Their Origin from a Common Embryonic Progenitor. *Cell Rep*. **27**, 429-441.e3 (2019).
11. Deng, S. *et al*. Roles of Ependymal Cells in the Physiology and Pathology of the Central Nervous System. *Aging Dis*. **14**, 468–483 (2023).
12. Del Bigio, M. R. The ependyma: A protective barrier between brain and cerebrospinal fluid. *Glia* **14**, 1–13 (1995).
13. Spassky, N. *et al*. Adult Ependymal Cells Are Postmitotic and Are Derived from Radial Glial Cells during Embryogenesis. *J. Neurosci.* **25**, 10–18 (2005).
14. Sarnat, H. B. Ependymal Reactions to Injury. A Review. *J. Neuropathol. Exp. Neurol*. **54**, 1–15 (1995).
15. Kyrousi, C. *et al*. Mcidas and GemC1 are key regulators for the generation of multiciliated ependymal cells in the adult neurogenic niche. *Development* **142**, 3661–3674 (2015).
16. Ogino, T. *et al*. Characterization of multiciliated ependymal cells that emerge in the neurogenic niche of the aged zebrafish brain. *J. Comp. Neurol*. **524**, 2982–2992 (2016).
17. Yang, Y. & Jackson, R. Astrocyte identity: evolutionary perspectives on astrocyte functions and heterogeneity. *Curr. Opin. Neurobiol*. **56**, 40–46 (2019).
18. Zhang, Y. & Barres, B. A. Astrocyte heterogeneity: an underappreciated topic in neurobiology. *Curr. Opin. Neurobiol*. **20**, 588–594 (2010).

19. Bocchi, R. *et al*. Astrocyte heterogeneity reveals region-specific astrogenesis in the white matter. *Nat. Neurosci.* **28**, 457–469 (2025).
20. Cahoy, J. D. *et al*. A transcriptome database for astrocytes, neurons, and oligodendrocytes: a new resource for understanding brain development and function. *J. Neurosci. Off. J. Soc. Neurosci.* **28**, 264–278 (2008).
21. Gross, R. E. *et al*. Bone morphogenetic proteins promote astroglial lineage commitment by mammalian subventricular zone progenitor cells. *Neuron* **17**, 595–606 (1996).
22. Freeman, M. R. Specification and Morphogenesis of Astrocytes. *Science* **330**, 774–778 (2010).
23. He, F. *et al*. A positive autoregulatory loop of Jak-STAT signaling controls the onset of astrogliogenesis. *Nat. Neurosci.* **8**, 616–625 (2005).
24. Bushong, E. A., Martone, M. E., Jones, Y. Z. & Ellisman, M. H. Protoplasmic Astrocytes in CA1 Stratum Radiatum Occupy Separate Anatomical Domains. *J. Neurosci.* **22**, 183–192 (2002).
25. Ogata, K. & Kosaka, T. Structural and quantitative analysis of astrocytes in the mouse hippocampus. *Neuroscience* **113**, 221–233 (2002).
26. Baldwin, K. T. *et al*. HepaCAM controls astrocyte self-organization and coupling. *Neuron* **109**, 2427-2442.e10 (2021).
27. Lovatt, D. *et al*. The Transcriptome and Metabolic Gene Signature of Protoplasmic Astrocytes in the Adult Murine Cortex. *J. Neurosci.* **27**, 12255–12266 (2007).

28. DeSilva, T. M., Borenstein, N. S., Volpe, J. J., Kinney, H. C. & Rosenberg, P. A. Expression of EAAT2 in neurons and protoplasmic astrocytes during human cortical development. *J. Comp. Neurol.* **520**, 3912–3932 (2012).
29. Lundgaard, I., Osório, M. J., Kress, B. T., Sanggaard, S. & Nedergaard, M. White matter astrocytes in health and disease. *Neuroscience* **276**, 161–173 (2014).
30. Seifert, G. *et al.* Analysis of Astroglial K+ Channel Expression in the Developing Hippocampus Reveals a Predominant Role of the Kir4.1 Subunit. *J. Neurosci.* **29**, 7474–7488 (2009).
31. Olsen, M. L. & Sontheimer, H. Functional implications for Kir4.1 channels in glial biology: from K+ buffering to cell differentiation. *J. Neurochem.* **107**, 589–601 (2008).
32. Tong, X. *et al.* Astrocyte Kir4.1 ion channel deficits contribute to neuronal dysfunction in Huntington's disease model mice. *Nat. Neurosci.* **17**, 694–703 (2014).
33. Suzuki, A. *et al.* Astrocyte-Neuron Lactate Transport Is Required for Long-Term Memory Formation. *Cell* **144**, 810–823 (2011).
34. Bonvento, G. & Bolaños, J. P. Astrocyte-neuron metabolic cooperation shapes brain activity. *Cell Metab.* **33**, 1546–1564 (2021).
35. Pellerin, L. & Magistretti, P. J. Glutamate uptake into astrocytes stimulates aerobic glycolysis: a mechanism coupling neuronal activity to glucose utilization. *Proc. Natl. Acad. Sci. U. S. A.* **91**, 10625–10629 (1994).

36. Abbott, N. J. Astrocyte–endothelial interactions and blood–brain barrier permeability. *J. Anat.* **200**, 523–534 (2002).

37. Armulik, A. *et al.* Pericytes regulate the blood–brain barrier. *Nature* **468**, 557–561 (2010).

38. Haj-Yasein, N. N. *et al.* Glial-conditional deletion of aquaporin-4 (Aqp4) reduces blood–brain water uptake and confers barrier function on perivascular astrocyte endfeet. *Proc. Natl. Acad. Sci.* **108**, 17815–17820 (2011).

39. Ezan, P. *et al.* Deletion of astroglial connexins weakens the blood-brain barrier. *J. Cereb. Blood Flow Metab. Off. J. Int. Soc. Cereb. Blood Flow Metab.* **32**, 1457–1467 (2012).

40. Nicchia, G. P. *et al.* The role of aquaporin-4 in the blood-brain barrier development and integrity: studies in animal and cell culture models. *Neuroscience* **129**, 935–945 (2004).

41. Singh, S. K. *et al.* Astrocytes Assemble Thalamocortical Synapses by Bridging NRX1α and NL1 via Hevin. *Cell* **164**, 183–196 (2016).

42. Kucukdereli, H. *et al.* Control of excitatory CNS synaptogenesis by astrocyte-secreted proteins Hevin and SPARC. *Proc. Natl. Acad. Sci.* **108**, E440–E449 (2011).

43. Navarrete, M. *et al.* Astrocytes Mediate In Vivo Cholinergic-Induced Synaptic Plasticity. *PLOS Biol.* **10**, e1001259 (2012).

44. Ota, Y., Zanetti, A. T. & Hallock, R. M. The Role of Astrocytes in the Regulation of Synaptic Plasticity and Memory Formation. *Neural Plast.* **2013**, 185463 (2013).

45. Liberto, C. M., Albrecht, P. J., Herx, L. M., Yong, V. W. & Levison, S. W. Pro-regenerative properties of cytokine-activated astrocytes. *J. Neurochem.* **89**, 1092–1100 (2004).

46. Lee, S. C., Liu, W., Dickson, D. W., Brosnan, C. F. & Berman, J. W. Cytokine production by human fetal microglia and astrocytes. Differential induction by lipopolysaccharide and IL-1 beta. *J. Immunol.* **150**, 2659–2667 (1993).

47. Dong, Y. & Benveniste, E. N. Immune function of astrocytes. *Glia* **36**, 180–190 (2001).

48. Chen, J., Poskanzer, K. E., Freeman, M. R. & Monk, K. R. Live-imaging of astrocyte morphogenesis and function in zebrafish neural circuits. *Nat. Neurosci.* **23**, 1297–1306 (2020).

49. Scheib, J. & Byrd-Jacobs, C. Zebrafish Astroglial Morphology in the Olfactory Bulb Is Altered With Repetitive Peripheral Damage. *Front. Neuroanat.* **14**, (2020).

50. Stork, T., Sheehan, A., Tasdemir-Yilmaz, O. E. & Freeman, M. R. Neuron-Glia Interactions through the Heartless FGF Receptor Signaling Pathway Mediate Morphogenesis of Drosophila Astrocytes. *Neuron* **83**, 388–403 (2014).

51. Rival, T. *et al.* Decreasing Glutamate Buffering Capacity Triggers Oxidative Stress and Neuropil Degeneration in the Drosophila Brain. *Curr. Biol.* **14**, 599–605 (2004).

52. Alliot, F., Godin, I. & Pessac, B. Microglia derive from progenitors, originating from the yolk sac, and which proliferate in the brain. *Dev. Brain Res.* **117**, 145–152 (1999).

53. Kierdorf, K. *et al.* Microglia emerge from erythromyeloid precursors via Pu.1- and Irf8-dependent pathways. *Nat. Neurosci.* **16**, 273–280 (2013).

54. Lawson, L. J., Perry, V. H., Dri, P. & Gordon, S. Heterogeneity in the distribution and morphology of microglia in the normal adult mouse brain. *Neuroscience* **39**, 151–170 (1990).

55. Nimmerjahn, A., Kirchhoff, F. & Helmchen, F. Resting microglial cells are highly dynamic surveillants of brain parenchyma in vivo. *Science* **308**, 1314–1318 (2005).

56. Fonseca, M. I. *et al.* Cell-specific deletion of C1qa identifies microglia as the dominant source of C1q in mouse brain. *J. Neuroinflammation* **14**, 48 (2017).

57. Schafer, D. P. *et al.* Microglia Sculpt Postnatal Neural Circuits in an Activity and Complement-Dependent Manner. *Neuron* **74**, 691–705 (2012).

58. Jurga, A. M., Paleczna, M. & Kuter, K. Z. Overview of General and Discriminating Markers of Differential Microglia Phenotypes. *Front. Cell. Neurosci.* **14**, (2020).

59. Holtman, I. R., Skola, D. & Glass, C. K. Transcriptional control of microglia phenotypes in health and disease. *J. Clin. Invest.* **127**, 3220–3229 (2017).

60. Lynch, M. A. The Multifaceted Profile of Activated Microglia. *Mol. Neurobiol.* **40**, 139–156 (2009).

61. Smith, J. A., Das, A., Ray, S. K. & Banik, N. L. Role of pro-inflammatory cytokines released from microglia in neurodegenerative diseases. *Brain Res. Bull.* **87**, 10–20 (2012).

62. Clearance of apoptotic neurons without inflammation by microglial triggering receptor expressed on myeloid cells-2 | Journal of Experimental Medicine | Rockefeller University Press. https://rupress.org/jem/article/201/4/647/52887/Clearance-of-apoptotic-neurons-without.
63. Sierra, A. *et al*. Microglia Shape Adult Hippocampal Neurogenesis through Apoptosis-Coupled Phagocytosis. *Cell Stem Cell* **7**, 483–495 (2010).
64. Stalder, M. *et al*. Association of Microglia with Amyloid Plaques in Brains of APP23 Transgenic Mice. *Am. J. Pathol.* **154**, 1673–1684 (1999).
65. Condello, C., Yuan, P., Schain, A. & Grutzendler, J. Microglia constitute a barrier that prevents neurotoxic protofibrillar Aβ42 hotspots around plaques. *Nat. Commun.* **6**, 6176 (2015).
66. McNamara, N. B. *et al*. Microglia regulate central nervous system myelin growth and integrity. *Nature* **613**, 120–129 (2023).
67. Frontiers | Phagocytosis in the Brain: Homeostasis and Disease. https://www.frontiersin.org/journals/immunology/articles/10.3389/fimmu.2019.00790/full.
68. Casano, A. M., Albert, M. & Peri, F. Developmental Apoptosis Mediates Entry and Positioning of Microglia in the Zebrafish Brain. *Cell Rep.* **16**, 897–906 (2016).
69. Mazzolini, J. *et al*. Gene expression profiling reveals a conserved microglia signature in larval zebrafish. *Glia* **68**, 298–315 (2020).

70. Nishiyama, A., Watanabe, M., Yang, Z. & Bu, J. Identity, distribution, and development of polydendrocytes: NG2-expressing glial cells. *J. Neurocytol.* **31**, 437 ppl= – 455 (2002).

71. Zhou, Q., Choi, G. & Anderson, D. J. The bHLH Transcription Factor Olig2 Promotes Oligodendrocyte Differentiation in Collaboration with Nkx2.2. *Neuron* **31**, 791–807 (2001).

72. Kessaris, N. *et al.* Competing waves of oligodendrocytes in the forebrain and postnatal elimination of an embryonic lineage. *Nat. Neurosci.* **9**, 173–179 (2006).

73. Foerster, S. *et al.* Developmental origin of oligodendrocytes determines their function in the adult brain. *Nat. Neurosci.* **27**, 1545–1554 (2024).

74. Buchanan, J. *et al.* Oligodendrocyte precursor cells ingest axons in the mouse neocortex. *Proc. Natl. Acad. Sci.* **119**, e2202580119 (2022).

75. Ms, Y. *et al.* Dynamics of oligodendrocyte generation and myelination in the human brain. *Cell* **159**, (2014).

76. Fancy, S. P. J. *et al.* Overcoming remyelination failure in multiple sclerosis and other myelin disorders. *Exp. Neurol.* **225**, 18–23 (2010).

77. Li, J., Miramontes, T. G., Czopka, T. & Monk, K. R. Synaptic input and Ca2+ activity in zebrafish oligodendrocyte precursor cells contribute to myelin sheath formation. *Nat. Neurosci.* **27**, 219–231 (2024).

78. Bergles, D. E., Roberts, J. D., Somogyi, P. & Jahr, C. E. Glutamatergic synapses on oligodendrocyte precursor cells in the hippocampus. *Nature* **405**, 187–191 (2000).

79. Lin, S. & Bergles, D. E. Synaptic signaling between GABAergic interneurons and oligodendrocyte precursor cells in the hippocampus. *Nat. Neurosci.* **7**, 24–32 (2004).

80. Gibson, E. M. *et al.* Neuronal activity promotes oligodendrogenesis and adaptive myelination in the mammalian brain. *Science* **344**, 1252304 (2014).

81. Hines, J. H., Ravanelli, A. M., Schwindt, R., Scott, E. K. & Appel, B. Neuronal activity biases axon selection for myelination in vivo. *Nat. Neurosci.* **18**, 683–689 (2015).

82. Mitew, S. *et al.* Pharmacogenetic stimulation of neuronal activity increases myelination in an axon-specific manner. *Nat. Commun.* **9**, 306 (2018).

83. Kirby, L. *et al.* Oligodendrocyte precursor cells present antigen and are cytotoxic targets in inflammatory demyelination. *Nat. Commun.* **10**, 3887 (2019).

84. Auguste, Y. S. S. *et al.* Oligodendrocyte precursor cells engulf synapses during circuit remodeling in mice. *Nat. Neurosci.* **25**, 1273–1278 (2022).

85. Buchanan, J., da Costa, N. M. & Cheadle, L. Emerging roles of oligodendrocyte precursor cells in neural circuit development and remodeling. *Trends Neurosci.* **46**, 628–639 (2023).

86. Park, H.-C., Boyce, J., Shin, J. & Appel, B. Oligodendrocyte Specification in Zebrafish Requires Notch-Regulated Cyclin-Dependent Kinase Inhibitor Function. *J. Neurosci.* **25**, 6836–6844 (2005).

87. Zannino, D. A. & Appel, B. Olig2+ Precursors Produce Abducens Motor Neurons and Oligodendrocytes in the Zebrafish Hindbrain. *J. Neurosci.* **29**, 2322–2333 (2009).

88. Neely, S. A. & Lyons, D. A. Insights Into Central Nervous System Glial Cell Formation and Function From Zebrafish. *Front. Cell Dev. Biol.* **9**, 754606 (2021).

89. Kucenas, S., Snell, H. & Appel, B. nkx2.2a promotes specification and differentiation of a myelinating subset of oligodendrocyte lineage cells in zebrafish. *Neuron Glia Biol.* **4**, 71–81 (2008).

90. Wang, S. *et al.* Notch receptor activation inhibits oligodendrocyte differentiation. *Neuron* **21**, 63–75 (1998).

91. Elbaz, B. & Popko, B. Molecular Control of Oligodendrocyte Development. *Trends Neurosci.* **42**, 263–277 (2019).

92. Emery, B. & Wood, T. L. Regulators of Oligodendrocyte Differentiation. *Cold Spring Harb. Perspect. Biol.* **16**, a041358 (2024).

93. Saher, G. *et al.* High cholesterol level is essential for myelin membrane growth. *Nat. Neurosci.* **8**, 468–475 (2005).

94. Snaidero, N. *et al.* Myelin Membrane Wrapping of CNS Axons by PI(3,4,5)P3-Dependent Polarized Growth at the Inner Tongue. *Cell* **156**, 277–290 (2014).

95. Nawaz, S. *et al.* Actin filament turnover drives leading edge growth during myelin sheath formation in the central nervous system. *Dev. Cell* **34**, 139–151 (2015).

96. Zuchero, J. B. *et al.* CNS Myelin Wrapping Is Driven by Actin Disassembly. *Dev. Cell* **34**, 152–167 (2015).

97. Ritchie, J. M. Physiological Basis of Conduction in Myelinated Nerve Fibers. in *Myelin* (ed. Morell, P.) 117–145 (Springer US, Boston, MA, 1984). doi:10.1007/978-1-4757-1830-0_4.

98. Huxley, A. F. & Stämpfli, R. Direct determination of membrane resting potential and action potential in single myelinated nerve fibres. *J. Physiol.* **112**, 476–495 (1951).

99. Griffiths, I. *et al.* Axonal Swellings and Degeneration in Mice Lacking the Major Proteolipid of Myelin. *Science* **280**, 1610–1613 (1998).

100. Kassmann, C. M. *et al.* Axonal loss and neuroinflammation caused by peroxisome-deficient oligodendrocytes. *Nat. Genet.* **39**, 969–976 (2007).

101. Lappe-Siefke, C. *et al.* Disruption of Cnp1 uncouples oligodendroglial functions in axonal support and myelination. *Nat. Genet.* **33**, 366–374 (2003).

102. Nave, K.-A. & Trapp, B. D. Axon-Glial Signaling and the Glial Support of Axon Function. *Annu. Rev. Neurosci.* **31**, 535–561 (2008).

103. Lee, Y. *et al.* Oligodendroglia metabolically support axons and contribute to neurodegeneration. *Nature* **487**, 443–448 (2012).

104. Saab, A. S. *et al.* Oligodendroglial NMDA Receptors Regulate Glucose Import and Axonal Energy Metabolism. *Neuron* **91**, 119–132 (2016).

105. Looser, Z. J. *et al.* Oligodendrocyte–axon metabolic coupling is mediated by extracellular K+ and maintains axonal health. *Nat. Neurosci.* **27**, 433–448 (2024).

106. Sherafat, A., Pfeiffer, F. & Nishiyama, A. Shaping of Regional Differences in Oligodendrocyte Dynamics by Regional Heterogeneity of the Pericellular Microenvironment. *Front. Cell. Neurosci.* **15**, (2021).

107. Hughes, E. G., Orthmann-Murphy, J. L., Langseth, A. J. & Bergles, D. E. Myelin remodeling through experience-dependent oligodendrogenesis in the adult somatosensory cortex. *Nat. Neurosci.* **21**, 696–706 (2018).

108. McKenzie, I. A. *et al.* Motor skill learning requires active central myelination. *Science* **346**, 318–322 (2014).

109. Hill, R. A., Li, A. M. & Grutzendler, J. Lifelong cortical myelin plasticity and age-related degeneration in the live mammalian brain. *Nat. Neurosci.* **21**, 683–695 (2018).

110. Steadman, P. E. *et al.* Disruption of Oligodendrogenesis Impairs Memory Consolidation in Adult Mice. *Neuron* **105**, 150-164.e6 (2020).

111. Kaller, M. S., Lazari, A., Blanco-Duque, C., Sampaio-Baptista, C. & Johansen-Berg, H. Myelin plasticity and behaviour-connecting the dots. *Curr. Opin. Neurobiol.* **47**, 86–92 (2017).

112. Perlman, S. J. & Mar, S. Leukodystrophies. in *Neurodegenerative Diseases* (ed. Ahmad, S. I.) 154–171 (Springer US, New York, NY, 2012). doi:10.1007/978-1-4614-0653-2_13.

113. Knowles, J. K. *et al.* Maladaptive myelination promotes generalized epilepsy progression. *Nat. Neurosci.* **25**, 596–606 (2022).

114. Chau Loo Kung, G. *et al*. Quantitative MRI reveals widespread, network-specific myelination change during generalized epilepsy progression. *NeuroImage* **280**, 120312 (2023).

115. Takahashi, N., Sakurai, T., Davis, K. L. & Buxbaum, J. D. Linking oligodendrocyte and myelin dysfunction to neurocircuitry abnormalities in schizophrenia. *Prog. Neurobiol.* **93**, 13–24 (2011).

116. Valdés-Tovar, M. *et al*. Insights into myelin dysfunction in schizophrenia and bipolar disorder. *World J. Psychiatry* **12**, 264–285 (2022).

117. Breton, J. M. *et al*. Juvenile exposure to acute traumatic stress leads to long-lasting alterations in grey matter myelination in adult female but not male rats. *Neurobiol. Stress* **14**, 100319 (2021).

118. Cai, J. *et al*. Generation of Oligodendrocyte Precursor Cells from Mouse Dorsal Spinal Cord Independent of *Nkx6* Regulation and *Shh* Signaling. *Neuron* **45**, 41–53 (2005).

119. Fogarty, M., Richardson, W. D. & Kessaris, N. A subset of oligodendrocytes generated from radial glia in the dorsal spinal cord. *Development* **132**, 1951–1959 (2005).

120. Vallstedt, A., Klos, J. M. & Ericson, J. Multiple Dorsoventral Origins of Oligodendrocyte Generation in the Spinal Cord and Hindbrain. *Neuron* **45**, 55–67 (2005).

121. Pringle, N. P. & Richardson, W. D. A singularity of PDGF alpha-receptor expression in the dorsoventral axis of the neural tube may define the origin of the oligodendrocyte lineage. *Development* **117**, 525–533 (1993).

122. Rivers, L. E. *et al*. PDGFRA/NG2 glia generate myelinating oligodendrocytes and piriform projection neurons in adult mice. *Nat. Neurosci.* **11**, 1392–1401 (2008).

123. Tripathi, R. B. *et al*. Dorsally and ventrally derived oligodendrocytes have similar electrical properties but myelinate preferred tracts. *J. Neurosci. Off. J. Soc. Neurosci.* **31**, 6809–6819 (2011).

124. Bergles, D. E. & Richardson, W. D. Oligodendrocyte Development and Plasticity. *Cold Spring Harb. Perspect. Biol.* **8**, a020453 (2016).

125. Boshans, L. L., Sherafat, A. & Nishiyama, A. The effects of developmental and current niches on oligodendrocyte precursor dynamics and fate. *Neurosci. Lett.* **715**, 134593 (2020).

126. Boulanger, J. J. & Messier, C. Unbiased stereological analysis of the fate of oligodendrocyte progenitor cells in the adult mouse brain and effect of reference memory training. *Behav. Brain Res.* **329**, 127–139 (2017).

127. Hill, R. A., Patel, K. D., Medved, J., Reiss, A. M. & Nishiyama, A. NG2 Cells in White Matter But Not Gray Matter Proliferate in Response to PDGF. *J. Neurosci.* **33**, 14558–14566 (2013).

128. Zhu, X., Bergles, D. E. & Nishiyama, A. NG2 cells generate both oligodendrocytes and gray matter astrocytes. *Development* **135**, 145–157 (2008).

129. Barres, B. A. *et al.* Cell death and control of cell survival in the oligodendrocyte lineage. *Cell* **70**, 31–46 (1992).

130. Hughes, E. G. & Stockton, M. E. Premyelinating Oligodendrocytes: Mechanisms Underlying Cell Survival and Integration. *Front. Cell Dev. Biol.* **9**, (2021).

131. Almeida, R. G., Czopka, T., ffrench-Constant, C. & Lyons, D. A. Individual axons regulate the myelinating potential of single oligodendrocytes in vivo. *Development* **138**, 4443–4450 (2011).

132. Lam, M. *et al.* CNS myelination requires VAMP2/3-mediated membrane expansion in oligodendrocytes. *Nat. Commun.* **13**, 5583 (2022).

133. Tripathi, R. B. *et al.* Remarkable Stability of Myelinating Oligodendrocytes in Mice. *Cell Rep.* **21**, 316–323 (2017).

134. Karttunen, M. J., Czopka, T., Goedhart, M., Early, J. J. & Lyons, D. A. Regeneration of myelin sheaths of normal length and thickness in the zebrafish CNS correlates with growth of axons in caliber. *PLOS ONE* **12**, e0178058 (2017).

135. Czopka, T., ffrench-Constant, C. & Lyons, D. A. Individual Oligodendrocytes Have Only a Few Hours in which to Generate New Myelin Sheaths In Vivo. *Dev. Cell* **25**, 599–609 (2013).

136. Almeida, R. G. *et al.* Myelination of Neuronal Cell Bodies when Myelin Supply Exceeds Axonal Demand. *Curr. Biol.* **28**, 1296-1305.e5 (2018).

137. Call, C. L. & Bergles, D. E. Cortical neurons exhibit diverse myelination patterns that scale between mouse brain regions and regenerate after demyelination. *Nat. Commun.* **12**, 4767 (2021).

138. Redmond, S. A. *et al.* Somatodendritic Expression of JAM2 Inhibits Oligodendrocyte Myelination. *Neuron* **91**, 824–836 (2016).

139. Almeida, R. G. The Rules of Attraction in Central Nervous System Myelination. *Front. Cell. Neurosci.* **12**, (2018).

140. Lee, S. *et al.* A culture system to study oligodendrocyte myelination-processes using engineered nanofibers. *Nat. Methods* **9**, 917–922 (2012).

141. Marques, S. *et al.* Transcriptional Convergence of Oligodendrocyte Lineage Progenitors during Development. *Dev. Cell* **46**, 504-517.e7 (2018).

142. Baaklini, C. S. *et al.* Microglia promote remyelination independent of their role in clearing myelin debris. *Cell Rep.* **42**, 113574 (2023).

143. Hughes, E. G., Kang, S. H., Fukaya, M. & Bergles, D. E. Oligodendrocyte progenitors balance growth with self-repulsion to achieve homeostasis in the adult brain. *Nat. Neurosci.* **16**, 668–676 (2013).

144. Bacmeister, C. M. *et al.* Motor learning promotes remyelination via new and surviving oligodendrocytes. *Nat. Neurosci.* **23**, 819–831 (2020).

145. Buscham, T. J., Eichel, M. A., Siems, S. B. & Werner, H. B. Turning to myelin turnover. *Neural Regen. Res.* **14**, 2063–2066 (2019).

146. Groteklaes, A., Bönisch, C., Eiberger, B., Christ, A. & Schilling, K. Developmental Maturation of the Cerebellar White Matter—an Instructive

Environment for Cerebellar Inhibitory Interneurons. *The Cerebellum* **19**, 286–308 (2020).

147. Yeung, M. S. Y. *et al*. Oligodendrocyte generation dynamics in multiple sclerosis. *Nature* **566**, 538–542 (2019).

148. Attfield, K. E., Jensen, L. T., Kaufmann, M., Friese, M. A. & Fugger, L. The immunology of multiple sclerosis. *Nat. Rev. Immunol.* **22**, 734–750 (2022).

149. Mezydlo, A. *et al*. Remyelination by surviving oligodendrocytes is inefficient in the inflamed mammalian cortex. *Neuron* **111**, 1748-1759.e8 (2023).

150. Aprato, J. *et al*. Myrf guides target gene selection of transcription factor Sox10 during oligodendroglial development. *Nucleic Acids Res*. **48**, 1254–1270 (2020).

151. Emery, B. *et al*. Myelin Gene Regulatory Factor Is a Critical Transcriptional Regulator Required for CNS Myelination. *Cell* **138**, 172–185 (2009).

152. Napoli, I. *et al*. A Central Role for the ERK-Signaling Pathway in Controlling Schwann Cell Plasticity and Peripheral Nerve Regeneration In Vivo. *Neuron* **73**, 729–742 (2012).

153. Ishii, A., Fyffe-Maricich, S. L., Furusho, M., Miller, R. H. & Bansal, R. ERK1/ERK2 MAPK Signaling is Required to Increase Myelin Thickness Independent of Oligodendrocyte Differentiation and Initiation of Myelination. *J. Neurosci.* **32**, 8855–8864 (2012).

154. Fedder-Semmes, K. N. & Appel, B. The Akt-mTOR Pathway Drives Myelin Sheath Growth by Regulating Cap-Dependent Translation. *J. Neurosci.* **41**, 8532–8544 (2021).

155. Jeffries, M. A. *et al*. mTOR Signaling Regulates Metabolic Function in Oligodendrocyte Precursor Cells and Promotes Efficient Brain Remyelination in the Cuprizone Model. *J. Neurosci. Off. J. Soc. Neurosci.* **41**, 8321–8337 (2021).

156. Brown, T. L. & Macklin, W. B. The actin cytoskeleton in myelinating cells. *Neurochem. Res.* 10.1007/s11064-019-02753–0 (2019) doi:10.1007/s11064-019-02753-0.

157. Aggarwal, S. *et al*. Myelin membrane assembly is driven by a phase transition of myelin basic proteins into a cohesive protein meshwork. *PLoS Biol.* **11**, e1001577 (2013).

158. Dimas, P. *et al*. CNS myelination and remyelination depend on fatty acid synthesis by oligodendrocytes. *eLife* **8**, e44702.

159. Teo, J. D. *et al*. Early microglial response, myelin deterioration and lethality in mice deficient for very long chain ceramide synthesis in oligodendrocytes. *Glia* **71**, 1120–1141 (2023).

160. Sabri, M. I., Bone, A. H. & Davison, A. N. Turnover of myelin and other structural proteins in the developing rat brain. *Biochem. J.* **142**, 499–507 (1974).

161. Hornig, J. *et al*. The Transcription Factors Sox10 and Myrf Define an Essential Regulatory Network Module in Differentiating Oligodendrocytes. *PLOS Genet.* **9**, e1003907 (2013).

162. Xiao, G. *et al*. Differential Inhibition of Sox10 Functions by Notch-Hes Pathway. *Cell. Mol. Neurobiol.* **40**, 653–662 (2020).

163. Koenning, M. *et al*. Myelin Gene Regulatory Factor Is Required for Maintenance of Myelin and Mature Oligodendrocyte Identity in the Adult CNS. *J. Neurosci*. **32**, 12528–12542 (2012).

164. Li, Z., Park, Y. & Marcotte, E. M. A Bacteriophage Tailspike Domain Promotes Self-Cleavage of a Human Membrane-Bound Transcription Factor, the Myelin Regulatory Factor MYRF. *PLOS Biol*. **11**, e1001624 (2013).

165. Huang, H. *et al*. Interactive Repression of MYRF Self-Cleavage and Activity in Oligodendrocyte Differentiation by TMEM98 Protein. *J. Neurosci*. **38**, 9829–9839 (2018).

166. Bujalka, H. *et al*. MYRF Is a Membrane-Associated Transcription Factor That Autoproteolytically Cleaves to Directly Activate Myelin Genes. *PLOS Biol*. **11**, e1001625 (2013).

167. Calonga-Solís, V. *et al*. MYRF: A New Regulator of Cardiac and Early Gonadal Development-Insights from Single Cell RNA Sequencing Analysis. *J. Clin. Med*. **11**, 4858 (2022).

168. Garnai, S. J. *et al*. Variants in myelin regulatory factor (MYRF) cause autosomal dominant and syndromic nanophthalmos in humans and retinal degeneration in mice. *PLOS Genet*. **15**, e1008130 (2019).

169. Wang, H. *et al*. Case Report: De novo variant in myelin regulatory factor in a Chinese child with 46,XY disorder/difference of sex development, cardiac and urogenital anomalies, and short stature. *Front. Pediatr*. **10**, (2022).

170. Duncan, G. J. *et al*. Remyelination protects neurons from DLK-mediated neurodegeneration. *Nat. Commun*. **15**, 9148 (2024).

171. Chung, S.-H., Guo, F., Jiang, P., Pleasure, D. E. & Deng, W. Olig2/Plp-positive progenitor cells give rise to Bergmann glia in the cerebellum. *Cell Death Dis*. **4**, e546 (2013).

172. Makinodan, M., Rosen, K. M., Ito, S. & Corfas, G. A critical period for social experience-dependent oligodendrocyte maturation and myelination. *Science* **337**, 1357–1360 (2012).

173. Fletcher, J. L., Makowiecki, K., Cullen, C. L. & Young, K. M. Oligodendrogenesis and myelination regulate cortical development, plasticity and circuit function. *Semin. Cell Dev. Biol*. **118**, 14–23 (2021).

174. López-Juárez, A. *et al*. Oligodendrocyte Nf1 Controls Aberrant Notch Activation and Regulates Myelin Structure and Behavior. *Cell Rep*. **19**, 545–557 (2017).

175. Zhang, Y. *et al*. Notch1 signaling plays a role in regulating precursor differentiation during CNS remyelination. *Proc. Natl. Acad. Sci. U. S. A*. **106**, 19162–19167 (2009).

176. Stidworthy, M. F. *et al*. Notch1 and Jagged1 are expressed after CNS demyelination, but are not a major rate-determining factor during remyelination. *Brain J. Neurol*. **127**, 1928–1941 (2004).

177. Nonneman, A. *et al*. Astrocyte-derived Jagged-1 mitigates deleterious Notch signaling in amyotrophic lateral sclerosis. *Neurobiol. Dis*. **119**, 26–40 (2018).

178. Givogri, M. I. *et al.* Central nervous system myelination in mice with deficient expression of Notch1 receptor. *J. Neurosci. Res.* **67**, 309–320 (2002).

179. Kageyama, R., Shimojo, H. & Imayoshi, I. Dynamic expression and roles of Hes factors in neural development. *Cell Tissue Res.* **359**, 125–133 (2015).

180. Figlia, G., Gerber, D. & Suter, U. Myelination and mTOR. *Glia* **66**, 693–707 (2018).

181. Ben-Sahra, I. & Manning, B. D. mTORC1 signaling and the metabolic control of cell growth. *Curr. Opin. Cell Biol.* **45**, 72–82 (2017).

182. Szwed, A., Kim, E. & Jacinto, E. Regulation and metabolic functions of mTORC1 and mTORC2. *Physiol. Rev.* **101**, 1371–1426 (2021).

183. Lebrun-Julien, F. *et al.* Balanced mTORC1 Activity in Oligodendrocytes Is Required for Accurate CNS Myelination. *J. Neurosci.* **34**, 8432–8448 (2014).

184. Bercury, K. K. *et al.* Conditional Ablation of Raptor or Rictor Has Differential Impact on Oligodendrocyte Differentiation and CNS Myelination. *J. Neurosci.* **34**, 4466–4480 (2014).

185. Furusho, M., Ishii, A. & Bansal, R. Signaling by FGF Receptor 2, Not FGF Receptor 1, Regulates Myelin Thickness through Activation of ERK1/2–MAPK, Which Promotes mTORC1 Activity in an Akt-Independent Manner. *J. Neurosci.* **37**, 2931–2946 (2017).

186. Maruyama, I. N. Mechanisms of Activation of Receptor Tyrosine Kinases: Monomers or Dimers. *Cells* **3**, 304–330 (2014).

187. Li, L. *et al*. The Ras/Raf/MEK/ERK signaling pathway and its role in the occurrence and development of HCC. *Oncol. Lett.* **12**, 3045–3050 (2016).

188. Yang, C. *et al*. Actin polymerization promotes invagination of flat clathrin-coated lattices in mammalian cells by pushing at lattice edges. *Nat. Commun.* **13**, 6127 (2022).

189. Blanchoin, L., Pollard, T. D. & Mullins, R. D. Interactions of ADF/cofilin, Arp2/3 complex, capping protein and profilin in remodeling of branched actin filament networks. *Curr. Biol.* **10**, 1273–1282 (2000).

190. Svitkina, T. M. & Borisy, G. G. Arp2/3 Complex and Actin Depolymerizing Factor/Cofilin in Dendritic Organization and Treadmilling of Actin Filament Array in Lamellipodia. *J. Cell Biol.* **145**, 1009–1026 (1999).

191. Southwick, F. S. Gelsolin and ADF/cofilin enhance the actin dynamics of motile cells. *Proc. Natl. Acad. Sci.* **97**, 6936–6938 (2000).

192. Fu, M. *et al*. The Golgi Outpost Protein TPPP Nucleates Microtubules and Is Critical for Myelination. *Cell* **179**, 132-146.e14 (2019).

193. Roll-Mecak, A. A Microtubule-Myelination Connection. *Cell* **179**, 54–56 (2019).

194. Carson, J. H., Worboys, K., Ainger, K. & Barbarese, E. Translocation of myelin basic protein mRNA in oligodendrocytes requires microtubules and kinesin. *Cell Motil. Cytoskeleton* **38**, 318–328 (1997).

195. Herbert, A. L. *et al*. Dynein/dynactin is necessary for anterograde transport of Mbp mRNA in oligodendrocytes and for myelination in vivo. *Proc. Natl. Acad. Sci. U. S. A.* **114**, E9153–E9162 (2017).

196. Bullock, T. H., Moore, J. K. & Fields, R. D. Evolution of myelin sheaths: both lamprey and hagfish lack myelin. *Neurosci. Lett.* **48**, 145–148 (1984).

197. Martini, R., Groh, J. & Bartsch, U. Comparative biology of Schwann cells and oligodendrocytes. in *The Biology of Oligodendrocytes* (eds. Mathey, E. & Armati, P.) 19–48 (Cambridge University Press, Cambridge, 2010). doi:10.1017/CBO9780511782121.003.

198. Zalc, B. The acquisition of myelin: An evolutionary perspective. *Brain Res.* **1641**, 4–10 (2016).

199. Hughes, E. G. & Appel, B. The cell biology of CNS myelination. *Curr. Opin. Neurobiol.* **39**, 93–100 (2016).

200. Bunge, M. B., Williams, A. K. & Wood, P. M. Neuron-schwann cell interaction in basal lamina formation. *Dev. Biol.* **92**, 449–460 (1982).

201. Linkage Between Axonal Ensheathment and Basal Lamina Production by Schwann Cells | Annual Reviews. https://www.annualreviews.org/content/journals/10.1146/annurev.ne.09.030186.001513.

202. Boerboom, A., Dion, V., Chariot, A. & Franzen, R. Molecular Mechanisms Involved in Schwann Cell Plasticity. *Front. Mol. Neurosci.* **10**, (2017).

203. Nocera, G. & Jacob, C. Mechanisms of Schwann cell plasticity involved in peripheral nerve repair after injury. *Cell. Mol. Life Sci. CMLS* **77**, 3977–3989 (2020).

204. Jaegle, M. *et al.* The POU proteins Brn-2 and Oct-6 share important functions in Schwann cell development. *Genes Dev.* **17**, 1380–1391 (2003).

205. Newbern, J. M. *et al.* Specific Functions for ERK/MAPK Signaling during PNS Development. *Neuron* **69**, 91–105 (2011).

206. Raphael, A. R., Lyons, D. A. & Talbot, W. S. ErbB signaling has a role in radial sorting independent of Schwann cell number. *Glia* **59**, 1047–1055 (2011).

207. Feltri, M. L., Poitelon, Y. & Previtali, S. C. How Schwann Cells Sort Axons: New Concepts. *The Neuroscientist* **22**, 252–265 (2016).

208. Gomez-Sanchez, J. A. *et al.* After Nerve Injury, Lineage Tracing Shows That Myelin and Remak Schwann Cells Elongate Extensively and Branch to Form Repair Schwann Cells, Which Shorten Radically on Remyelination. *J. Neurosci.* **37**, 9086–9099 (2017).

209. Newbern, J. & Birchmeier, C. Nrg1/ErbB signaling networks in Schwann cell development and myelination. *Semin. Cell Dev. Biol.* **21**, 922–928 (2010).

210. Finzsch, M. *et al.* Sox10 is required for Schwann cell identity and progression beyond the immature Schwann cell stage. *J. Cell Biol.* **189**, 701–712 (2010).

211. Lawson, N. D. & Wolfe, S. A. Forward and Reverse Genetic Approaches for the Analysis of Vertebrate Development in the Zebrafish. *Dev. Cell* **21**, 48–64 (2011).

212. Sanchez, N. E. *et al*. Whole Genome Sequencing-Based Mapping and Candidate Identification of Mutations from Fixed Zebrafish Tissue. *G3 GenesGenomesGenetics* **7**, 3415–3425 (2017).

213. Wienholds, E. *et al*. Efficient Target-Selected Mutagenesis in Zebrafish. *Genome Res*. **13**, 2700–2707 (2003).

214. Swanhart, L. M. *et al*. Characterization of an lhx1a transgenic reporter in zebrafish. *Int. J. Dev. Biol*. **54**, 731–736 (2010).

215. Mensch, S. *et al*. Synaptic vesicle release regulates myelin sheath number of individual oligodendrocytes in vivo. *Nat. Neurosci*. **18**, 628–630 (2015).

216. Yeh, C.-H., Bellon, M. & Nicot, C. FBXW7: a critical tumor suppressor of human cancers. *Mol. Cancer* **17**, 115 (2018).

217. Berke, S. J. S. & Paulson, H. L. Protein aggregation and the ubiquitin proteasome pathway: gaining the UPPer hand on neurodegeneration. *Curr. Opin. Genet. Dev*. **13**, 253–261 (2003).

218. Cova, D. L. & C, C. The Highs and Lows of FBXW7: New Insights into Substrate Affinity in Disease and Development. *Cells* **12**, 2141 (2023).

219. Akhoondi, S. *et al*. FBXW7/hCDC4 Is a General Tumor Suppressor in Human Cancer. *Cancer Res*. **67**, 9006–9012 (2007).

220. Nguyen, K. M. & Busino, L. The Biology of F-box Proteins: The SCF Family of E3 Ubiquitin Ligases. in *Cullin-RING Ligases and Protein Neddylation: Biology and Therapeutics* (eds. Sun, Y., Wei, W. & Jin, J.) 111–122 (Springer, Singapore, 2020). doi:10.1007/978-981-15-1025-0_8.

221. Snyder, J. L., Kearns, C. A. & Appel, B. Fbxw7 regulates Notch to control specification of neural precursors for oligodendrocyte fate. *Neural Develop.* **7**, 15 (2012).

222. Kulkarni, A., Emerson, J., Danziger, N., Elvin, J. A. & DiSilvestro, P. A. Response of mTOR inhibitor associated with mutation of FBXW7 gene identified by comprehensive genomic profiling in cervical squamous cell carcinoma supports additional therapy opportunity for select patients with treatment-refractory, recurrent disease. *Gynecol. Oncol.* **159**, 166–167 (2020).

223. Matsumoto, A. *et al.* Fbxw7-dependent Degradation of Notch Is Required for Control of "Stemness" and Neuronal-Glial Differentiation in Neural Stem Cells *. *J. Biol. Chem.* **286**, 13754–13764 (2011).

224. Zhang, Z. *et al.* Function and regulation of F-box/WD repeat-containing protein 7 (Review). *Oncol. Lett.* **20**, 1526–1534 (2020).

225. Harty, B. L. *et al.* Myelinating Schwann cells ensheath multiple axons in the absence of E3 ligase component Fbxw7. *Nat. Commun.* **10**, 2976 (2019).

226. Harrington, E. P. *et al.* Oligodendrocyte PTEN required for myelin and axonal integrity not remyelination. *Ann. Neurol.* **68**, 703–716 (2010).

227. Flores, A. I. *et al.* Constitutively Active Akt Induces Enhanced Myelination in the CNS. *J. Neurosci.* **28**, 7174–7183 (2008).

228. Kearns, C. A., Ravanelli, A. M., Cooper, K. & Appel, B. Fbxw7 Limits Myelination by Inhibiting mTOR Signaling. *J. Neurosci.* **35**, 14861–14871 (2015).

229. Nakayama, S., Yumimoto, K., Kawamura, A. & Nakayama, K. I. Degradation of the endoplasmic reticulum-anchored transcription factor MyRF by the ubiquitin ligase SCFFbxw7 in a manner dependent on the kinase GSK-3. *J. Biol. Chem.* **293**, 5705–5714 (2018).

230. Busino, L. *et al.* Fbxw7α- and GSK3-mediated degradation of p100 is a pro-survival mechanism in multiple myeloma. *Nat. Cell Biol.* **14**, 375–385 (2012).

231. Madden, M. E. *et al.* CNS Hypomyelination Disrupts Axonal Conduction and Behavior in Larval Zebrafish. *J. Neurosci. Off. J. Soc. Neurosci.* **41**, 9099–9111 (2021).

232. Gibson, E. M. *et al.* Neuronal Activity Promotes Oligodendrogenesis and Adaptive Myelination in the Mammalian Brain. *Science* **344**, 1252304 (2014).

233. Alizadeh, A., Dyck, S. M. & Karimi-Abdolrezaee, S. Myelin damage and repair in pathologic CNS: challenges and prospects. *Front. Mol. Neurosci.* **8**, (2015).

234. Labun, K. *et al.* CHOPCHOP v3: expanding the CRISPR web toolbox beyond genome editing. *Nucleic Acids Res.* **47**, W171–W174 (2019).

235. Almeida, R. G. & Lyons, D. A. Intersectional Gene Expression in Zebrafish Using the Split KalTA4 System. *Zebrafish* **12**, 377–386 (2015).

236. Schüller, U. *et al.* Acquisition of granule neuron precursor identity is a critical determinant of progenitor cell competence to form Shh-induced medulloblastoma. *Cancer Cell* **14**, 123–134 (2008).

237. Doerflinger, N. H., Macklin, W. B. & Popko, B. Inducible site-specific recombination in myelinating cells. *Genes. N. Y. N 2000* **35**, 63–72 (2003).

238. Mo, A. *et al.* Epigenomic Signatures of Neuronal Diversity in the Mammalian Brain. *Neuron* **86**, 1369–1384 (2015).

239. Dugas, J. C. & Emery, B. Purification of Oligodendrocyte Precursor Cells from Rat Cortices by Immunopanning. *Cold Spring Harb. Protoc.* **2013**, pdb.prot070862 (2013).

240. Wilmarth, P. A., Riviere, M. A. & David, L. L. Techniques for accurate protein identification in shotgun proteomic studies of human, mouse, bovine, and chicken lenses. *J. Ocul. Biol. Dis. Infor.* **2**, 223–234 (2009).

241. Eng, J. K., Jahan, T. A. & Hoopmann, M. R. Comet: an open-source MS/MS sequence database search tool. *Proteomics* **13**, 22–24 (2013).

242. Perez-Riverol, Y. *et al.* The PRIDE database at 20 years: 2025 update. *Nucleic Acids Res.* **53**, D543–D553 (2024).

243. Deutsch, E. W. *et al.* The ProteomeXchange consortium at 10 years: 2023 update. *Nucleic Acids Res.* **51**, D1539–D1548 (2023).

244. Perez-Riverol, Y. *et al.* PRIDE Inspector Toolsuite: Moving Toward a Universal Visualization Tool for Proteomics Data Standard Formats and Quality Assessment of ProteomeXchange Datasets. *Mol. Cell. Proteomics MCP* **15**, 305–317 (2016).

245. Kim, H. *et al.* Notch-regulated perineurium development from zebrafish spinal cord. *Neurosci. Lett.* **448**, 240–244 (2008).

246. Peri, F. & Nüsslein-Volhard, C. Live Imaging of Neuronal Degradation by Microglia Reveals a Role for v0-ATPase a1 in Phagosomal Fusion In Vivo. *Cell* **133**, 916–927 (2008).

247. Waxman, S. G. & Bennett, M. V. L. Relative Conduction Velocities of Small Myelinated and Non-myelinated Fibres in the Central Nervous System. *Nature. New Biol.* **238**, 217–219 (1972).

248. Raff, M. C., Miller, R. H. & Noble, M. A glial progenitor cell that develops in vitro into an astrocyte or an oligodendrocyte depending on culture medium. *Nature* **303**, 390–396 (1983).

249. Saher, G. & Simons, M. Cholesterol and Myelin Biogenesis. in *Cholesterol Binding and Cholesterol Transport Proteins: Structure and Function in Health and Disease* (ed. Harris, J. R.) 489–508 (Springer Netherlands, Dordrecht, 2010). doi:10.1007/978-90-481-8622-8_18.

250. Auer, F., Vagionitis, S. & Czopka, T. Evidence for Myelin Sheath Remodeling in the CNS Revealed by In Vivo Imaging. *Curr. Biol.* **28**, 549-559.e3 (2018).

251. Nateri, A. S., Riera-Sans, L., Costa, C. D. & Behrens, A. The Ubiquitin Ligase SCFFbw7 Antagonizes Apoptotic JNK Signaling. *Science* **303**, 1374–1378 (2004).

252. Ye, X. *et al.* Recognition of Phosphodegron Motifs in Human Cyclin E by the SCFFbw7 Ubiquitin Ligase*. *J. Biol. Chem.* **279**, 50110–50119 (2004).

253. Yada, M. *et al.* Phosphorylation-dependent degradation of c-Myc is mediated by the F-box protein Fbw7. *EMBO J.* **23**, 2116–2125 (2004).

254. Thompson, B. J. *et al.* Control of hematopoietic stem cell quiescence by the E3 ubiquitin ligase Fbw7. *J. Exp. Med.* **205**, 1395–1408 (2008).

255. Orthmann-Murphy, J. *et al.* Remyelination alters the pattern of myelin in the cerebral cortex. *eLife* **9**, e56621 (2020).

256. Klingseisen, A. *et al.* Oligodendrocyte Neurofascin Independently Regulates Both Myelin Targeting and Sheath Growth in the CNS. *Dev. Cell* **51**, 730-744.e6 (2019).

257. Barron, T., Saifetiarova, J., Bhat, M. A. & Kim, J. H. Myelination of Purkinje axons is critical for resilient synaptic transmission in the deep cerebellar nucleus. *Sci. Rep.* **8**, 1022 (2018).

258. Koike, M. *et al.* Purkinje Cells Are More Vulnerable to the Specific Depletion of Cathepsin D Than to That of Atg7. *Am. J. Pathol.* **187**, 1586–1600 (2017).

259. Winston, J. T., Koepp, D. M., Zhu, C., Elledge, S. J. & Harper, J. W. A family of mammalian F-box proteins. *Curr. Biol.* **9**, 1180-S3 (1999).

260. Zhang, J. *et al.* Rack1 protects N-terminal phosphorylated c-Jun from Fbw7-mediated degradation. *Oncogene* **31**, 1835–1844 (2012).

261. Richter, K. T., Kschonsak, Y. T., Vodicska, B. & Hoffmann, I. FBXO45-MYCBP2 regulates mitotic cell fate by targeting FBXW7 for degradation. *Cell Death Differ.* **27**, 758–772 (2020).

262. Hartley, M. D. *et al.* Myelin repair stimulated by CNS-selective thyroid hormone action. *JCI Insight* **4**, (2019).

263. Jin, J., Ang, X. L., Shirogane, T. & Wade Harper, J. Identification of Substrates for F-Box Proteins. in *Methods in Enzymology* vol. 399 287–309 (Academic Press, 2005).

264. Rosenbluth, J. REDUNDANT MYELIN SHEATHS AND OTHER ULTRASTRUCTURAL FEATURES OF THE TOAD CEREBELLUM. *J. Cell Biol.* **28**, 73–93 (1966).

265. Cooper, M. H. & Beal, J. A. Myelinated granule cell bodies in the cerebellum of the monkey (Saimiri sciureus). *Anat. Rec.* **187**, 249–255 (1977).

266. Katanov, C. *et al.* N-Wasp Regulates Oligodendrocyte Myelination. *J. Neurosci.* **40**, 6103–6111 (2020).

267. Elazar, N. *et al.* Axoglial Adhesion by Cadm4 Regulates CNS Myelination. *Neuron* **101**, 224-231.e5 (2019).

268. Kipreos, E. T. & Pagano, M. The F-box protein family. *Genome Biol.* **1**, reviews3002.1 (2000).

269. Zhang, Y., Peng, Z., Zhao, Y. & Chen, L. microRNA-25 Inhibits Cell Apoptosis of Human Gastric Adenocarcinoma Cell Line AGS via Regulating CCNE1 and MYC. *Med. Sci. Monit. Int. Med. J. Exp. Clin. Res.* **22**, 1415–1420 (2016).

270. Zhou, X., Jin, W., Jia, H., Yan, J. & Zhang, G. MiR-223 promotes the cisplatin resistance of human gastric cancer cells via regulating cell cycle by targeting FBXW7. *J. Exp. Clin. Cancer Res.* **34**, 28 (2015).

271. Elbaz, B. *et al.* Phosphorylation State of ZFP24 Controls Oligodendrocyte Differentiation. *Cell Rep.* **23**, 2254–2263 (2018).

272. Kornfeld, S. F., Cummings, S. E., Fathi, S., Bonin, S. R. & Kothary, R. MiRNA-145-5p prevents differentiation of oligodendrocyte progenitor cells by regulating expression of myelin gene regulatory factor. *J. Cell. Physiol.* **236**, 997–1012 (2021).

273. Djannatian, M. *et al.* Two adhesive systems cooperatively regulate axon ensheathment and myelin growth in the CNS. *Nat. Commun.* **10**, 4794 (2019).

274. Zawadzka, M. *et al.* CNS-Resident Glial Progenitor/Stem Cells Produce Schwann Cells as well as Oligodendrocytes during Repair of CNS Demyelination. *Cell Stem Cell* **6**, 578–590 (2010).

275. Chapman, T. W., Kamen, Y., Piedra, E. T. & Hill, R. A. Oligodendrocyte Maturation Alters the Cell Death Mechanisms That Cause Demyelination. *J. Neurosci.* **44**, (2024).

276. Bonetti, B. *et al.* Activation of NF-kappaB and c-jun transcription factors in multiple sclerosis lesions. Implications for oligodendrocyte pathology. *Am. J. Pathol.* **155**, 1433–1438 (1999).

277. Srinivasan, R. *et al.* New Transgenic Mouse Lines for Selectively Targeting Astrocytes and Studying Calcium Signals in Astrocyte Processes In Situ and In Vivo. *Neuron* **92**, 1181–1195 (2016).

278. Park, Y. M., Chun, H., Shin, J.-I. & Lee, C. J. Astrocyte Specificity and Coverage of hGFAP-CreERT2 [Tg(GFAP-Cre/ERT2)13Kdmc] Mouse Line in Various Brain Regions. *Exp. Neurobiol.* **27**, 508–525 (2018).

279. Gonzalez, G. A. *et al*. Tamoxifen accelerates the repair of demyelinated lesions in the central nervous system. *Sci. Rep.* **6**, 31599 (2016).

280. Jessen, K. R. & Mirsky, R. The Role of c-Jun and Autocrine Signaling Loops in the Control of Repair Schwann Cells and Regeneration. *Front. Cell. Neurosci.* **15**, (2022).

281. Fischer, I., Konola, J. & Cochary, E. Microtubule associated protein (MAP1B) is present in cultured oligodendrocytes and co-localizes with tubulin. *J. Neurosci. Res.* **27**, 112–124 (1990).

282. Zhao, L. *et al*. QKI Binds MAP1B mRNA and Enhances MAP1B Expression during Oligodendrocyte Development. *Mol. Biol. Cell* **17**, 4179–4186 (2006).

283. Zhang, Y. *et al*. F-box protein RAE1 regulates the stability of the aluminum-resistance transcription factor STOP1 in Arabidopsis. *Proc. Natl. Acad. Sci.* **116**, 319–327 (2019).

284. Quarles, R. H. Myelin-associated glycoprotein (MAG): past, present and beyond. *J. Neurochem.* **100**, 1431–1448 (2007).

285. Çolakoğlu, G., Bergstrom-Tyrberg, U., Berglund, E. O. & Ranscht, B. Contactin-1 regulates myelination and nodal/paranodal domain organization in the central nervous system. *Proc. Natl. Acad. Sci. U. S. A.* **111**, E394–E403 (2014).